Kinematics and Thermodynamics of a Two-Dimensional Fermi Gas

A thesis submitted for the degree of

Doctor of Philosophy

by

Kristian Fenech

Centre for Quantum and Optical Science

Faculty of Science, Engineering and Technology

Swinburne University of technology

Melbourne, Australia

June 27, 2016

Abstract

Degenerate Fermi gases provide a versatile platform to study interacting quantum systems. When confined to highly oblate trap geometries, these gases can be used to probe two-dimensional physics by freezing out the dynamics of the gas in one dimension. This thesis presents two studies of a two-dimensional Fermi gas, confined to a blue-detuned TEM_{01} mode optical trap with a trapping frequency in the transverse (tight) direction $\frac{\omega_z}{2\pi} = 5.15\,\text{kHz}$ and $\frac{\omega_r}{2\pi} = 25\,\text{Hz}$ in the radial direction.

The first experiment is an investigation of how interactions between particles drive a strongly confined Fermi gas out of the strict two-dimensional regime [Dyk16a]. By tuning the *s*-wave scattering length through the Feshbach resonance at 832.2 G and imaging the released gas after an expansion time of $\tau = 600\,\mu\text{s}$ the transverse width can be measured. From this measurement an enhancement in the transverse release energy is observed close to the Feshbach resonance, beginning at 850 G and peaking at 810 G. Such an enhancement in the transverse width indicates the presence of transverse excitations.

By measuring the transverse width as a function of atom number N the 3D to 2D transition can be observed when the transverse width becomes independent of N, indicating that only the transverse ground state remains occupied. This measurement was conducted from the very weakly attractive BCS side of the Feshbach resonance at 972 G to just below the Feshbach resonance at 820 G. As the *s*-wave scattering length a_{3D} approaches the transverse harmonic oscillator length l_z a lower atom number is required to observe kinematically two-dimensional behaviour. This trend continues towards the BEC side of the Feshbach resonance, where eventually no strictly two-dimensional behaviour was found for the accessible range of atom numbers.

The second experiment in this thesis is the determination of the thermodynamic

properties of a two-dimensional Fermi gas with attractive interactions [Fen16b]. For a two-dimensional Fermi gas the true density distribution is readily accessible by absorption imaging. From the density distribution it is possible to extract the thermodynamic properties of the gas such as the pressure P and isothermal compressibility κ [Ho04]. Using these properties the density and pressure equations of state are determined. The density equation of state when normalised by the ideal gas result is non-monotonic with respect to $\beta\mu$ where $\beta = 1/k_B T$ and μ is the chemical potential. This result is significantly different to the case of a three-dimensional Fermi gas and arises due to the modified scattering properties in two dimensions and the existence of a two-body bound state for any arbitrary weak attractive interaction. A determination of additional thermodynamic properties—internal energy, chemical potential, entropy and Helmholtz free energy—was also performed, providing a detailed picture of the thermodynamic properties for a two-dimensional Fermi gas in the normal phase.

Declaration

I, Kristian Fenech, declare that this thesis entitled:

"Kinematics and thermodynamics of a two-dimensional Fermi gas"

contains no material which has been accepted for the award to the candidate of any other degree or diploma, except where due reference is made in the text of the examinable outcome; to the best of my knowledge, contains no material previously published or written by another person except where due reference is made in the text of the examinable outcome; and where work is based on joint research or publications, discloses the relative contributions of the respective workers or authors.

Kristian Fenech

Centre for Quantum and Optical Science (CQOS)
Faculty of Science, Engineering and Technology
Swinburne University of Technology
Melbourne, Australia

June 27, 2016

Acknowledgments

After going on the journey which was this PhD, I have learned much and have had the pleasure of being surrounded by many wonderful, intelligent and supportive people. All of whom I owe great thanks. My first thanks goes to my supervisors; Chris Vale and Peter Hannaford. Without their guidance this work would not have been possible.

Chris' explanations on some of the physics we saw in the lab would often lead to those precious mental moment when the penny drops and what was confusing becomes suddenly clear. I would also like to thank Chris for all of the feedback he has provided, not only during the writing of this thesis but also his suggestions to improve the experiment, the analysis and the communication of the work. Next I would like to thank Peter, his knowledge and experience in physics has been both very useful and very entertaining.

It's been fantastic working with everyone in the lab, some I have known longer than others but all have left an impression and I hope I have taken away from each of you a positive trait. To Marcus, Sascha, Paul and Tyson you have all been an essential part of my time in the group. To all of the other members of CQOS you have made these years a spectacular joy, from lunch and tea time discussion to general shenanigans you will all be remembered.

Outside of the labs, I would like to thank my family for their support not only during my PhD but for all the times they have been there and to the Simonyi family for their hospitality, support and curioisty about what I was spending my time on.

Finally I would like to thank my partner Kinga Simonyi, she has gone above and beyond in her level of support during my PhD, particular in the closing stages where she shouldered as much of the life related burdens as she could to allow me to put words to paper. I could not have asked for a better supporter than her.

Contents

List of Figures

List of Tables

Chapter 1

Introduction

1.1 Motivation and background

Quantum gases have presented themselves as a valuable tool for developing our understanding of the quantum mechanical behaviour of matter [Fey82; Gre02; Blo05; Bul09; Van12]. This capability was born through a number of paradigm changing developments. Trapping and cooling of atoms was essential to making quantum gases viable, with a range of cooling techniques developed which take advantage of the interactions between light and matter which far exceeded the cooling ability provided by traditional cryogenic methods.

Bose-Einstein condensation predicted in 1925, was first observed in liquid ^{4}He [Kap38; Lon38]. With the breakthroughs in optical cooling and trapping it became readily obtainable in the alkali elements [And95; Dav95; Bra95]. Not long after the observation of alkali BECs, came the realisation of degenerate Fermi gases [DeM99; Tru01]. The monumental efforts of the researchers involved helped clearly expose the quantum nature of both bosonic and fermionic particles.

These newly accessible quantum degenerate systems provide an exciting test bed for understanding more complicated physics. Unlike condensed matter systems, where the number of parameters which are available for manipulation is often restricted by the nature of the material, dilute quantum gases do not suffer from these limitations. The level of complexity relative to that found in traditional condensed matter research is also significantly lower, as many quantum degenerate gases consist of only a single

atomic species where the interactions are dominated by the van der Waals interaction between atoms. Due to the depth of research in atomic physics, the microscopic details of particles and their interactions with external fields are precisely known and we can take advantage of these properties in many ways. An example of such an advantage is found in the fact that interactions between particles can be readily controlled through the scattering resonance known as the Feshbach resonance [Fes58].

A Feshbach resonance allows the direct control of the *s*-wave scattering length which fully characterises the interparticle interaction at low energies. It would not be amiss to think that the control of such a fundamental property of interacting particles would be fraught with difficulty. As it turns out, control of the interactions through the Feshbach resonance in a quantum gas can be achieved simply through the application of a magnetic field, where the required magnetic field strengths are readily achievable with commercial power supplies. For the case of fermions, the Feshbach resonance allows more than just the direct control of the interactions. It permits the creation of a tunable superfluid in which the bosonic and fermionic limits are smoothly connected.

On one side of the Feshbach resonance in a system containing fermions in two quantum states, a weak attractive interaction between atoms of opposite spin in the presence of the Fermi sea leads to the formation of weakly bound Cooper pairs [Coo56]. These Cooper pairs act as a composite boson and can undergo condensation below the critical temperature T_c and superfluidity described by BCS theory can emerge [Bar57]. On the opposite side of the resonance it becomes energetically favourable for two particles to form a tightly bound molecule. Similar to the case of the Cooper pairs, these molecules are a composite boson and can undergo condensation; such a condensate is known as a molecular BEC [Str03; Cub03; Joc03b; Zwi03; Reg03; Gre03; Joc03a]. Here the fermionic nature of the constituent particles is not significant and condensation is similar to that of regular bosonic atoms. Each of these two limits can be described by different physics, but the transition between them is smoothly connected by the unitary regime accessed at the pole of the Feshbach resonance [Sá 93].

In many materials there exists the property of superconductivity, which is a result of superfluidity involving charged particles. This phenomenon was discovered by Heike Kamerlingh Onnes in 1911 during his work on refrigerants. By cooling liquid helium

to temperatures as low as 1.5 K and using this to cool conductive materials, Onnes was able to uncover superconductivity in mercury [Kam11a; Kam11b; Kam11c].

Ever since the discovery of superconductivity there has been continued interest in creating materials which are superconductive at ever higher temperatures, with the goal of room temperature superconductors in the minds of many. A particular type of superconductor, known as the cuprates, first discovered by Bednorz and Müller in 1986 [Bed86] has been verified to have transition temperatures as high as 133 K [Sch93]. While the exact nature of such high-T_c superconductivity is not yet fully understood, the materials contain within them quasi-two-dimensional copper-oxide planes and it may be possible to further our understanding of such materials through the study of highly controllable quasi-two-dimensional Fermi gases.

Dimensionality is critical when examining physical phenomena and reduced dimensions can lead to qualitatively different physics. For a two-dimensional system it was argued by Peierls [Pei35] that thermal fluctuation destroys long-range order in two dimensions. This destruction of long-range order was proven by Mermin and Wagner in 1966 [Mer66] and independently by Hohenberg [Hoh67]. Building on this was the work of Berezinskii, Kosterlitz and Thouless (BKT). They defined a new type of order for two-dimensional systems known as topological order [Ber71; Kos72]. They describe a phase transition in which, for a two-dimensional superfluid, the condensate wavefunction, can be defined in certain regions of the superfluid leading to long range order through the spontaneous proliferation of vortex-antivortex pairs. It is this BKT transition in two dimensions which accompanies the onset of superfluidity rather than the existence of a BEC which is commonly found with superfluidity in three dimensions.

The BKT transition in two dimensions has garnered significant theoretical attention in the context of Fermi gases. The vortex-antivortex pairing associated with the BKT transition in a two-dimensional Fermi gas was studied within a strong coupling regime [Bot06]. This analysis provided a first estimate of the critical temperature for the BKT transition of $T_{BKT} = 0.125E_F$, where E_F is the Fermi energy. Following this Zhang *et al.* also considered the Berezinksii-Kosterlitz-Thouless transition in a trapped quasi-two-dimensional Fermi gas near a Feshbach resonance [Zha08]. The transition

temperature in two dimensions behaves similarly to the three-dimensional case, increasing monotonically from the BCS side to a limiting value of $T_{BKT} = 0.075E_F$ on the BEC side of the resonance.

These results related only to a homogeneous gas. For a trapped gas it was noted that, while the Mermin-Wagner-Hohenberg theorem does not allow Bose-Einstein condensation at finite temperature [Mer66; Hoh67], this is only in the case of a uniform two-dimensional system. Quantum gases under examination in laboratory settings are typically not uniform, but are rather harmonically trapped where finite size effects may permit condensation [Bag91; Bay98]. It was also found that population imbalance contributes to the destruction of superfluidity in two dimensions [Tem09].

In three dimensions the nature of the smooth BCS-BEC crossover was of significant interest to theorists and experimentalists alike. The physics of the crossover in two dimensions is no exception. Early theoretical studies of this crossover using variational methods for a dilute two-dimensional Fermi gas at zero temperature were reported by Randeria *et al.* [Ran90]. In this case exact solutions for the *s*-wave pairing for the evolution of Cooper pairs to Bose-Einstein condensate were derived which showed that in two dimensions there too exists a smooth crossover from the BCS to BEC regime.

The BCS-BEC crossover in two dimensions was also examined using fixed-node diffusion Monte Carlo (FN-DMC) calculations [Ber11]. Using FN-DMC the equation of state and gap parameter as functions of interaction strength and an estimate of Tan's contact parameter across the BCS-BEC crossover were calculated. The contact parameter in three dimensions has been well studied using spectroscopic methods [Tör14] with Bragg spectroscopy [Vee08; Kuh11; Hoi13] and also radio-frequency spectroscopy [Sag12]. In two dimensions this property of the gas has been probed using radio-frequency spectroscopy to determine the bulk trap averaged contact for a range of interaction strengths [Frö12].

Building on the work of Bertaina *et al.*, Fischer and Parish developed a mean-field theory to describe the BCS-BEC crossover of a two-dimensional Fermi gas at zero temperature [Fis13]. They include in their model a large number of transverse harmonic oscillator states such that this theory describes a quasi-2D system. In their paper they provide three key results. The first is that in the extreme BEC regime if the confinement

length is greater than the dimer size then one obtains 3D dimers confined in quasi-2D with weak repulsive interactions, in line with the result of Petrov *et al.* [Pet01]. Their second result is that in a system with weak interactions and a Fermi energy less than the tight confinement, excited transverse levels strongly affect pairing in the system. Lastly they use their model to produce a theoretical radio-frequency spectrum and compare it to existing experimental results.

The accuracy of their model is evident in their good match to the experimental radio-frequency data and the model generalises to the true two-dimensional Fermi gas in the limit that $\omega_z \to \infty$, where ω_z is the trap frequency in the tightly confined direction. These results pose fundamental questions regarding the quantification of two-dimensionality in a trapped Fermi gas. In particular, when combined with the result that for even moderate interactions transverse excitations are expected to be present in a trapped Fermi gas [Kes06]. This leads to the first of two key questions to be examined in this thesis; how do interactions affect the dimensionality of a Fermi gas in a highly anisotropic confining potential?

There has also been significant interest in the determination of the superfluid transition temperature for a two-dimensional system [Tra94; Pet03]. However, calculations tend to break down in the strongly interacting regime and are often only valid in the limits of the weakly interacting BCS/BEC gas. In addition to the critical temperature other thermodynamic properties of a two-dimensional Fermi gas have been explored. In the high temperature limit the virial expansion has previously been used to determine the thermodynamics of the three-dimensional Fermi gas [Tho05]. The virial expansion has also been used to study a two-dimensional Fermi gas. For a harmonically trapped system the second and third order virial coefficients were determined and the high temperature thermodynamic properties calculated [Liu10]. These results, only probe the normal phase of the gas and are not valid at low temperatures where critical behaviour may be present. The virial expansion was also developed for homogeneous systems through diagrammatic methods and the high temperature pairing explored through the calculation of Tan's Contact parameter [Nga13].

The thermodynamics of a homogeneous two-dimensional Fermi gas have also been extended into the low-temperature regime with a strong-coupling theory known as the

Luttinger-Ward approximation [Bau14]. The Luttinger-Ward approximation is an implementation of the fully self-consistent Green's function (GG) model which solves the problem of scattering of fermions [Hau99]. Within this study a number of thermodynamic properties of a two-dimensional Fermi gas were determined. The authors show that the density equation of state, given by the density of the interacting gas normalised by the ideal density, is non-monotonic with respect to $\beta\mu$, where $\beta = 1/k_B T$ and μ is the chemical potential. This behaviour deviates significantly from the three-dimensional case. This non-monotonic behaviour is also found in lattice quantum Monte-Carlo (LQMC) simulations, but for the same interaction strength the LQMC result is slightly lower than the Luttinger-Ward result [And15]. Such a discrepancy necessitates experimental determination to further inform the development of more accurate models. The determination of these thermodynamic properties constitutes the second focus of this thesis.

Transitioning to the experimental side there have been a number of realisations of two-dimensional Fermi gases, utilising a number of different trapping geometries including optical lattices [Mar10; Rie15a], red-detuned dipole traps [Dyk11] and blue-detuned TEM_{01} mode traps [Mey05].

The first observation of a quasi-two-dimensional Fermi gas was reported by Modugno *et al.* [Mod03]. In their experiment they prepare ^{40}K atoms sympathetically cooled with ^{87}Rb, where the cooled ^{40}K is trapped in a one-dimensional optical lattice. Observed changes in the density indicated the onset of the quasi-two-dimensional nature of the gas. The authors also attempted to explore the dynamics of the gas by perturbing the atoms with a sudden displacement in the axial direction, where it was found the dynamics of the gas were heavily damped.

Another trapping geometry was presented by Meyrath *et al.* in 2005. They describe a method to create a high frequency optical trap using Hermite-Gaussian beams as well as a characterisation of this trap [Mey05]. In order to achieve this they created a π phase plate to transform a regular Gaussian mode into a TEM_{01} mode. The tight trapping frequencies achieved in their experiment reach values of up to 66 kHz which is due to the 2.4 µm transverse width of their focused beam.

In 2010 Martiyanov *et al.* reported the observation of a two-dimensional Fermi

gas [Mar10]. In order to create their trap they use a red-detuned optical lattice with lattice spacing of 5.3 μm with radial trapping frequency of 102(4) Hz and a tight trapping frequency of 5.57(11) kHz. They show that on the time scale of the experiment there should be no tunnelling between lattice sites and to maintain that the gas would only occupy the axial ground state they ensured that the Fermi energy remained below $\hbar\omega_z$. This was determined by temperature measurements which were made by fitting their acquired density profiles to the finite-temperature Thomas Fermi distribution. Using this method they determine the temperature of their trap to be 18 nK. This method of temperature measurement is limited to the case of a weakly interacting gas on the BCS side of the Feshbach resonance.

With a number of groups successful in creating two-dimensional Fermi gases there has been a number of experiments conducted looking at pairing, thermodynamics and superfluidity. The 3D to 2D crossover was observed by Dyke *et al.* [Dyk10]. The transition between three and two dimensions is marked by changes in the spatial characteristics of the gas, and can be determined by observing a change in the dependence of the Fermi radius on total atom number N from $N^{1/6}$ in three dimensions to $N^{1/4}$ in two dimensions. In addition to this measurement, the transverse width of the gas showed shell structure as the total atom number was increased. This occurred due to the filling of discrete excited transverse states. Both of these measurements provide a direct method to determine the dimensionality of a trapped Fermi gas.

The effects of dimensionality on pairing were experimentally examined using radio-frequency spectroscopy across the Feshbach resonance [Fel11; Som12]. By tuning the lattice depth the pairing behaviour across the 3D to 2D transitions was directly accessible. The reduction in dimensionality resulted in an increased separation between the single particle and pairing peaks in the observed RF spectrum.

Experiments conducted on Bose gases are also of interest as it is possible to create such a BEC via the Feshbach resonance. With significant theoretical work involved in the development of the theory behind the Berezinskii-Kosterlitz-Thouless transition, evidence of the BKT transition in a two-dimensional Bose gas was observed by Hadzibabic *et al.* [Had06]. The evidence for the transition was clear through the observation of phase dislocations in the interference pattern of two BECs.

Directly related to our experiments both in terms of goal and technical challenges was the measurement of the pressure and phase-space density of bosonic ^{87}Rb and their dependencies on total atom number, density, chemical potential and temperature [Yef11]. Experimental similarities exist in the trap geometry and imaging technique as both ours and their traps are blue-detuned TEM_{01} mode traps and imaging is performed via absorption imaging.

Following their initial observation of a two-dimensional Fermi gas, Makhalov *et al.* conducted experiments to obtain the ground-state pressure of a quasi-two-dimensional Fermi gas across the BCS-BEC crossover [Mak14]. This experiment marked the first significant steps towards the measurement of the thermodynamics of a two-dimensional Fermi gas. Due to their lattice geometry they did not have experimental access to the true density distribution of their gas, which is accessible to our experiment.

Most recently the first measurements of the phase diagram of a two-dimensional Fermi gas were obtained [Rie15a], by using a method of matter wave Fourier optics together with a time of flight measurement to extract the momentum distribution [Mur14]. Below a critical temperature they observed signatures of pair condensation and found critical temperatures across the BKT-BCS crossover. Observed temperatures on the BCS side of the resonance were observed to be slightly above the current theoretical prediction. Further measurement of the first-order correlation function showed a transition to algebraic decay below the critical temperature, consistent with BKT superfluidity [Mur15].

Following the trajectory of previous theoretical and experimental work, it is clear that there are significant open questions regarding the notion of dimensionality and the subsequent thermodynamics of a two-dimensional Fermi gas. The work described in this thesis addresses these questions.

1.2 Thesis outline

Chapter 2 This chapter provides the basic theoretical framework necessary for understanding ultracold Fermi gases in 3D and 2D. In this chapter we begin with examining the ideal Fermi gas in both 3D and 2D. With this foundation we will introduce interactions and examine the difference in scattering and pairing between 3D and 2D systems and finally the phenomenon of the Feshbach resonance and BCS–Bose crossover will be discussed.

Chapter 3 As this thesis is the first account of a TEM_{01} mode optical dipole trap being used to confine a degenerate Fermi gas in two dimensions within the ultracold Fermi gas group at Swinburne this chapter will provide a description of how such a gas is produced and observed experimentally. This chapter will begin with a brief overview of the existing experimental apparatus and the techniques used in order to produce a degenerate Fermi gas in three dimensions. Following this a description of how the TEM_{01} mode optical trap is formed will be given. Finally, the characterisation of our optical trap and review the procedure to cross from the 3D trap to the 2D trap will be presented.

Chapter 4 This chapter will detail the first key experimental result of this thesis. Before being able to conduct any experiments on a two-dimensional system it is necessary to ascertain the conditions in which one can claim to have a kinematically two-dimensional Fermi gas in the presence of interactions. To examine this, two sets of experiments are conducted in order to observe the influence of interactions and finally present the parameter range for which we can be assured that our gas is kinematically two-dimensional for future experiments.

Chapter 5 This chapter details the second main experimental result. In this chapter thermodynamic properties for both the ideal gas and the interacting gas through the three-body virial expansion will be presented. Details regarding the methodology to extract the thermodynamics from the measured density distribution will be outlined. Finally the normalised density and pressure equations of state for an attractive Fermi

gas in two dimensions will be given in addition to the measurement of the chemical potential, free energy, internal energy and entropy.

Chapter 6 This chapter will summarise the previous chapters focusing on the key findings from chapters 4 and 5 as well as provide a discussion of future experiments which can be conducted with a two-dimensional Fermi gas.

Chapter 2

Degenerate Fermi gases in 3D and 2D

2.1 Introduction

Since the first realisation of a degenerate Fermi gas of ^{40}K in 1999 [DeM99], significant strides have been made in producing colder atomic samples and expanding the number of elements which can be cooled to degeneracy, including but not limited to ^{6}Li [Tru01], ^{161}Dy [Lu12], ^{167}Er [Aik14]. The experimental advantage which these systems wield when compared to more complex condensed matter systems is found both in their relative simplicity and in the ability to precisely tune the strength of interactions present in the system, allowing one to realise both an ideal non-interacting system or a strongly interacting quantum system. This control is enabled by a Feshbach resonance [Fes58] which allows the *s*-wave scattering length to be tuned via the application of external magnetic fields. A more significant implication of the Feshbach resonance is not simply in the ability to manipulate the magnitude of interactions but to provide access to the Bose-Einstein condensate (BEC)–Bardeen-Cooper-Schrieffer (BCS) crossover in three dimensions or the two-dimensional equivalent, the Berezinskii-Kosterlitz-Thouless (BKT)–BCS crossover. The information contained within this chapter will provide an introduction to the basic theoretical aspects of degenerate Fermi gases. Beginning with non interacting atoms, the ideal Fermi gas will be introduced, followed by a discussion of two-body scattering and then the many body picture with an emphasis on the role of interactions in two dimensions.

2.2 Ideal Fermi gases in 3D and 2D

The application of statistical formalisms to a gas of classical particles allowed the elucidation of the physics of a many-particle system without the need to know the microscopic details [Lan70]. Experiments involving degenerate Fermi gases deviate from classical Maxwell-Boltzmann statistics which govern particles at high temperatures; at low temperatures these systems operate under quantum statistics.

Here, we consider an ensemble of non-interacting spin-1/2 particles, in this case a collection of fermions in a single spin state. At low temperature, the behaviour of these particles is governed by Fermi-Dirac statistics which follows the distribution

$$n_{FD}(\varepsilon) = \frac{1}{\exp(\beta(\varepsilon - \mu)) + 1} \tag{2.1}$$

where $\beta = 1/k_B T$, k_B is the Boltzmann constant, T is the temperature, ε is the energy and μ is the chemical potential. Physically equation (2.1) describes the probability of a quantum state with energy ε being occupied. The chemical potential can be determined by the normalisation constraint $\sum n(\varepsilon_i) = N$, where N is the total number of particles in the system. In addition to the chemical potential the Fermi-Dirac distribution is also essential for describing other thermodynamic properties of a Fermi gas.

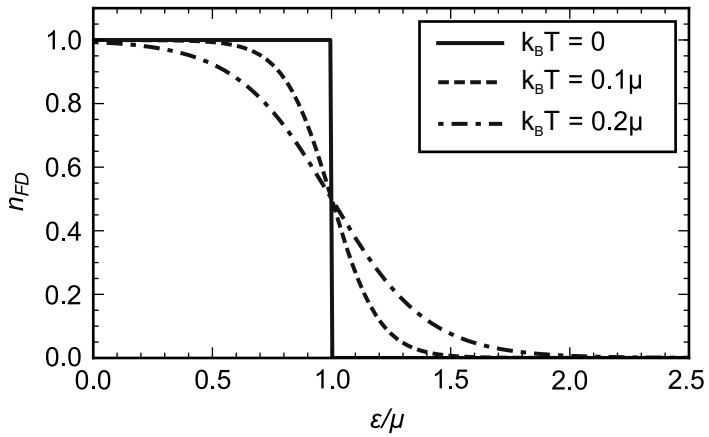

Figure 2.1: Fermi-Dirac distribution for particles at three temperatures. The solid line clearly demonstrates the Pauli exclusion principle in a system of fermions at $T = 0\,\mathrm{K}$, where all available quantum states are occupied up to the Fermi energy. At higher temperatures we see that particles can now be found in the higher energy states with increasing probability as the temperature increases.

Its connection to the thermodynamic properties is evident in the fact that n_{FD} is directly obtainable from the thermodynamic partition function Z in the grand canonical ensemble [Pat11] which fully describes the thermodynamic processes.

In the high temperature limit, when the energy $\varepsilon \gg \mu$ equation (2.1) reduces to the classical Boltzmann distribution and the system can be viewed as a classical gas. For our experiments the gases under observation are 'degenerate', which means the thermal de Broglie wavelength of the particles $\lambda = \sqrt{2\pi\hbar^2/mk_BT}$ is on the order of the mean interparticle spacing $n^{-1/3}$. If the following equality holds $\lambda^3 n^{-1/3} \approx 1$ a gas of fermions can be called degenerate. Based on this requirement to produce a degenerate Fermi gas one needs either low temperatures or high densities. In the following sections the properties of degenerate Fermi gases for both the homogeneous and harmonically trapped gas will be introduced for both three and two dimensions.

2.2.1 Homogeneous gas

Beginning with the homogeneous case, we have a gas with a uniform density distribution. Such a system can be created by confinement in a box potential with sides of length L and total volume L^3. A number of important properties of a quantum gas can be determined by the density of states. For a homogeneous system in three-dimensional phase-space all allowed momentum states are contained within a sphere with volume $V = 4\pi p^3/3$, where $p = \sqrt{2m\varepsilon}$ is the momentum. The total number of states with energy up to ε is determined by

$$G(\varepsilon) = V\frac{\sqrt{2}(m\varepsilon)^{3/2}}{3\pi^2\hbar^3} \tag{2.2}$$

where V is the system volume and m is the mass of the particle. Due to Heisenberg's uncertainty principle the minimum phase space volume in dimension D is given by $(2\pi\hbar)^D$ [Pet02]. The density of states can be found by determining the number of states located between energy ε and $\varepsilon + \delta\varepsilon$. By taking the derivative of equation 2.2

the density of states is given by

$$g(\varepsilon) = \frac{V m^{3/2} \varepsilon^{\frac{1}{2}}}{\pi^2 \sqrt{2} \hbar^3}. \tag{2.3}$$

Two important characteristics of Fermi gases are the Fermi energy E_F and the Fermi momentum k_F. These properties are connected to the dispersion relation for the particle. For a free particle we have $\varepsilon = p^2/2m$ and E_F can be determined in the zero temperature limit where it represents the energy of the highest lying occupied quantum state such that all other particles occupy states with energy $\varepsilon < E_F$ and is calculated as

$$N = \int g(\varepsilon) n_{FD}(\varepsilon) \mathrm{d}\varepsilon \tag{2.4}$$

where N is the total atom number. As n_{FD} is unity below the Fermi energy and zero elsewhere at zero temperature, equation (2.4) can be rewritten as

$$N = \int_0^{E_F} g(\varepsilon) \mathrm{d}\varepsilon \tag{2.5}$$

substituting equation (2.3) into the above equation and integrating, the Fermi energy and momentum are

$$E_F(n) = \frac{\hbar^2}{2m} \left(3\pi^2 n\right)^{2/3} \tag{2.6}$$

$$k_F(n) = \left(3\pi^2 n\right)^{1/3} \tag{2.7}$$

where $n = \frac{N}{V}$ is the density of the gas and the corresponding Fermi momentum was found by substituting $E_F = \frac{\hbar^2 k_F^2}{2m}$ into equation (2.6).

As the experimental sections of this thesis describe results for a two-dimensional gas, the results for the homogeneous gas in two dimensions will now be given in a similar fashion. As in the three-dimensional case we begin by determining the density of states for a homogeneous system in two dimensions. In our two-dimensional phase-space all available states are contained within a circle with area $A = \pi p^2$. As previously for a free particle we have $\varepsilon = p^2/2m$ or $p = \sqrt{(2m\varepsilon)}$. Therefore in two dimensions

the total number of available states is

$$G(\varepsilon) = \frac{A(m\varepsilon)}{2\pi\hbar^2} \tag{2.8}$$

differentiating equation (2.8) we can find that in two dimensions the density of states is

$$g_{2D}(\varepsilon) = \frac{Am}{2\pi\hbar^2}. \tag{2.9}$$

This procedure can be repeated for the D-dimensional case and one can find that $g_D(\varepsilon) \propto \varepsilon^{(D/2-1)}$ [Pet02]. From this a distinguishing feature of the two-dimensional system is that the density of states is constant, having no dependence on the energy. This has implications for the scattering behaviour in two dimensions which is discussed in Section 2.3.3. The reduced dimensionality results in a modification to the Fermi energy and Fermi momentum which are found in the same manner as for the three-dimensional gas and are given by

$$E_F = \frac{2\pi\hbar^2 N}{Am} = \frac{2\pi\hbar^2}{m} n \tag{2.10}$$

$$k_F = \sqrt{4\pi n} \tag{2.11}$$

where $n = \frac{N}{A}$ is the density and m is the mass of the particle.

2.2.2 Harmonically trapped gas

While it is possible to experimentally produce a homogeneous system by confinement in a box potential [Gau13], it is more common that confinement is provided by a harmonic potential, which for a D-dimensional potential can be written as

$$V(r) = \sum_i^D \frac{1}{2} m\omega_i^2 r_i^2 \tag{2.12}$$

where m is the atomic mass, ω_i is the trapping frequency of the i^{th} dimension and r_i is the displacement in the i^{th} dimension. By examining the zero temperature result for a collection of non-interacting fermions confined to a harmonic trap, shown in figure 2.2 as we did for the homogeneous gas, we can again extract a number of properties of

the system. When placed under the influence of a confining potential, the density of

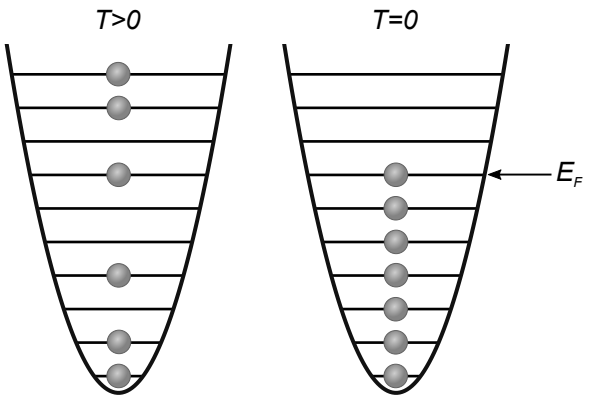

Figure 2.2: Harmonically trapped Fermi gas at non-zero temperature on the left, displaying the occupation of higher excited states, as the temperature is reduced at zero temperature the characteristic stacking of occupied energy levels due to Pauli exclusions becomes apparent.

states of the system shifts. In the limit of large N and where the energy level spacing is less than $k_B T$, a semi-classical approach can be used and the density of states for a D-dimensional system can be written as [Ket07]

$$g(\varepsilon) = \int \frac{\mathrm{d}^D\mathbf{r}\mathrm{d}^D\mathbf{p}}{(2\pi\hbar)^D}\delta(\varepsilon - \varepsilon(\mathbf{r},\mathbf{p})) \tag{2.13}$$

where δ is the Dirac delta function and $\varepsilon(\mathbf{r},\mathbf{p}) = \frac{p^2}{2m} - V(\mathbf{r},\mathbf{p})$ is the classical Hamiltonian. By solving the above integral it can be shown that for a D-dimensional system under harmonic confinement the density of states is given by [Ket07]

$$g(\varepsilon) = \frac{\varepsilon^{D-1}}{(D-1)!\Pi_i \hbar\omega_i} \tag{2.14}$$

which gives the following result for the case of a harmonically trapped gas in three dimensions

$$g^{H.O}(\varepsilon) = \frac{\varepsilon^2}{2\hbar^3\bar{\omega}^3} \tag{2.15}$$

where $\bar{\omega} = (\omega_x\omega_y\omega_z)^{1/3}$ is the geometric mean of the trap frequencies in each dimension. As in the homogeneous case, in the zero temperature limit by solving for

the density of states up to the highest occupied state one can determine the Fermi energy and momentum as

$$E_F = \hbar\bar{\omega}(6N)^{1/3} \tag{2.16}$$

$$k_F = \sqrt{\frac{2m\bar{\omega}}{\hbar}}(6N)^{1/6} \tag{2.17}$$

where N is the total atom number.

In configuration space from the density of states the spatial density distribution can be determined by integration over all momenta. The integral of the Fermi-Dirac distribution is given by the family of polylogarithm functions $Li_n(z)$. For a harmonically trapped gas in three dimensions the local density is given by [Sal00]

$$n(r) = \frac{1}{\lambda^3} Li_{3/2}\left(-e^{\beta(\mu - V(\mathbf{r}))}\right) \tag{2.18}$$

where λ is the thermal de Broglie wavelength, $\beta = 1/k_B T$, μ is the chemical potential and $V(\mathbf{r})$ is the trapping potential at position $\mathbf{r}$. At zero temperature, the maximum radius of the atomic cloud is the Fermi radius R_F. This distance is set by the relationship between the Fermi energy and the potential energy of the trap. The point at which $V(\mathbf{r}) = E_F$ defines the absolute edge of the density distribution and is equal to

$$R_{F,i} = \sqrt{\frac{2E_F}{m\omega_i^2}} = \sqrt{\frac{2\hbar\bar{\omega}}{m\omega_i^2}}(6N)^{1/6}. \tag{2.19}$$

By altering the confinement in the transverse direction, which we label z, to have a significantly larger frequency than the radial trap frequency ω_r, we can begin to explore what can be considered a two-dimensional system. While the atoms confined in the trap are still three-dimensional, it is possible to freeze out the motion in the transverse direction such that the only accessible degrees of freedom are those in the radial direction. For this condition to be satisfied we require $k_B T, E_F \ll \hbar\omega_z$. In the zero temperature limit these criteria can be intuitively understood by looking at the occupied energy levels in the radial and transverse trapping directions and is shown in figure 2.3. By including this non-isotropic confining potential the definitions of the

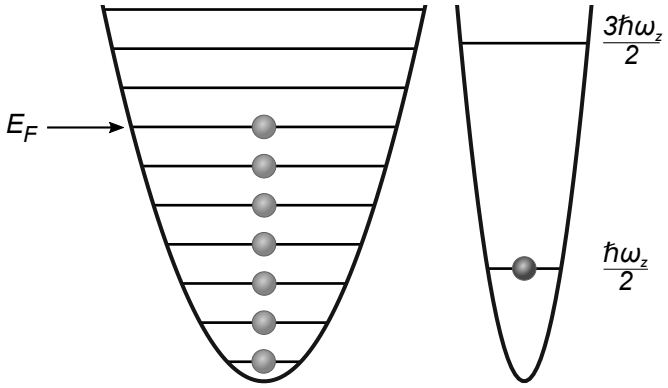

Figure 2.3: Zero temperature occupation of energy levels in an effective two-dimensional system of non-interacting fermions. Due to the high level of anisotropy in the trap there exists many available energy states in the radial (left) harmonic potential before the first excited state in the transverse (right) potential is energetically accessible. At zero temperature the total number of atoms is required to be small enough so as to not populate higher transverse excited states.

previously described properties for the harmonically trapped gas in three dimensions are altered.

Using the general form for the density of states for a D-dimensional gas given by equation (2.14) and using $D = 2$, the density of states is given as

$$g_{2D}^{H.O}(\varepsilon) = \frac{\varepsilon}{\hbar^2 \omega_x \omega_y}. \tag{2.20}$$

Consequently, as was done for three dimensions, the Fermi energy and wave vector can be found to be

$$E_{F,2D} = \sqrt{2N}\hbar\omega_r \tag{2.21}$$

$$k_{F,2D} = \sqrt{\frac{2m\omega_r}{\hbar}}(2N)^{1/4}. \tag{2.22}$$

As previously, we can also determine the spatial density profile for the gas and find

$$n_{2D}(r) = \frac{1}{\lambda^2} Li_1(e^{\beta(\mu - V(\mathbf{r}))}) \tag{2.23}$$

where $\beta = 1/k_B T$, μ is the chemical potential, λ is the thermal de Broglie wavelength

and $V(\mathbf{r})$ is the trapping potential. Calculation of the polylogarithm of order one is simplified as $Li_1(z) = -\ln(1-z)$. The Fermi radius can also be determined as in three dimensions and is given by

$$R_{i,F2D} = (8N)^{1/4}\sqrt{\frac{\hbar}{m\omega_r}}\frac{\omega_r}{\omega_i}. \tag{2.24}$$

As mentioned previously, in order to have a two-dimensional system we must satisfy the two-dimensional criteria $k_B T, E_F \ll \hbar\omega_z$. With this condition in mind it is possible to determine the maximum number of atoms which can be present while we remain in a two-dimensional state. This critical atom number is determined by counting the number of available states in the radial trapping direction which are below the first excited state of the transverse trapping potential. At zero temperature this ideal limit is given by [Dyk11]

$$N_{2D} = \sum_{n_r=0}^{\Lambda-1}(n_r+1) = \frac{\Lambda}{2}(\Lambda+1) \tag{2.25}$$

where $\Lambda = \frac{\omega_z}{\omega_r}$ is the aspect ratio of the oblate trap. Previous two-dimensional work conducted on this experiment was done with an aspect ratio $\Lambda \approx 60$ [Dyk11]. The work presented in this thesis is a significant improvement, with the new trap described in Chapter 3 having an aspect ratio $\Lambda \approx 200$.

2.3 Interacting systems

In the previous section the properties of an ideal Fermi gas in two and three dimensions were introduced. While this provides a useful starting point, rarely are ideal gases studied experimentally as many of their properties can be readily computed. Experiments conducted in this thesis aim to examine the effects of interactions on a two-dimensional system, a problem which remains computationally expensive or at times intractable beyond three-body systems. In the following sections the physics of low-energy scattering will be introduced and description of how the Feshbach resonance arises in quantum systems presented. Following this, pairing for both the two-

dimensional and three-dimensional cases will be introduced and finally the BCS-Bose crossover in both three dimensions and two dimensions will be discussed.

2.3.1 Scattering in 3D and 2D

Scattering experiments have been a fundamental tool in uncovering a wide range of new physics, from the early experiments by Rutherford [Rut11] in discovering the existence of the atomic nucleus with neutron scattering and by Bragg with X-ray scattering from crystal lattices [Bra13]. Scattering also plays a significant role in ultra-cold quantum gases.

Scattering processes belong to one of two classes, elastic or inelastic. An inelastic collision is simply an interaction between particles which results in an exchange of kinetic and internal energies between the interacting particles. Three-body recombination is an example of an inelastic collision in which three particles interact, two form a dimer molecule and the third required to help redistribute the kinetic energy from the binding energy of the dimer. In cold atom experiments such collisions are usually undesirable due to the enhanced heating and losses which arise. Elastic collisions, on the other hand, can be beneficial as they lead to the rethermalisation of atoms as required by commonly employed cooling techniques.

The dynamics of the particle to be scattered in the region of the scattering event can be overwhelmingly complex and the exact details are not always of interest, but rather it is the initial and final states of the particle outside of the interaction region which are of interest. To examine this, scattering problems are viewed in the asymptotic limit in which the interaction potential $V(\mathbf{r}) \to 0$; this limit is satisfied under the condition that $r \gg r_0$, where r_0 is the characteristic length scale of the interaction potential. For the problem of scattering of two particles with masses m_1 and m_2, where $m_1 = m_2 = m$, and position vectors $\mathbf{r_1}$ and $\mathbf{r_2}$, when the interaction potential $V(r)$ depends only on the magnitude of the distance $r = |\mathbf{r_1} - \mathbf{r_2}|$, the full Hamiltonian is separable and comprises of both contributions from the centre-of-mass and relative motion which can be solved independently.

The centre-of-mass motion of the particles is just that of a free particle with mass $2m$. Due to the potential having only a dependence on the relative separation r, the

problem of the relative motion is equivalent to the solution of the Schrödinger equation for a single particle with reduced mass m_r interacting with a spherically symmetric potential. The formulation of this problem is given by

$$-\frac{\hbar^2\nabla^2}{2m_r}\Psi(\mathbf{r})+V(\mathbf{r})\Psi(\mathbf{r})=E\Psi(\mathbf{r}) \tag{2.26}$$

where $m_r=\frac{m_1m_2}{(m_1+m_2)}$ is the reduced mass and $\mathbf{r}=\mathbf{r_1}-\mathbf{r_2}$ is the relative position vector between the two particles. Solutions for the relative motion contain both bound and continuum states which are of interest when examining scattering. Detailed analysis of such scattering problems are found in text-books and reviews such as [Tay72; Gio08; Ket07].

In the asymptotic limit the wavefunction Ψ is given by equation (2.27), in which the first term describes the plane wave of the incoming particle and the second term describes the spherically symmetric outgoing wave which arises due to the scattering event. In the low energy limit encountered at the low temperatures at which cold atom experiments are conducted, the analysis of the scattering problem can be accomplished by the method of partial wave expansion

$$\lim_{r\gg r0}\Psi(\mathbf{r})=e^{ik_zr}+f(k,\theta)\frac{e^{ikr}}{r} \tag{2.27}$$

where $f(k,\theta)$ is defined as the scattering amplitude, which describes the probability of detecting a particle scattered with momentum k at angle θ. The scattering amplitude $f(k,\theta)$ can be written as a superposition of Legendre polynomials

$$f(k,\theta)=\sum(2l+1)f_l(k)P_l(\cos\theta) \tag{2.28}$$

where l relates to the value of angular momentum of the scattering particle and the term $P_l(\cos\theta)$ are given by

$$P_l(\cos(\theta))=\sqrt{\frac{4\pi}{2l+1}}Y_{l,0} \tag{2.29}$$

due to the symmetry of $V(r)$, only the $Y_{l,0}$ spherical harmonic is required. In order

to determine the form of f_l which describe the partial wave scattering amplitude in equation (2.28) we can compare the incoming plane wave and the total wavefunction Ψ in the asymptotic limit and obtain

$$f_l(k) = \frac{e^{i\delta_l}}{k}\sin(\delta_l) = \frac{1}{k\cot\delta_l - ik}\,. \tag{2.30}$$

In ultracold gases the scattering energies are small enough that the centrifugal barrier which arises in the radial Schrödinger equation prevents higher order angular momentum states from contributing to the scattering process leaving only the *s*-wave ($l = 0$) momentum states. From equation (2.30) we can see that the scattering amplitude in this low energy limit is described entirely by the resulting *s*-wave phase shift δ_0 imparted on the wavefunction due to the interaction with the potential. From the scattering amplitude a number of parameters describing the scattering potential can be obtained by expressing the cot term in equation (2.30) via the effective range expansion [Bet49]

$$k\cot\delta = -\frac{1}{a} + \frac{1}{2}k^2 r_e + \mathcal{O}\left(k^4\right). \tag{2.31}$$

From this we can determine the *s*-wave scattering length a and effective range r_e of the potential. These terms describe the effective size of the scatterer and the distance over which the potential modifies the wavefunction of the scattering particles from the asymptotic limit. Using the above expansion the *s*-wave scattering amplitude can be rewritten as

$$f_0(k) = \frac{1}{-\frac{1}{a} + \frac{1}{2}k^2 r_e - ik}\,. \tag{2.32}$$

The total scattering cross section for the particle is defined as

$$\sigma = \int |f(k)|^2 \mathrm{d}\Omega \tag{2.33}$$

substituting equation (2.28) and solving the resulting integral the total cross section

including all angular momenta is

$$\sigma = \frac{4\pi}{k^2}\sum_{l=0}^{\infty}(2l+1)\sin^2\delta_l \tag{2.34}$$

and as we are limited to the s-wave ($l = 0$) case, the total scattering cross section becomes

$$\sigma = \frac{4\pi\sin^2\delta}{k^2} = \frac{4\pi a^2}{1+k^2a^2}\,. \tag{2.35}$$

For a two-dimensional system we can again determine the scattering length and scattering phase shifts. The next section follows closely the work of S. Adhikari [Adh86]. As with the three-dimensional scattering problem we are looking to solve the two-dimensional Schrödinger equation for two interacting particles

$$-\frac{\hbar^2\nabla^2}{2m_r}\Psi(\mathbf{r}) + V(\mathbf{r})\Psi(\mathbf{r}) = E\Psi(\mathbf{r}) \tag{2.36}$$

where m_r is the reduced mass of the system and $\mathbf{r}$ is the position vector which were defined previously. Assuming a cylindrically symmetric potential, equation (2.36) is separable and the solution for the wavefunction Ψ can be written as $\Psi(\mathbf{r}) = R(r)T(\theta)$. In the asymptotic region equation (2.36) becomes

$$\frac{1}{r}\frac{d}{dr}\left(r\frac{dR}{dr}\right) + \left(k^2 - \frac{m^2}{R^2}\right)R = 0 \tag{2.37}$$

and the wavefunction can be written as the sum of an incoming plane wave and an outgoing circular wave

$$\Psi(r,\theta) = \exp(ikx) + \sqrt{\frac{i}{8\pi k}}f(k)\frac{\exp(ikr)}{\sqrt{r}} \tag{2.38}$$

where the wavefunction contains the factor $r^{-1/2}$ rather than r^{-1} as in the three-dimensional case. This is to satisfy probability conservation of the outgoing circular wave. The scattering amplitude $f(k)$ can again be determined through the method of

partial waves resulting in a scattering amplitude of the form [Lev15]

$$f_l(k)_{2D} = \frac{-4}{\cot\delta_l(k) - i}\,. \tag{2.39}$$

Again due to the low energies of the scattering particles only the *s*-wave contributions to the phase shift need to be taken into account and the cot term can be expanded as in three dimensions [Lev15]

$$\cot\delta_s(k) = \frac{2}{\pi}\ln(ka_{2D}) + \mathcal{O}(k^2) \tag{2.40}$$

where k is the Fermi wave vector and a_{2D} is the two-dimensional *s*-wave scattering length, analogous to a in three dimensions. The scattering amplitude can then be written as

$$f_{2D}(k) = -\frac{4\pi}{2\ln(k_F a_{2D}) - i\pi}\,. \tag{2.41}$$

For experimentally realised systems the length scale of the van der Waals interaction between particles is much smaller than the typical harmonic oscillator length for an optical trap making the case for a quasi-two-dimensional system also useful to consider. Petrov *et al.* examined the alteration to the scattering properties in such an environment [Pet01]. Tight harmonic confinement in one direction results in the introduction of a new length scale into the description of the scattering processes l_z, which describes the characteristic harmonic oscillator length given as $l_z = \sqrt{\hbar m/\omega_z}$. The effective dimensionality of the scattering can be parameterised by the ratio l_z/a_{3D}. For the case in which $l_z/a_{3D} \ll -1$ the scattering processes are heavily influenced by the presence of the tight confinement. Conversely, for the case $l_z/a_{3D} \gg 1$ tightly bound dimers can be produced which interact as they would in three dimensions, albeit with minor alteration to their total scattering cross section. In this quasi-two-dimensional limit for low energy scattering such that $k \ll l_z^{-1}$ and $E \ll \hbar\omega_z$ [Pet01] the scattering

amplitude is

$$f(k) = \frac{4\pi}{\sqrt{2\pi} l_z / a_{3D} + \ln\left(B/\pi k^2 l_z^2\right) + i\pi} \tag{2.42}$$

where B is a dimensionless parameter given by $B = 0.905$ [Pet01], l_z is the harmonic oscillator length in the z direction and a_{3D} is the s-wave scattering length for particles in three dimensions. Comparing the scattering amplitudes for the pure two-dimensional and quasi-two-dimensional cases the two-dimensional scattering length can be found to be

$$a_{2D} = l_z \sqrt{\frac{\pi}{B}} \exp\left(-\sqrt{\frac{\pi}{2}} \frac{l_z}{a_{3D}}\right) \tag{2.43}$$

which depends entirely on the three-dimensional scattering properties and the characteristic length scale of the harmonic confining potential.

2.3.2 Feshbach resonances

With the framework of quantum scattering introduced in the previous section, the importance of the scattering length was emphasised due to its ability to fully parameterise the low energy scattering in ultracold gases. The ability to control this parameter is an important feature in cold atom experiments. This control is enabled by the Feshbach resonance. Detailed reviews of the Feshbach resonance are available in the following references [Chi10; Köh06]. This scattering resonance was discovered in the context of nuclear and atomic scattering by Feshbach and Fano [Fes58; Fan61] respectively, and provides to cold atom experiments a dial in which the interactions between particles can be precisely tuned. Predictions of the location of these resonances in alkali metals were first given by Tiesinga *et al.* for cesium [Tie93] and later for lithium and sodium by Moerdijk *et al.* [Moe95]. Experimental realisation of the scattering resonance in a number of elements soon followed [Hou98; Ino98; Zwi04].

In our experiments the atoms are equally populated in the two lowest hyperfine states. In ^{6}Li these are the $|F = 1/2, m_F = \pm 1/2\rangle$ states, where F and m_F are the total spin and the corresponding spin projection. For simplicity these states are labelled $|\uparrow\rangle$

and $|\downarrow\rangle$. When examining the scattering between two atoms in the presence of a magnetic field the effective Hamiltonian describing the system consists of contributions due to the hyperfine splitting and Zeeman shift in addition to the typical kinetic and potential terms.

In atoms with single valence electrons such as the alkali metals, the primary interaction at short-range is dominated by the interactions between the outer electron, where the interparticle interaction can be described using the Born-Oppenheimer approximation. The scattering potentials are parameterised by the quantum number $\mathbf{S} = \mathbf{s_1} + \mathbf{s_2}$ describing the total electron spin of the two-particle system. Here we have $\mathbf{S} = 0$ or 1 which result in either a singlet ${}^1\Sigma_g$ interaction or a triplet ${}^3\Sigma_u$ interaction potential. The interaction potentials are shown in figure 2.4 and are labeled as open if

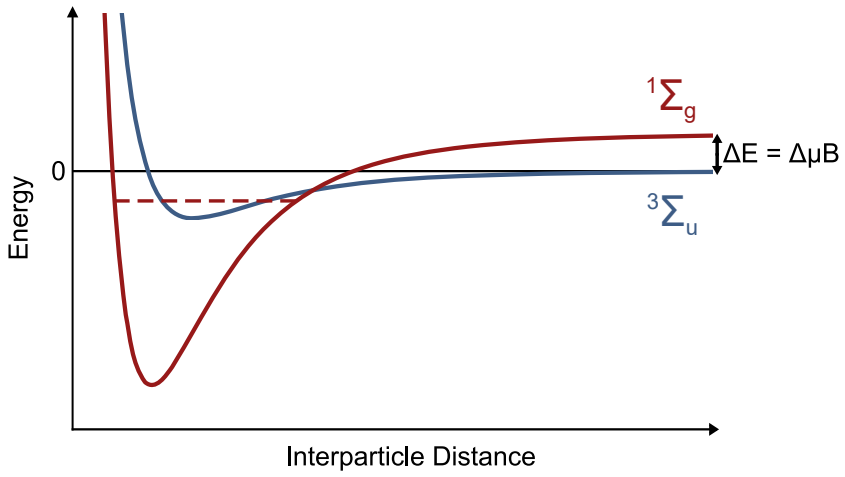

Figure 2.4: Scattering potentials seen by the colliding particles in the centre of mass representation. ${}^1\Sigma_g$ is the singlet potential and ${}^3\Sigma_u$ is the triplet potential. The two channels are split by an energy $\Delta E = \Delta\mu B$. By tuning the closed channel bound state energy it can be made resonant with the scattering energy of the particles.

in the asymptotic limit ($r \to \infty$) the energy is less than the energy E of the incoming particles and closed if the energy is greater than that of the particles. Due to the hyperfine interaction, there is coupling between the open and closed channels. Due to this coupling if there is a bound state in the closed channel near the energy of the scattering state, the particles can access a virtual transition from the open scattering state to the closed channel bound state before being returned to the open channel. The presence of this bound state leads to a resonance condition in which the scattering

length can be tuned through the resonance where $a_{3D} \to \infty$.

Tunability of the Feshbach resonance can be achieved either magnetically or optically [The04; Bau09]. In the experiment we access the Feshbach resonance through the application of a uniform magnetic field. Due to the difference in total spin between the singlet and triplet electronic states there is a difference in the total magnetic moment which allows tuning of one channel relative to the other through the application of a magnetic field. This allows the bound state in the closed channel to be tuned through resonance with the open channel continuum. By magnetically tuning the position of the bound state the scattering length obtains a dependence on the magnetic field and can be varied as [Moe95]

$$a(B) = a_{bg}\left(1 - \frac{\Delta B}{B - B_0}\right) \tag{2.44}$$

where a_{bg} is the background scattering length, B_0 is the resonance position and ΔB is the width of the resonance. Precise characterisation of the Feshbach resonance found the following values for ^{6}Li in the two lowest hyperfine states [Zür13], $a_{bg} = -1582a_0$, where a_0 is the Bohr radius, $\Delta B = -262.3\,\mathrm{G}$ and $B_0 = 832.2\,\mathrm{G}$. These parameters indicate a very broad Feshbach resonance. The scattering length through the resonance is shown in figure 2.5. The ability to control the interactions between particles of oppo-

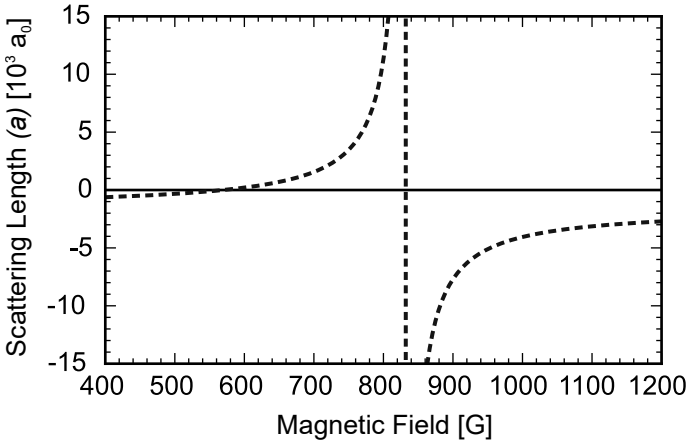

Figure 2.5: Scattering length as a function of applied magnetic field for the broad Feshbach resonance for spin mixture of ^{6}Li atoms in the lowest hyperfine levels of the 2S ground state.

site spin provides the ability to form long lasting pairs in the trap. Losses from three-

body recombination proved to be a significant challenge in bosonic systems [Ste99]. For fermionic systems such as ^{6}Li, three-body recombination is greatly reduced due to Pauli blocking [Pet04], making the Feshbach resonance an extremely powerful tool in Fermi gas research.

2.3.3 Pairing in 3D and 2D

In Section 2.3.1 the scattering properties of two particles were given for both two and three dimensions. Of significant importance is an understanding of the bound states which arise between two interacting particles. Pairing between two opposite spin fermions is fundamental in the emergence of condensation and superfluidity [Coo56; Bar57; Leg75]. There are fundamental differences in the physics describing the bound state properties between three dimensions and two dimensions. In three dimensions the existence of a bound state is predicated on the depth of the interaction potential exceeding a critical depth V_c [Ket07]. For two ^{6}Li atoms, the triplet potential is almost deep enough to support a new bound state, which gives rise to an anomalously large triplet scattering length $a_{bg} = -1582a_0$ [Ket07; Zür13]. In the presence of a Feshbach resonance, when the bound state energy $E_{res} \leq 0$, it becomes energetically favourable for the two particles to form a bound diatomic molecule [Köh06]. Near resonance, the binding energy E_B of these molecules is related to the scattering length by

$$E_B = \frac{\hbar^2}{m a_{3D}^2} \tag{2.45}$$

Figure 2.6 shows a number of differences between the evolution of the binding energy of pairs across two and three dimensions. In the two-body picture, in three dimensions pairing only occurs at $a_{3D} > 0$, which can be observed on the BEC side of the Feshbach resonance. For the region of the Feshbach resonance in which $a_{3D} < 0$ many-body effects permit the formation of weakly bound pairs which will be discussed in Section 2.4. The ability to adiabatically sweep through the Feshbach resonance in a Landau-Zener style ramp across an avoided crossing permits the transfer between free particles and bound diatomic molecules.

In two dimensions the continuum energy is increased by $\hbar\omega_z/2$ and a two-body

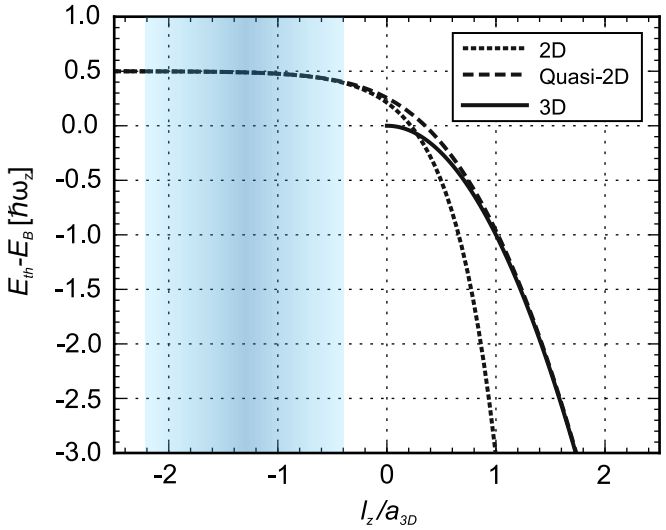

Figure 2.6: Binding energy for a 3D, 2D and quasi-2D Fermi gas through the Feshbach resonance. Immediate differences between two and three dimensions can be seen in the presence of a bound state for both the true and quasi-two-dimensional case for negative values of a_{3D}. As the pairs become more tightly bound and the impact of the transverse confinement becomes less significant for the scattering properties, the binding energy for the quasi-two-dimensional system merges with that of the pure three-dimensional gas. The shaded region represents the range of l_z/a_{3D} traversed in the experiments in Chapter 5.

bound state is present for any arbitrary attractive interaction. As in the three-dimensional case, for a pure two-dimensional Fermi gas the binding energy is given as

$$E_{B,2D} = \frac{\hbar^2}{m a_{2D}^2}. \tag{2.46}$$

In the quasi-two-dimensional regime the presence of the confining potential alters the binding energy. These energies can be determined through the solution of the following transcendental equation [Pet01; Blo08]

$$\frac{l_z}{a_{3D}} = \int_0^\infty \left[1 - \frac{\exp\left(-\frac{E_B}{\hbar\omega_z} u\right)}{\sqrt{(1-\exp(-2u))/2u}} \right] \frac{\mathrm{d}u}{\sqrt{4\pi u^3}} \tag{2.47}$$

the dependence of the binding energy on the *s*-wave scattering length for the quasi-two-dimensional case is shown as the dashed line in Figure 2.6. In the region where l_z/a_{3D} is negative, corresponding to the BCS side of the Feshbach resonance, the binding energy is qualitatively the same as a pure two-dimensional gas, progressing

through the Feshbach resonance as the scattering length a_{3D} becomes increasingly positive, and the binding energy is described by the three-dimensional result when the pair size becomes smaller than the characteristic length of the transverse harmonic oscillator.

In two dimensions the reason for the existence of this bound state can be obtained by examining the divergent behaviours caused by the modified density of states in two dimensions. By solving the Schrödinger equation in momentum space for the relative two-body motion, the binding energy can be solved through the relation [Ket07]

$$-\frac{1}{V_0} = \frac{m}{\hbar^2}\int_{q\leq\frac{1}{R}} \frac{\mathrm{d}^D q}{(2\pi)^D}\frac{1}{q^2+\kappa^2} = \frac{1}{\Omega}\int_{\varepsilon<E_R} \mathrm{d}\varepsilon \frac{g_D(\varepsilon)}{2\varepsilon+|E_B|} \tag{2.48}$$

where V_0 is related to the depth of the interaction potential. At low energies the interaction potential can be approximated by a contact interaction $V(\mathbf{r}) \approx V_0\delta(\mathbf{r})$ [Dal99b] where the Fourier transform $V(\mathbf{q})$ is constant for the low scattering energies up to a cut-off, $E_R = \frac{\hbar^2}{mR^2}$, where R is the size of the interaction potential. The momentum of the bound pair is $k = \sqrt{\frac{mE_B}{\hbar^2}}$, $q = \sqrt{\frac{2m\varepsilon}{\hbar^2}}$ is the momentum of the scattering particles, Ω is the system volume and g_D is the density of states for dimension D.

In the limit $V_0 \to 0$ the term on the left hand side of equation (2.48) diverges, for a bound state to exist the integral also needs to diverge with $E_B \to 0$. In two dimensions it has been shown that the density of states is constant where $g_{2D} = \frac{Am}{2\pi\hbar^2}$. Substituting this into the integral in equation (2.48) and solving gives $\frac{m}{4\pi\hbar^2}\ln\left(\frac{2E_R+E_B}{E_B}\right)$. As this solution processes a logarithmic divergence we have a bound state in two dimensions. While in three dimensions $g_{3D} = \frac{mV}{2\hbar^2\pi^2}\sqrt{\frac{2m\varepsilon}{\hbar^2}}$ which results in a finite solution to the integral disallowing a bound state below a critical potential depth [Ket07].

2.4 BCS-Bose crossover in 3D and 2D

In three dimensions, while the individual atoms within the gas are fermionic it is possible to access bosonic behaviour through the formation of diatomic molecules where the total spin of the molecule becomes integer and therefore the system is no longer described by Fermi-Dirac statistics but rather Bose-Einstein statistics. In a Fermi gas

which has an accessible Feshbach resonance it is possible to access both the fermionic and bosonic regimes. On the far BEC side of the resonance where the scattering length is small and positive, atoms of opposite spin may form molecules which exhibit weak repulsive interactions. On the other side of the Feshbach resonance in the limit of weak attractive interactions, pairing between particles is over distances much larger than the average interparticle spacing and these pairs are the well known Cooper pairs described by BCS theory [Bar57]. Both of these distinct regimes are smoothly connected in the middle where interparticle interactions are strongest. The region in which the *s*-wave scattering length $a_{3D} \to \infty$ is known as the unitary regime; here the atoms are very strongly interacting. This unique crossover behaviour has garnered significant theoretical and experimental interest [Zwe12].

During the formulation of the BCS theory, the question regarding the nature of pairing between two fermions was answered by Cooper [Coo56]. To solve this, the simplification of only considering the scattering of particles on top of a filled Fermi sea was made. It was shown that the presence of the filled Fermi sea allows pairing between atoms of opposite spin in three dimensions. At sufficiently low temperature these Cooper pairs can undergo a phase transition into the superfluid phase [Zwi05; Zwi06]. Returning to the criteria for the existence of a bound state in three dimensions, the ability to form weakly bound Cooper pairs in the presence of any arbitrary attractive interaction suggests likeness to the case of bound states in two dimensions. In three dimensions the presence of the filled Fermi sea limits the range of available energies for scattering to a thin shell at the Fermi surface resulting in an effective constant density of states which gives rise to the same divergences as was shown for two dimensions. This allows access to a two-body bound state. This necessity of attractive interactions means that the BCS limit can be obtained where $a_{3D} < 0$. On the other side of the Feshbach resonance where $a_{3D} > 0$, two atoms of opposite spin are allowed to form a stable bound state, with an increasing binding energy as $a_{3D} \to 0$. In this limit the molecule can be described by Bose-Einstein statistics and form a condensate at sufficiently low temperatures [Gre03; Zwi03; Joc03b]. The final limit which is important in the BEC-BCS crossover is at the pole of the Feshbach resonance where the scattering length diverges $a_{3D} = \infty$ and is known as the unitary limit. At this point the

interaction parameter $(k_F a_{3D})^{-1} = 0$ and the scattering cross section becomes independent of the scattering length taking on the value $\sigma = 4\pi/k^2$ and the only relevant parameter remaining is the interparticle spacing $n^{1/3}$.

In two dimensions the interaction parameter which characterises the crossover is no longer $1/k_F a_{3D}$ but $\ln(k_F a_{2D})$ which defines the position in the crossover. Due to the logarithmic dependence of the interaction parameter, in a two-dimensional Fermi gas the effect of changing the density, and by extension the value k_F, can lead to significant changes in the value $\ln(k_F a_{2D})$. This means that in a two-dimensional system there exists a density driven crossover and for a harmonically trapped gas which has a spatially varying density it is possible to span the crossover in a single trapped gas.

Similar to the three-dimensional Fermi gas the crossover in two dimensions has two distinct limits. The BCS limit occurs in two dimensions for values of the interaction parameter $\ln(k_F a_{2D}) \gg 1$. For $\ln(k_F a_{2D}) \ll -1$ the gas can be described in the bosonic limit. Between -1 and 1 the gas is in the strongly interacting regime. This strongly interacting region does not contain the same divergence in the scattering length as in three dimensions and the unitary regime in two dimensions occurs only for the trivial case where $a_{3D} \to 0$, or equivalently $a_{2D} \to \infty$.

Looking first at the BCS limit $\ln(k_F a_{2D}) \gg 1$ the gas can be described by BCS theory as in the three-dimensional case. In the BCS formalism the critical temperature indicating the onset of superfluidity is determined as [Miy83; Lev15]

$$\frac{T_C}{T_F} = \frac{2e^{\gamma}}{\pi k_F a_{2D}} \tag{2.49}$$

where $\gamma \approx 0.5772$ is Euler's constant. Further calculations by Petrov *et al.* found a critical temperature as above reduced by a factor of e^{γ} [Pet03]. Furthermore, it has been shown that for the case of the quasi-two-dimensional Fermi gas the value of the critical temperature increases as the gas approaches the transition from two to three dimensions [Fis14].

In the opposite limit $\ln(k_F a_{2D}) \ll -1$ the system can be increasingly described in terms of bosons. For a homogeneous gas in two dimensions, a gas can not become a strict BEC. The Mermin-Wagner-Hohenberg theorem states that for a two-

dimensional system at non-zero temperature, long-range order is forbidden due to thermal fluctuations [Mer66; Hoh67], precluding the formation of a condensate for a uniform system. However, this is not the case for a harmonically trapped system in which quasi-long range order can be obtained over the spatial extent of the trapped system. For a uniform system, while condensation is forbidden, superfluidity can still occur. This superfluid transition is manifested in the Berezinskii-Kosterlitz-Thouless (BKT) transition [Kos73; Ber72]. As density fluctuations are suppressed at low temperatures [San10] any excitations within the system predominately affect the phase [Had13]. This phase fluctuation is presented in the form of vortices, which have a phase circulation of $\pm 2\pi$ and vanishing density within the vortex core. Below the critical temperature the BKT phase is characterised by the binding of pairs of vortices with opposite circulation. These pairs result in the onset of a quasi-long range order in the gas and the first order correlation function decays algebraically [Had13]. Above the critical temperature T_{BKT} free vortices proliferate in the system. The BKT transition temperature for a weakly interacting Bose gas has been calculated as [Pet03]

$$\frac{T_{BKT}}{T_F} = \frac{1}{2}\left[\ln\left(\frac{C}{4\pi}\ln\left(\frac{4\pi}{k_F^2 a_{2D}^2}\right)\right)\right]^{-1} \tag{2.50}$$

where $C = 380$. Experimentally, the BKT transition has been observed in a two-dimensional Bose gas [Had06; Sch07] and indications of the BKT transition in a two-dimensional Fermi gas have been reported [Mur15]. Similar to the three-dimensional gas, calculation of the critical temperature in the strongly interacting region has eluded theorists but it is possible to interpolate between the BCS and BKT limits to obtain the possible phase diagram shown in figure 2.7. The first measurements of the phase diagram in a two-dimensional Fermi gas have be obtained by Ries *et al.* [Rie15a], in which they measure the critical temperature through the measurement of the momentum distribution which demonstrated signs of condensation. In the BCS regime they observe higher values of T_C then predicted. Future explorations of the phase diagram may wish to concentrate on this region. However, as will be shown in Chapter 4, experiments involving strong interactions will need to take into account the existence of additional transverse excitations in the gas.

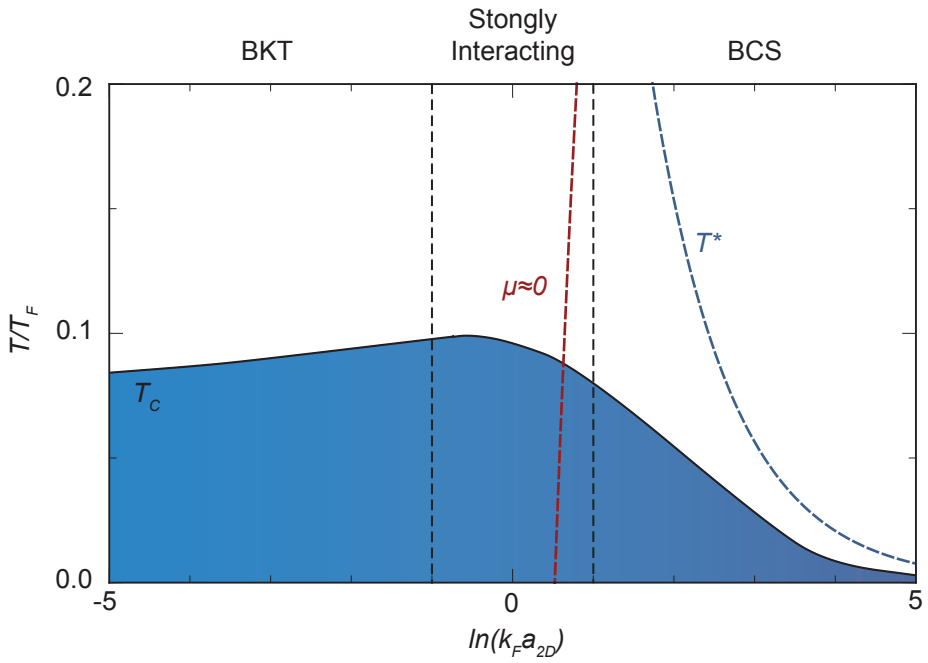

Figure 2.7: Phase diagram of the BCS-BKT crossover for two-dimensional Fermi gas. The solid black line denotes the calculated critical temperature. Between $-1 < \ln(k_F a_{2D}) < 1$ the critical temperature is interpolated between the BKT and BCS regions. The dashed blue line shows T^* which gives the temperature associated with the onset of pair formation. Figure adapted from [Lev15].

2.5 Summary

In this chapter the basic theory of degenerate Fermi gases was introduced, distinguishing a number of differences in the properties for both the ideal homogeneous and harmonically trapped gases when moving from three to two dimensions. The two-body physics focusing on the scattering properties in two and three dimensions was then introduced. Using this scattering framework the concept of the Feshbach resonance was introduced and the differences in the pairing physics in two and three dimensions were outlined. Finally, the behaviour of interacting systems was discussed in an examination of the BCS-BEC crossover in three dimensions and the analogous BCS-BKT crossover in two dimensions.

Chapter 3

Producing a two-dimensional Fermi gas

3.1 Introduction

The creation of an ultracold Fermi gas requires mastery of a number of techniques, involving ultra-high vacuum, electronics, optics and software. The experiments contained in this thesis involve the manipulation and measurement of ^{6}Li atoms prepared in the two lowest hyperfine states of the $2^2S_{1/2}$ ground state. Many of the experimental details discussed in the following sections have been covered in previous theses from our group. Details of the early generation of this experiment can be found in the following references [Fuc09; Vee09; Dyk10] with significant improvements to the experiment detailed in [Hoi14]. This thesis presents the first details of the development and implementation of a blue-detuned TEM_{01} mode optical trap within the Swinburne group. This chapter will begin with a brief discussion of the Fermi gas apparatus, followed by an introduction to the theory behind optical trapping in order to discuss the cooling and trapping techniques used to produced a degenerate Fermi gas in three dimensions. Details of the new TEM_{01} mode trapping potential are presented in Section 3.3.1 and the method used to produce a two-dimensional Fermi gas from an initial three-dimensional Fermi gas is outlined. Finally, in Section 3.4 the method of absorption imaging used to probe the atoms will be introduced and a technique for the calibration of the absolute density of the trapped gas. Using these tools it is

possible to begin to examine the nature of two-dimensional Fermi gases and explore the resulting thermodynamics in the following chapters.

3.2 Experimental setup

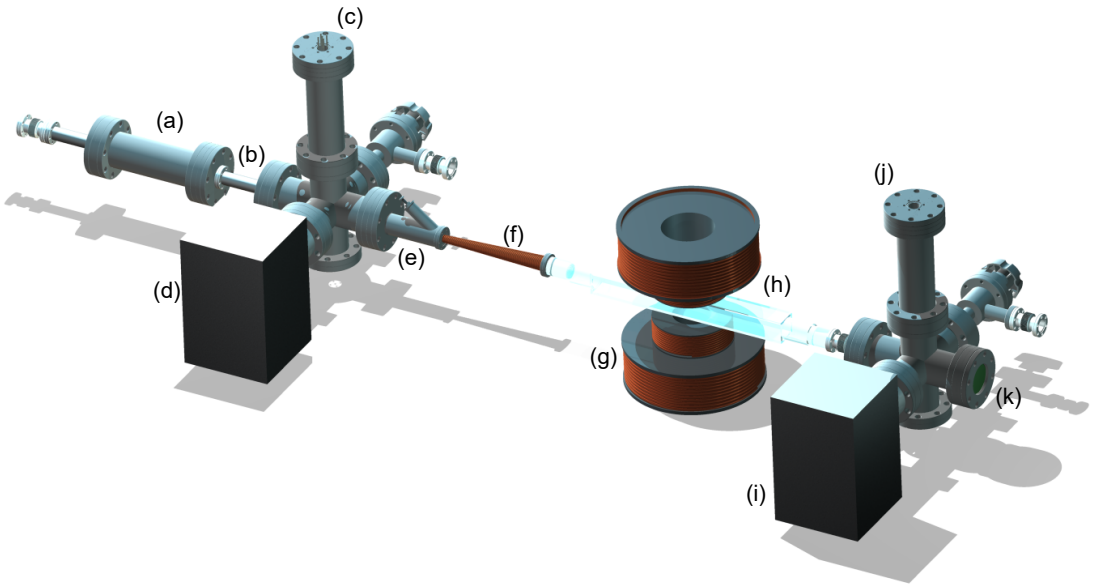

Figure 3.1: Experimental apparatus for producing a degenerate Fermi gas of ^{6}Li atoms. Beginning from the left the oven is located at position (a). The collimation tube which can be opened and closed via a pneumatic shutter is at (b). Elements (c) and (d) are the titanium sublimation pump and ion-pump. (e) is an in-line valve which separates the high-vacuum area on the oven side from the ultra-high vacuum on the experiment side. (f) is the Zeeman slower. The main coils at (g) are the MOT coils (outer set) and the Feshbach coils (inner set). (h) is the science cell a vycor quartz rectangular cell. An additional ion pump is at (i) and a getter pump at (j). Finally a sapphire window at (k) provides an entrance point for the Zeeman slower beam.

3.2.1 Producing a three-dimensional degenerate Fermi gas

In the following sections an overview of the main experimental systems which are used to produce a two-dimensional degenerate sample of ^{6}Li will be given. A thorough description of the laser setup used in the experiment can be found in the PhD thesis of Sascha Hoinka [Hoi14]. Following this, the concepts required to understand how a degenerate Fermi gas is produced will be introduced. For those familiar with

similar cold atom experiments our methodology is quite standard. Beginning with a source of solid lithium, which is heated in an oven at a temperature of approximately $360^{\circ}C$. The resulting atomic vapour through a collimation tube, which is opened with a pneumatically actuated shutter during the loading stage. The atomic beam is initially slowed through the use of a Zeeman slower allowing the magneto-optical trap (MOT) to capture a low-speed subset of the atoms from the atomic beam. The MOT loading time is on the order of 40 seconds which produces an atomic cloud of approximately 10^9 atoms. A 1075 nm focused dipole trap is then turned on and the magnetic field used to generate the MOT is increased leading to a compression of the MOT to enhance the transfer to the dipole trap. The MOT light is then switched off and the atoms are evaporatively cooled to a final temperature of approximately $0.1T_F$, with an overall atom number of approximately $N_\sigma = 2.5 \times 10^5$ by lowering the power of the dipole trap. We then transfer the atoms into the TEM_{01} mode trap. As the transfer and optimisation of the two-dimensional trap constitutes a new advancement for the experiment a detailed description of the process will be withheld until Section 3.3.

3.2.1.1 Optical traps for neutral atoms

The ability to cool and trap atoms with light has provided experimental physicists with a means to precisely manipulate atoms and to cool these atoms to previously unreachable temperatures. With early proposals to use light as a method of confining atoms [Ash70; Let79] the first realisations of such trapping and cooling schemes were developed in the mid 1980s [Phi85; Dal89] becoming an essential technique in cold atom experiments with a number of detailed reviews and textbooks published on this topic [Gri00; Met02; Foo04]. A semi-classical approach to describing the light-matter interaction is sufficient to describe the physics involved in trapping and cooling neutral atoms. Two components come into play within this description, the scattering force and the gradient (dipole) force. Both of these elements arise due to the light field's ability to induce an electric dipole moment on the atom. When this occurs the polarisation of the atom is

$$\vec{P} = \chi \vec{E} \tag{3.1}$$

where χ is the complex polarisability of the atom and $\vec{E}$ is the electric field vector of the incident light. The scattering force arises from the imaginary component of χ, which is a non-conservative friction-like force on the atom and allows cooling. Whereas the gradient force originates from the real component of the polarisability and allows the trapping of atoms [Ash97], the interaction potential between the atom and light is of the form of the dipole interaction

$$U_{dip} = -P.\vec{E}\,. \tag{3.2}$$

Substituting the atomic polarisability, the interaction potential is given by the square of the time-averaged electric field which is proportional to the intensity, giving an interaction potential [Gri00]

$$U_{dip} = -\frac{1}{2\varepsilon_0 c} Re(\chi) I \tag{3.3}$$

solving for the polarisability χ, the dipole potential and associated scattering rate are

$$U_{dip}(\mathbf{r}) = \frac{3\pi c^2}{2\omega_0}\left(\frac{\Gamma}{\omega_0-\omega}+\frac{\Gamma}{\omega_0+\omega}\right) I(\mathbf{r}) \tag{3.4}$$

$$\Gamma_{sc}(\mathbf{r}) = \frac{3\pi c^2}{2\hbar\omega_0^3}\left(\frac{\omega}{\omega_0}\right)^3\left(\frac{\Gamma}{\omega_0-\omega}+\frac{\Gamma}{\omega_0+\omega}\right)^2 I(\mathbf{r}) \tag{3.5}$$

where Γ is the natural linewidth of the transition, ω_0 is the transition frequency and ω is the frequency of the interacting light. As the term $\left(\frac{\Gamma}{\omega_0-\omega}\right)$ is typically larger than $\left(\frac{\Gamma}{\omega_0+\omega}\right)$, equations (3.4) and (3.5) can be approximated as

$$U_{dip}(\mathbf{r}) = \frac{3\pi c^2}{2\omega_0}\frac{\Gamma}{\Delta} I(\mathbf{r}) \tag{3.6}$$

$$\Gamma_{sc}(\mathbf{r}) = \frac{3\pi c^2}{2\hbar\omega_0^3}\left(\frac{\Gamma}{\Delta}^2 I(\mathbf{r})\right) \tag{3.7}$$

where $\Delta = \omega_0 - \omega$ is the detuning of the light from the transition frequency. Different behaviours can be observed depending on the sign of the detuning Δ. For red-detuned beams ($\Delta > 0$) the atoms experience an attractive potential. In this scenario the atoms are attracted to regions in the light field with the highest intensity. For the inverse

case of a blue-detuned beam ($\Delta < 0$) atoms experience a repulsive potential from the beam and are pushed into regions of minimum intensity. This property allows the manipulation of atoms by combining different geometry intensity distributions with either sign of the detuning depending on the desired goal.

3.2.1.2 Zeeman slower

The Zeeman slower is a common first-stage slowing technique used in cold atom experiments. First conclusive evidence of the deceleration of an atomic beam was found by Phillips and Metcalf [Phi82], since then it has become a core technique in the field. As mentioned in Section 3.2.1.1 in the semi-classical approach the imaginary part of the polarisation gives rise to the non-conservative scattering force which can result in the overall cooling and increase of the phase space density. When examining the physics of the Zeeman slower it is useful to use the quantum mechanical framework, in which the electromagnetic field of the laser is comprised of photons with momentum $p = \hbar k$. The ensemble of atoms in the Zeeman slower travel in the direction counter-propagating to the Zeeman slower beam with velocities described by a Maxwell-Boltzmann distribution.

A particular velocity component of the atomic beam will be resonant with the frequency of the photons in the slower beam and will undergo absorption and an exchange of momentum $\hbar k$. The total force felt by an atom is given by the product of the momentum of the photon p with the total number of photons scattered. For a two-level system, in the limit that the transition is saturated the atom spends an equal amount of time between the ground and excited states giving a maximum force on the atom

$$F_{\max} = \frac{\hbar k \Gamma}{2}. \tag{3.8}$$

While the atom will also undergo spontaneous emission, these photons are emitted isotropically and the time averaged change to the atom's momentum is zero.

Due to the Doppler shift of the transition frequency as the velocity of the atoms changes, atoms which were once resonant with the laser field will be shifted away from

resonance by an amount proportional to the change in the atoms velocity Δv. With a large enough shift the atoms will no longer interact with the laser field. To overcome this, a spatially varying magnetic field is applied along the length of the Zeeman slower. This magnetic field shifts the transition frequency of the initially resonant velocity component back into resonance with the laser as the atom's velocity is reduced. Upon exiting the oven the average velocity of the atoms is approximately $1730\,\mathrm{m\,s^{-1}}$. Prior to entering the capture volume of the magneto-optical trap the average velocity of the atoms is on the order of tens of meters per second.

3.2.1.3 Magneto-optical trap

The second stage of cooling is provided by the magneto-optical trap (MOT). The MOT is another standard laser cooling technique which has been demonstrated to achieve sub-Doppler temperatures [Raa87]. The experiment implements a 3D MOT consisting of three pairs of counter-propagating laser beams. Each pair of beams consists of one beam with σ^+ polarisation and one with σ^- polarisation. The layout of these beams in relation to the main science cell is shown in figure 3.2. By applying a quadrupole

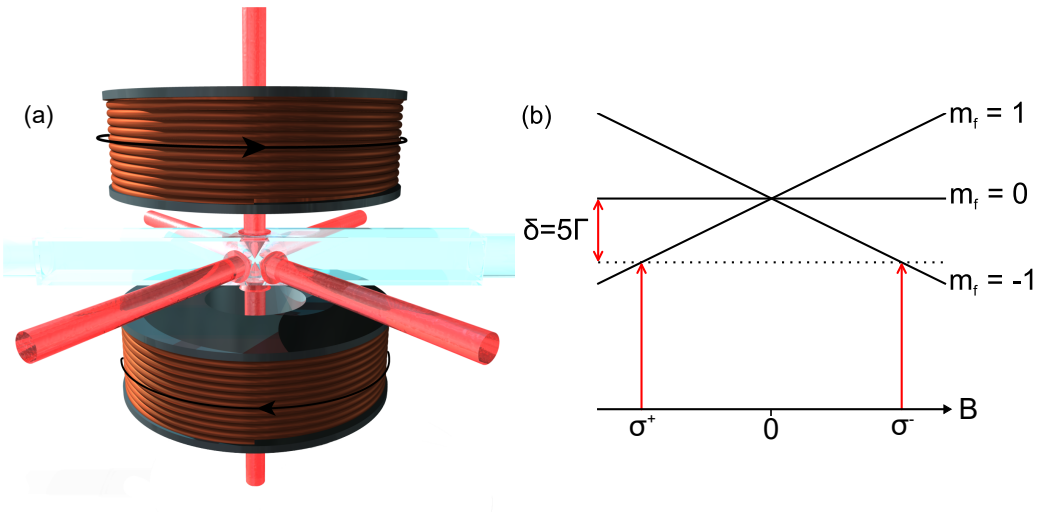

Figure 3.2: Figure (a) shows the basic layout and orientation of the 6 MOT beams and MOT coil placement. The direction of current in each coil is indicated by the black arrow. Figure (b) demonstrates the general principle of the MOT in 1D. Any atom travelling outward from the field minima will experience a shift in energy levels and will become resonant with the beam in the counter-propagating direction.

magnetic field generated in a pair of anti-Helmholtz configured coils the magnetic field

goes to zero halfway between the coils which we define as our trap centre. Atoms travelling outward from this minimum will experience an increasing magnetic field and a subsequent shift in their transition frequency due to the Zeeman shift caused by the magnetic field, resulting in the atom becoming resonant with light in the co-propagating direction, as shown in figure 3.2. The light is polarised in such a way to conform with the selection rules for the desired atomic transition due to the lifted degeneracy of the sub-levels in the presence of the magnetic field. This configuration allows us to preferentially slow and return into the capture volume only those atoms which are escaping.

For our experiment, cooling occurs on the D_2-line between the $|F = 3/2\rangle$ and $|F' = 5/2\rangle$ states. However, it is also possible to cool on the D_1-line [Rio12; Gri13; Bur14]. Due to the linewidth of the lasers there can be additional excitation into the $|F' = 3/2\rangle$ state from where the atoms can decay to the $|F = 1/2\rangle$ ground state. Atoms in this state are no longer resonant with the cooling laser and are removed from the cooling process. To circumvent this, re-pumper light is used to pump the atoms out of the $|F = 1/2\rangle$ dark state and allow them to once again be part of the cooling process. The potential formed by the MOT is on the order of millikelvins and only a low velocity subset of all the atoms leaving the Zeeman slower are able to be captured. Despite this, after a loading time of approximately 40 seconds we achieve an atom number on the order of 10^9 and temperatures of order $280\,\mu K$ [Dyk10]. The final stage in the MOT loading procedure is compression, which occurs a short time after the application of a single-beam dipole trap. Compression is achieved by increasing the current in the MOT coils causing the magnetic field strength to increase, resulting in an increased density which enhances the transfer efficiency from the MOT to the dipole trap in preparation for the final cooling stage. Additionally, during this final stage the MOT laser is tuned closer to resonance to maximise cooling towards the Doppler limit.

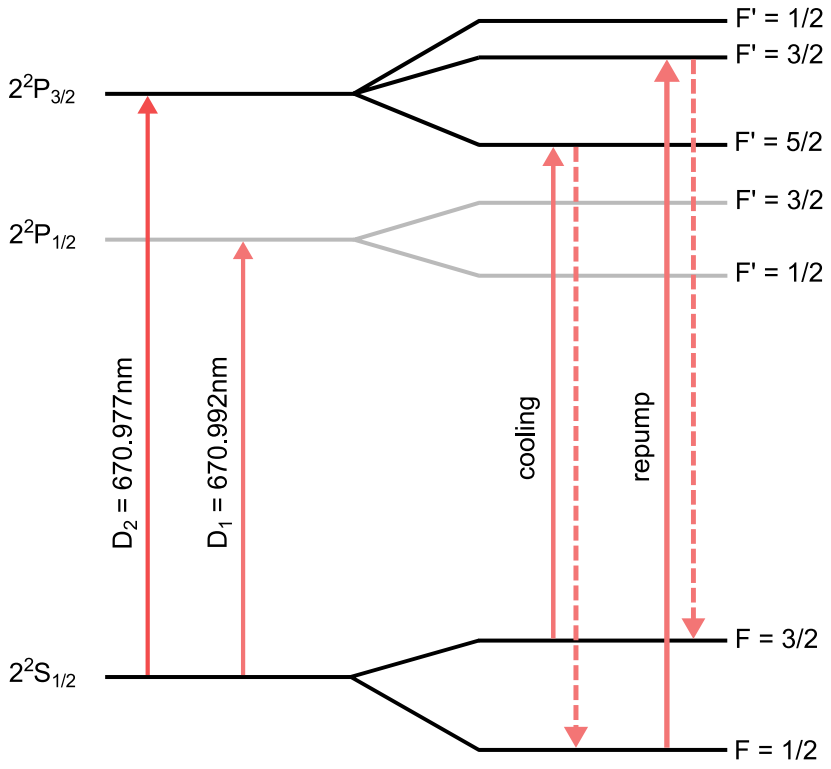

Figure 3.3: Energy level splitting for fine and hyperfine structure in ^{6}Li at zero magnetic field.

3.2.1.4 Dipole trap and evaporative cooling

The final stage of cooling is evaporative cooling in a high power red-detuned dipole trap. The trap is produced with a 1075 nm fibre laser,[1] with a maximum output power of 100 W. Intensity control of this laser is provided by the use of an acousto-optical modulator, controlled directly by the main LabView control panel at high power. At powers below 13 W the AOM is controlled by an external PID controller. This laser is focused down to a radius of 38 μm at the position of the magnetic field minimum in order to collect atoms from the densest region of the compressed MOT.

In the presence of the strong electric field created by the laser, as the laser frequency is red-detuned, the atoms are attracted to the high-intensity regions of the beam. As the laser is very far detuned the scattering of photons is reduced as we

[1] IPG YLR-100

aim to minimise residual heating effects. The potential felt by the atoms is set by the approximately Gaussian intensity of the laser. In the low temperature limit, the atoms will mostly experience the lowest regions of the potential which approximates a harmonic potential and is given as [Gri00]

$$U_{dip}(\mathbf{r}) \approx -U_0\left[1-2\left(\frac{r}{\omega_0}\right)^2-\left(\frac{z}{z_R}\right)^2\right]. \tag{3.9}$$

The process of evaporation occurs as the total power of the dipole trap is reduced. As the laser power is reduced the trapping potential felt by the atoms decreases proportionally, allowing high energy atoms to escape the trap. This process amounts to cutting off the high energy tail of the Boltzmann distribution. After rethermalisation through elastic collisions the gas reaches a lower equilibrium temperature. As colli-

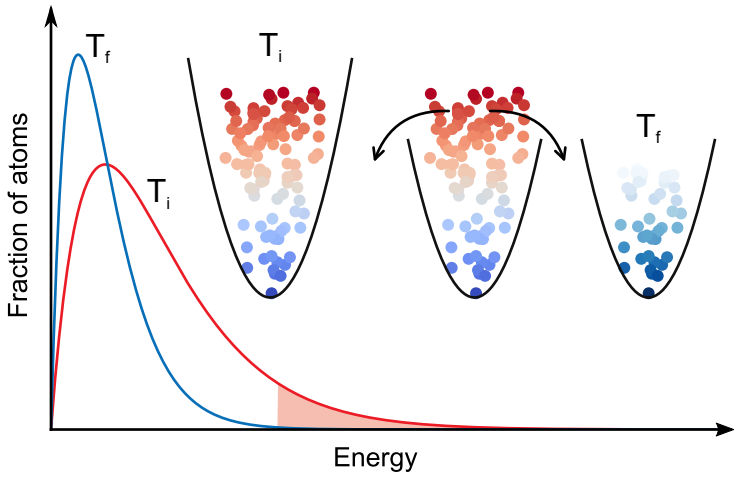

Figure 3.4: Cartoon depicting the basic process of evaporative cooling. At the initial temperature T_i the trapping potential is at its maximum and all atoms are confined. By lowering the trapping potential we are allowing the high energy particles with energies in the shaded area of the tail of the Boltzmann distribution to escape. The atoms are then allowed to undergo elastic collisions and rethermalise resulting in a lower average energy with a new Maxwell-Boltzmann distribution given by temperature T_f.

sions are crucial for the rethermalisation process, we perform the evaporation process near the pole of the Feshbach resonance at 790 G where the interactions between particles are significant. Due to the shallow trapping potential at the end of the evaporation ramp, to avoid unnecessary additional losses it is optimal to transfer the atoms to their final trap, which in previous experiments on three-dimensional gases has been another

single beam dipole trap and in the two-dimensional case the atoms are transfered to the new TEM_{01} trap.

3.3 Reaching two dimensions

3.3.1 The two-dimensional trapping potential

There have been a number of trapping potentials designed with the goal of producing and confining a single or set of layered two-dimensional quantum gases. Optical lattices have been favoured by a number of groups [Bur01; Yef11; Mar10; Rie15b] due to their relative simplicity in design, only requiring two beams which produce an interference pattern that provides the trapping potential. Its simplicity may be complicated by the fact that one has to then be confined to either imaging from the side of the trap or to image over a number of lattice sites, eliminating a fundamental advantage of two-dimensional systems; the ability to image the true atomic density distribution. This disadvantage can be eliminated by depopulating all but one of the lattice sites as done by [Rie15b; Mor14].

In order to create a single two-dimensional Fermi gas with a high level of repeatability we generate a TEM_{01} mode blue-detuned optical trap using a home-made π phase plate as in [Mey05]. For an ideal TEM_{01} mode trapping potential the need to depopulate additional sites is not required. The following sections detail the theoretical background of the trap, the measured trap parameters, the loading sequence used to transfer from the three-dimensional trap to the TEM_{01} mode trap while avoiding populating additional lobes and additional magnetic evaporation to reduce the total atom number N in a controlled manner.

3.3.2 Theoretical description

The electric field produced by a transverse electric mode with radial and axial mode numbers, l and m is given by [Sal07]

$$E(x,y,z) = A_{l,m}\frac{W_0}{W_{x,z}}H_l\left(\frac{\sqrt{2}x}{W_{x,z}(y)}\right)H_m\left(\frac{\sqrt{2}z}{W_{x,z}(y)}\right)\exp\left[-i(\frac{x^2+z^2}{2R(y)})+(l+m+1)\zeta(y)\right] \tag{3.10}$$

where $A_{l,m}$ is the amplitude of the electric field, $H_{l(m)}$ are the Hermite-Gaussian functions, $W_{x,z}(y)$ are the beam waist sizes in the x and z directions, $R(y)$ is the radius of curvature of the beam and $\zeta(y)$ is the Riemann zeta function. From equation 3.10 the intensity distribution can be written as

$$I_{l,m}(x,y,z) = |A_{l,m}|^2\left(\frac{W_0}{W_{x,z}(y)}\right)H_l^2\left(\frac{\sqrt{2}x}{W_{x,z}(y)}\right)H_m^2\left(\frac{\sqrt{2}z}{W_{x,z}(y)}\right). \tag{3.11}$$

The trapping geometry we create is ideally that of a TEM_{01} mode. By setting the mode indices $l=0$, $m=1$ in equation (3.11) we can write the intensity distribution as

$$I_{0,1}(x,y,z) = \frac{8Pz^2}{W_x(y)W_z^3(y)}\exp\left[-\frac{2x^2}{W_x^2(y)}-\frac{2z^2}{W_z^2(y)}\right]. \tag{3.12}$$

The waist sizes W_z and W_x are important characteristics of the trap as, in conjunction with the overall beam power, they set the values of the trapping frequencies ω_r and ω_z. Inserting the TEM_{01} mode intensity distribution in equation (3.11) into the definition of the dipole potential given in equation (3.2) we can define the optical trapping potential

$$U_{dipole} = -\frac{3\pi c^2}{2\omega_0^3}\left(\frac{\Gamma}{\omega_0-\omega}+\frac{\Gamma}{\omega_0+\omega}\right)I_{0,1}(x,z) \tag{3.13}$$

$$= U_0\frac{2z^2}{W_z^2}\exp\left(-\frac{2x^2}{W_x^2}-\frac{2z^2}{W_z^2}\right) \tag{3.14}$$

where U_0 is the central trap depth and is given as

$$U_0 = \frac{6c^2 P\left(\frac{\Gamma}{\omega_0-\omega} + \frac{\Gamma}{\omega_0+\omega}\right)}{W_x W_z \omega_0^3} \tag{3.15}$$

where c is the speed of light in vacuum, P is the trap power, Γ is the natural line width of the transition, ω_0 is the transition frequency and ω is the frequency of the laser used to provide the trapping. Finally, the trapping frequencies at the focus of the beam can be determined by Taylor expanding the desired direction around zero to second order and equating the result to the harmonic oscillator potential $m\omega^2 j^2/2$, where j is the direction of interest (x, y, z) and are given for all three directions as [Mey05]

$$\frac{\omega_z}{2\pi} = \sqrt{\frac{U_0}{\pi^2 m W_z^2}} \tag{3.16}$$

$$\frac{\omega_x}{2\pi} = \frac{i}{\sqrt{2}\pi}\frac{1}{W_x\sqrt{W_y}}\left(\frac{U_0}{\pi^2 m W_y^2}\right)^{1/4} \tag{3.17}$$

$$\frac{\omega_y}{2\pi} = \sqrt{\frac{3}{2}}\frac{i}{2\pi^2}\frac{\lambda}{W_x^{5/2}}\left(\frac{U_0}{\pi^2 m W_z^2}\right)^{1/4} \tag{3.18}$$

where ω_z is the trapping frequency in the tight (transverse) direction, and ω_x and ω_y are the trapping frequencies of the two orthogonal directions in the radial plane. The total trapping frequency in the radial direction is the geometric mean of frequencies in the radial directions giving $\omega_{r,optical} = \sqrt{\omega_x \omega_y}$. It should be noted that this trap actually provides a small amount of anti-trapping to the atoms in the radial directions x and y as indicated by the imaginary trap frequencies ω_x and ω_y. This anti-trapping arises from the Gaussian intensity distributions in the x and y directions. It is therefore important to add an additional form of trapping in the radial direction. In this case such a potential is produced by the residual magnetic field curvature provided by the Helmholtz configured Feshbach coils, which results in a harmonic potential with a frequency $\omega_B/2\pi = 24.5\,\text{Hz}$ for a field of 832.2 G. The final effective trap frequency in the radial direction is

$$\omega_r = \sqrt{\omega_B^2 + \omega_{r,optical}^2}. \tag{3.19}$$

For a laser power of 5 W at the position of the atoms and nominal beam widths of $W_z = 10\,\mu\text{m}$ and $W_x = 2000\,\mu\text{m}$, the trap frequencies we expect are

$$\frac{\omega_z}{2\pi} = 5.23\,\text{kHz} \tag{3.20}$$

$$\frac{\omega_x}{2\pi} = 2.15\text{i}\,\text{Hz} \tag{3.21}$$

$$\frac{\omega_y}{2\pi} = 3.81\text{i}\,\text{Hz} \tag{3.22}$$

From the values listed above it is clear that the level of anti-trapping provided by the optical trap will be dominated by the magnetic field. When combined with the magnetic curvature the final radial trap frequency is $\omega_r/2\pi = 24.38\,\text{Hz}$.

3.3.3 Producing the trap

There are multiple ways to generate a TEM_{01} mode optical trap. Optical resonators can be aligned to preferentially generate higher-order modes and holographic methods utilising spatial light modulators (SLM) [Hec92] are a reliable method to generate new phases in the beam. These devices are limited by their low damage thresholds, as the power of our trap can be up to $4\,\text{W}\,\text{cm}^{-2}$ at the position of the phase alteration spatial light modulators were not a viable option. The method chosen is the manipulation of the phase of the laser with refractive elements, which is a robust method to generate higher order modes [Bei94]. To produce a TEM_{01} mode a π phase shift needs to be induced in half of the beam. Such a phase plate has been used in other experiments [Mey05]. The basic design of the phase plate is straight forward and is outlined in figure 3.5. It consists of a regular one-inch optical flat made of BK7 glass, on which one-half has been coated with approximately 700 nm of MgF_2 which has a refractive index $n = 1.3789$ for the wavelength of light we use for the trap (532 nm). This π relative phase shift results in destructive interference at the interface around the mid-point of the optical flat which produces a region of zero intensity. It is in this resulting node that the atoms will be confined. While the phase plate is the key element in producing the TEM_{01} mode for the trap, additional optical elements are required to create the desired trap. The full optical setup is presented in figure 3.6.

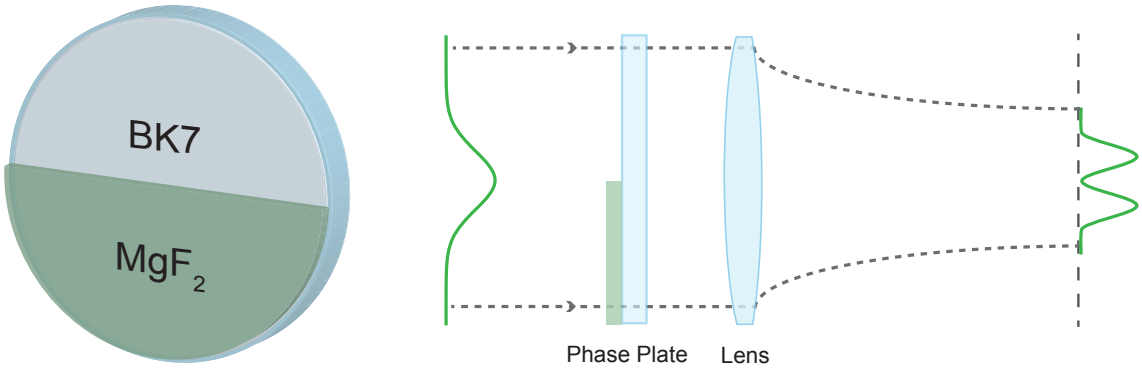

Figure 3.5: Phase plate used to generate a TEM_{01} mode beam. The lower half of the optical flat has a coating of $\sim 700\,nm$ of MgF_2. This coating results in the required π phase shift to half of the beam. Taking an initially Gaussian beam and passing through the phase plate and lens system results in a nearly TEM_{01} intensity distribution in the far-field.

Our trapping light is provided by a 532 nm fibre laser.[2] An acousto-optical modulator (AOM) is then used in conjunction with a PI controller to provide intensity stabilisation and control. We select the first order from the AOM and deflect the zeroth and any additional orders to a beam dump. Due to distortions of the beam caused by the AOM we spatially filter the beam by focusing it through a 50 µm pinhole resulting in a highly Gaussian beam at the output. An additional aperture is used to remove any Airy ring structure present after the spatial filtering. The beam is then re-collimated with a 300 mm achromat to a diameter of approximately 25 mm. The re-collimated beam passes through the phase plate and a 1000 mm cylindrical lens which focuses the beam in the horizontal plane. Before the final steering mirror an aperture is used to further filter the beam. This aperture can be used to adjust the final beam waist in the transverse direction, where a smaller aperture diameter results in a larger transverse waist but a more homogeneous intensity distribution and a larger aperture diameter gives a tighter waist with the potential introduction of fringes in the intensity distribution. It is important to note that the final choice of aperture size and its alignment is crucial to achieving an intensity distribution which is uniform in both nodes of the TEM_{01} mode.

The final lens before the science cell is a 50 mm diameter, 200 mm focal length achromat which collimates the beam in the horizontal direction and focuses the beam

[2] IPG GLR-20

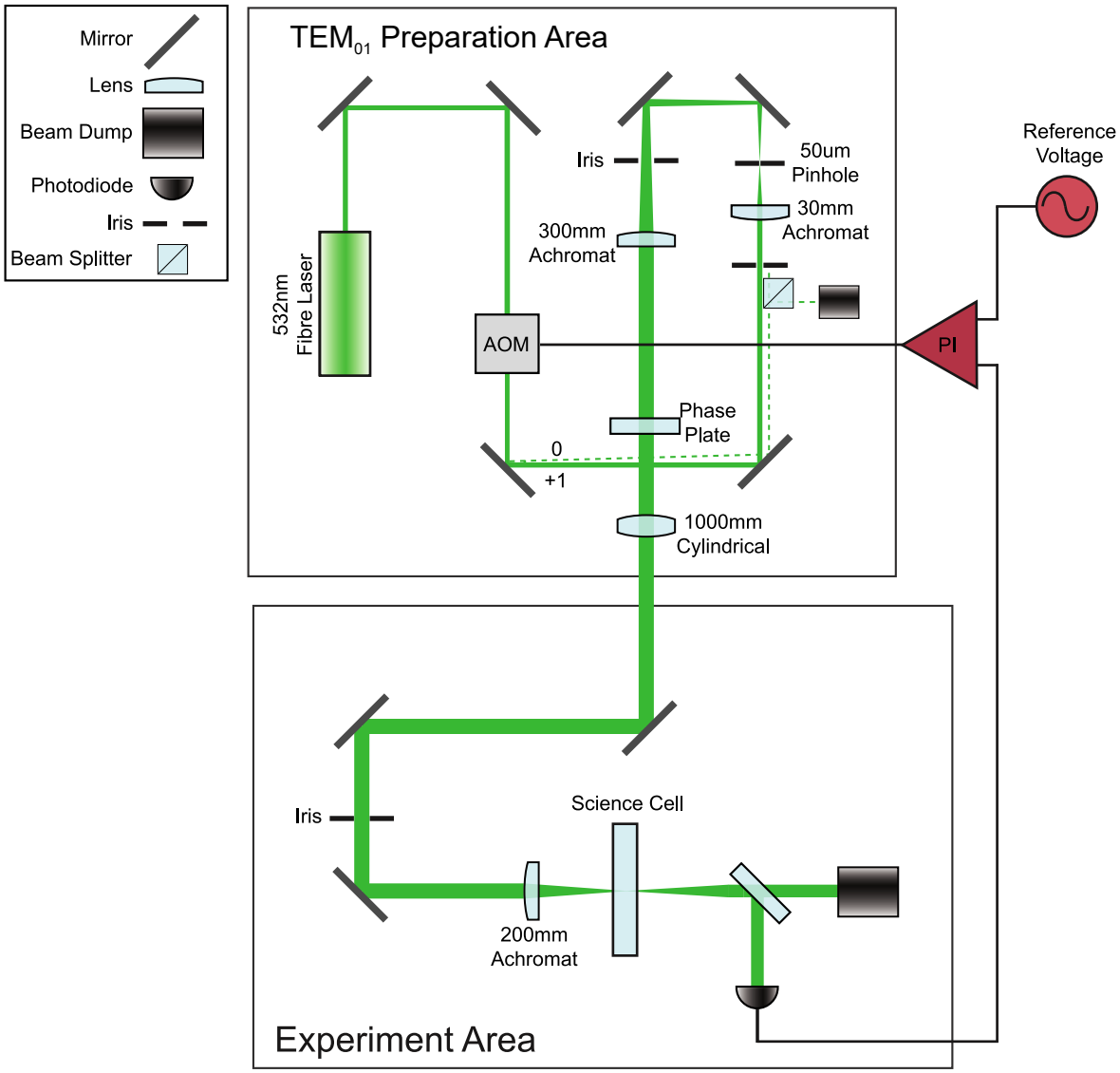

Figure 3.6: A separate breadboard contains the optical elements to generate the TEM_{01} mode beam. The intensity of the laser is controlled by an AOM, we block all orders from the AOM except for the +1 order which is spatially filtered and re-collimated before the phase plate. The beam is focused in the horizontal direction by a long focal length cylindrical lens. A final aperture filters the beam before it is focused in the tight direction by the final $f = 200\,\text{mm}$ achromat.

in the transverse direction with its focal point located at the position of the atoms in the 3D dipole trap. After the science cell we pick off a small amount of the light and direct it onto a photodiode which provides the PI controller with a feedback signal, while the majority of the light is directed to a beam dump.

3.3.3.1 Beam Profiling

As the quality of the TEM_{01} mode is sensitive to a number of criteria; co-axial propagation relative to the phase plate, final aperture size and beam centreing on the final aperture, it is necessary to profile the beam and make accurate measurements of the intensity distribution before attempting to trap atoms. When considering what constitutes good alignment we require the intensity distribution of the TEM_{01} mode to be uniform and evenly distributed between the two anti-nodes of the TEM_{01} mode through the focal region and over a propagation range larger than the expected Fermi radius. This is to ensure a uniform confinement frequency is felt across the atoms. To ensure this, the beam is imaged over a range of $\pm 500\,\mu m$ from the focus in steps of $50\,\mu m$. The experimental setup for this procedure is shown in figure 3.7. Due to the

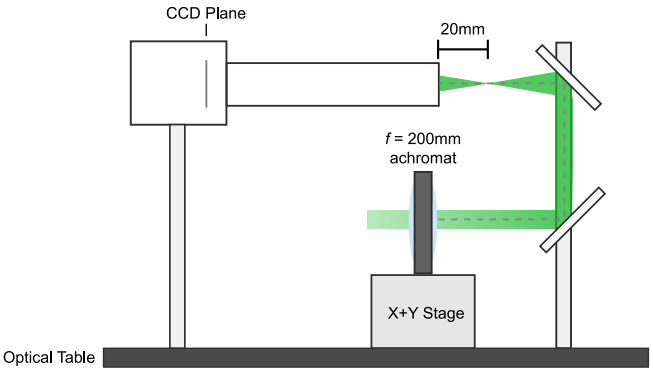

Figure 3.7: Optical setup used to measure the TEM_{01} profile. We image a range throughout the focused beam onto a CCD. The dashed grey line is the total distance between the lens and working distance of the microscope objective. This distance is the focal length of the lens $f = 200\,mm$.

limited space near the science cell, a periscope is used to reflect the beam back towards a CCD camera with an attached microscope objective, with a lens tube allowing for adjustable magnification. With these images we can generate a surface of the intensity distribution. From these measurements we confirm that the difference in intensity between the two nodes is approximately 3%, which suggests that anharmonicity in the trapping potential should be small. We can also examine the waist size as a function of position as shown in figure 3.8. With a measured tight waist $W_z \approx 10\,\mu m$ and radial waist $W_r \approx 2\,mm$ it is possible to estimate our critical atom number $N_{2D} \approx 3.9 \times 10^5$ using equation (2.25). Despite this estimate, it will be the measured trap frequencies

which define our final N_{2D}. A technical aside which concerns the particular equip-

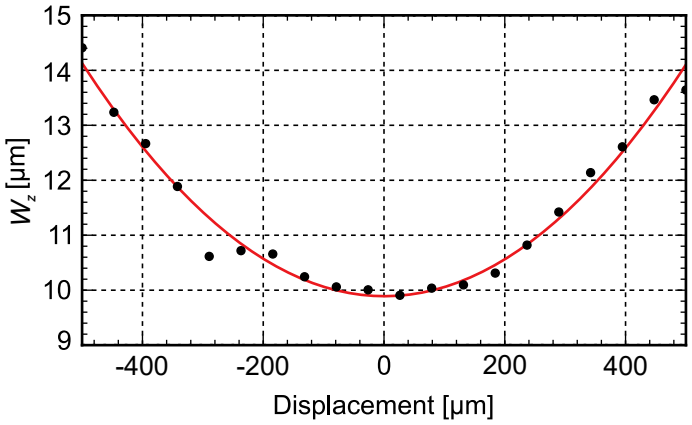

Figure 3.8: Measured transverse waist size as a function of displacement from the focal plane.

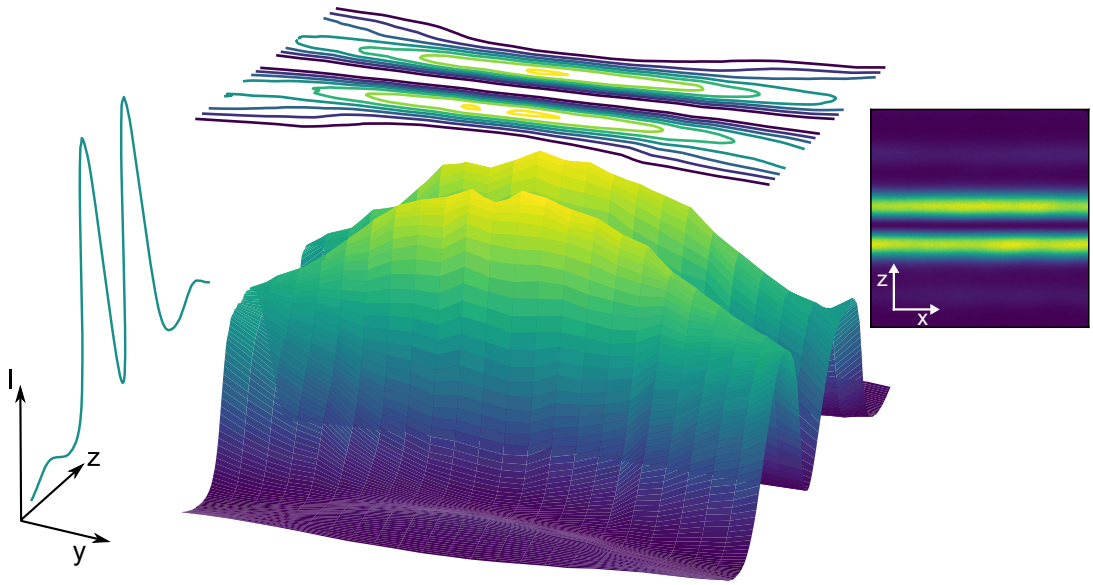

Figure 3.9: Surface plot of the intensity profile of the TEM_{01} mode through the focus. The result of precise alignment can be seen as the measured intensity distribution is approximately the same for the two anti-nodes. The inset image on the right is a portion of the beam as seen from the camera.

ment used in this experiment is the effect of temperature of both the laser head and the AOM. It has been observed that there is a significant shift in the beam pointing of the laser when the output head temperature increases. This is noticeable when running the IPG-GLR20 at powers greater than 10 W causing a noticeable decrease in efficiency through the 50 µm pinhole used for spatial filtering which may eventually damage the pinhole, degrading the Gaussian profile of the beam after the pinhole. It

has also been seen that a beam pointing drift occurs when the AOM increases in temperature due to the application of a continuous RF signal. This should be kept in mind during the alignment of the trap to ensure that a reliable trapping potential is created during the continuous operation of the experiment. Failure to account for these drifts results in a reduction of the overall power inside the glass cell when the laser head and AOM reach thermal equilibrium. These drifts can be recognised by monitoring the signal from the final photo-diode which is sent to the PID circuit. When the signal fails to reach the set-point this usually indicates the beam-pointing has changed.

3.3.3.2 Trap frequency measurements

While estimates for the trapping frequency can be obtained from the size of the beam waists in the transverse and radial directions, the actual value of the trap frequency can be shifted due to imperfections in the trapping potential and misalignment. Measurement of the transverse trap frequency and damping allow the benchmarking and optimisation of the trap's final alignment.

In order to measure the transverse trap frequency we induce an oscillation in the centre of mass in the tightly confined z dimension. To do this we begin with the atoms initially confined to the TEM_{01} mode optical trap. To induce oscillations in the centre of mass motion of the atoms, the atoms are perturbed through the application of a strong magnetic field gradient, turned on linearly over 20 ms. The power of the trapping laser is suddenly decreased from 5 W to 2.5 W and held for 10 ms before being suddenly returned to full strength. After a variable hold time τ the atoms are released and imaged after 1.2 ms time of flight. The center of mass in the transverse direction is measured from the resultant absorption image.

For a power of 5 W at the location of the atoms a trap frequency of 5.15(1) kHz is found, in good agreement with the ideal value found in Section 3.3.3.1 and the damping time for the trap is $\tau = 4.4(5)$ ms. The trap frequency measurements for both the transverse and radial directions are given in figures 3.10 and 3.11.

With a knowledge of the power of the trap at the site of the atoms and the resulting trap frequency one can iteratively alter the trap position until a maximum is found. We find the trap frequency does not change significantly over a range of approxi-

mately ±150 µm. The damping time of the oscillations on the other hand is sensitive to changes on the order of 25 µm. Maximising both of these parameters places the trap in the optimal alignment for creating a two-dimensional Fermi gas. Because the criti-

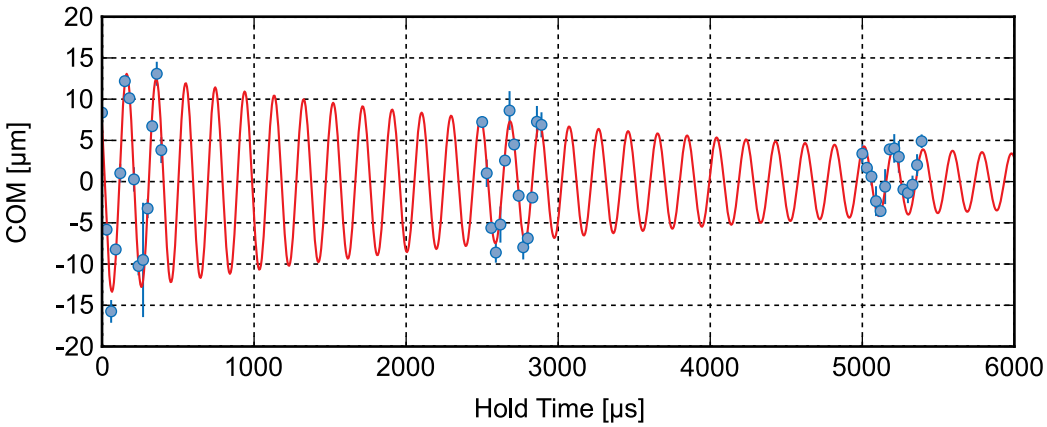

Figure 3.10: Transverse trap frequency for a power of 5 W. Each point is the average of three measurements and the error bar is given by the standard deviation.

cal atom number N_{2D} of our two-dimensional trap relies on the ratio of the tight and radial trapping frequencies, as we move around the Feshbach resonance by altering our magnetic field we simultaneously change the curvature of the magnetic field and therefore change the strength of the radial confinement. Because of this, it is important to know how the radial trap frequencies changes with magnetic field. A similar procedure to that used in the measurement of the transverse trap frequency is used to measure the radial trapping frequencies. Oscillations in the radial direction are again

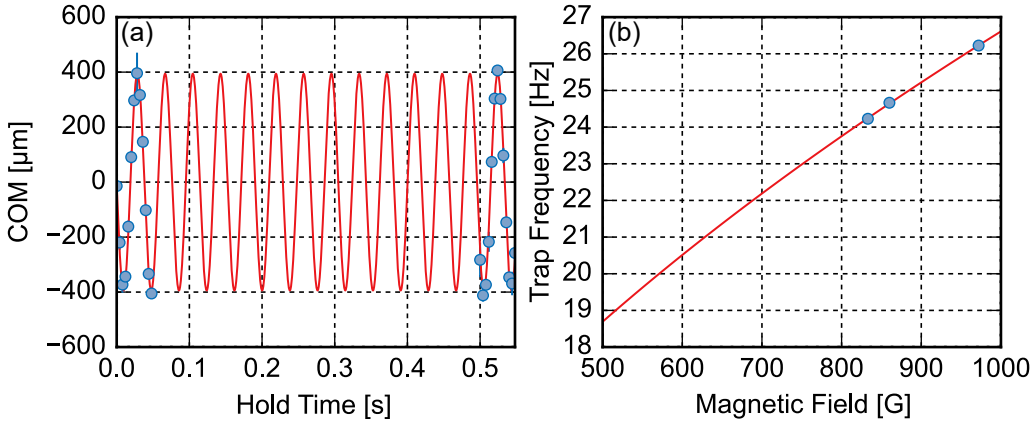

Figure 3.11: Panel (a) shows the measured centre of mass oscillation for a magnetic field of 972 G. By repeating this measurement at a number of fields the field dependence on the radial trap frequency can be obtained.

obtained by shifting the centre of mass position of the trap through the application of a strong magnetic gradient provided by the MOT coils. Upon removal of the gradient field we observe the centre of mass oscillation for a range of hold times τ. Figure 3.11 shows the result of this measurement. Oscillations with a peak-to-peak amplitude of 30 μm and 800 μm are observed for the centre of mass motion in the transverse and radial direction. The measurement of the radial trap frequency is repeated at multiple magnetic fields. From a power-law fit to the resulting trap frequencies, the magnetic field dependence is given by $\omega_r = 0.84(5) \times \sqrt{B}$. Using these two trap frequencies we can readily estimate our aspect ratio Λ at any magnetic field. For a magnetic field of 972 G confined to the TEM_{01} mode trap with the trapping frequency found above we obtain a critical atom number $N_{2D} = 3.9 \times 10^4$.

3.3.4 3D to 2D transfer procedure

While the ideal TEM_{01} mode trapping potential would trap only a single two-dimensional gas, our optical potential contains a number of fringes on either side of the main node in the intensity distribution. With a large enough laser power these fringes are capable of trapping a non-negligible number of atoms.

In order to avoid this situation, it is necessary to transfer the atoms from the initial three-dimensional 100 W dipole trap to the TEM_{01} mode trap at low power. The laser power at which this can be achieved is a function of the waist size in the tight direction and proximity of the atoms to the focal point of the trap. This dependence on the waist size makes it necessary to recalibrate the loading parameters whenever changes are made to the TEM_{01} optics. The resulting atomic distribution for a single two-dimensional gas when viewed from both the top and side is demonstrated in figure 3.12.

The transfer procedure for the TEM_{01} trap begins at the end of the evaporation ramp. Immediately after the atoms are evaporatively cooled in the high-power optical dipole trap we obtain a cloud of approximately 2.5×10^5 atoms per spin state at a temperature of approximately $0.1\,T_F$. At this stage the TEM_{01} trap is ramped up linearly over a period of 200 ms to a power of approximately 190 mW at the atoms. Performing the initial loading at powers greater than this can lead to the trapping of atoms in the

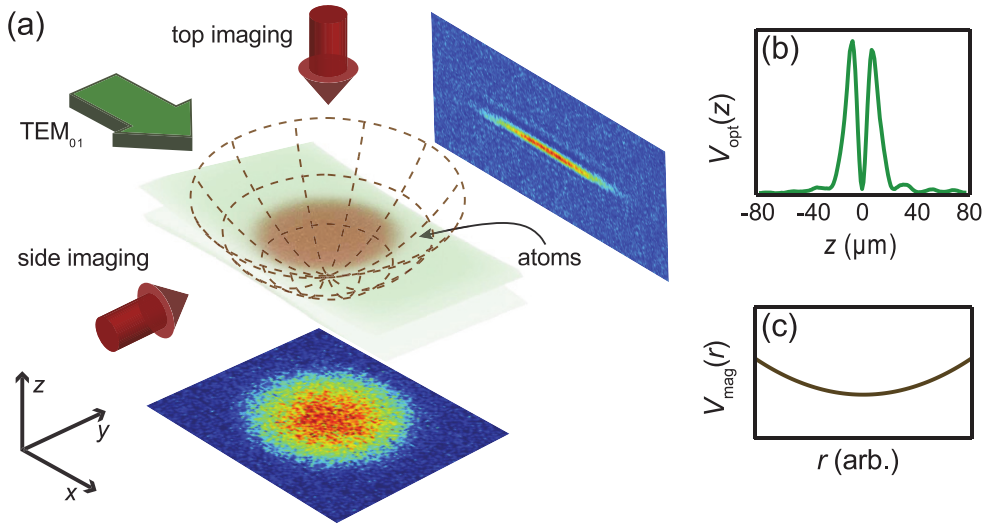

Figure 3.12: Panel (a) shows a schematic of the trapping potentials and accessible imaging degrees of freedom in the experiment, where the optical trap is shown in green and the radial confinement is represented by the brown dashed lines. Panels (b) illustrates the optical potential used to confine the transverse direction and panel (c) shows the typically harmonic trapping potential provided by the residual magnetic field curvature.

fringes of the trap. With the 2D trap held constant the 3D dipole trap is turned off linearly over a period of 200 ms. Even when the transfer from the 3D trap to the 2D trap is performed at low power, the total number of atoms transfered into the 2D trap is typically larger than the required critical atom number N_{2D}. In order to reduce the atom number we apply a magnetic field gradient to the atoms. This step is achieved by linearly increasing the magnetic gradient produced by the MOT coils to approximately $7\,\mathrm{G\,cm^{-1}}$ over 2 s. The magnetic gradient is then turned off, while simultaneously the 2D trap is increased to full power over 750 ms. This provides a highly robust method of controlling the final atom number in the two-dimensional trap. At this stage a cloud of atoms consisting of approximately 2×10^4 atoms per spin state with a temperature $0.1T_F$ is confined to the TEM_{01} mode optical trap. The timing of the final ramp is an important consideration. If the final ramp of the TEM_{01} trap is completed too quickly centre of mass oscillations can be induced in the atoms necessitating longer hold times and subsequent heating to allow for the damping of this motion.

3.3.5 Upgrades to imaging software and automation

While physical upgrades to the experiment focused on the integration of the two-dimensional trap optics a number of software upgrades have been made to streamline the experiment. In the following section, key details of the application used to automate the imaging process on the experiment are presented.

3.3.5.1 Image acquisition in LabView

Previously, image acquisition was conducted using the windows application WinView. While sufficient, it required constant user input at the start of each run of the experiment. Given that some experiments require hundreds of images for a single data set, this is an area in which automation can allow the operator to focus on more important tasks (e.g., monitoring laser locks, processing previously acquired data). In order to achieve this a new imaging program was developed in LabView[3] which interfaced directly with the Pixis CCD camera. Interfacing between LabView and the camera was provided by the LabView Software Interface ToolKit (SITK).[4] The SITK provides a LabView accessible interface to the PVCAM library.

The basic control flow of the application is shown in figure 3.13, which involves an initialisation process in which the SITK library is invoked followed by the camera setup in which all camera parameters, e.g., exposure time, kinetics window size, etc. are provided. Each acquisition requires an initial trigger, which can be provided manually but provides the same limitation as the previous WinView setup. To allow for automated acquisition a TTL pulse can be provided by the experiment control computer and read on the imaging computer via the serial port. The serial port provides a number of control bits which can be used as triggers. A pin-out and setup between the control and imaging computers can be found in Appendix A.1.2. After the image acquisition process the program continuously polls the camera storage buffer and extracts each image frame[5]as they arrive. After all frames have been collected these frames are processed according to Section 3.4. From the resulting absorption image, the pro-

[3]Compatible with 2011 and newer
[4]Obtained from Rcubed Software http://www.rcubed.com
[5]Details of the top imaging system and the definition of a frame is given in Section 3.4

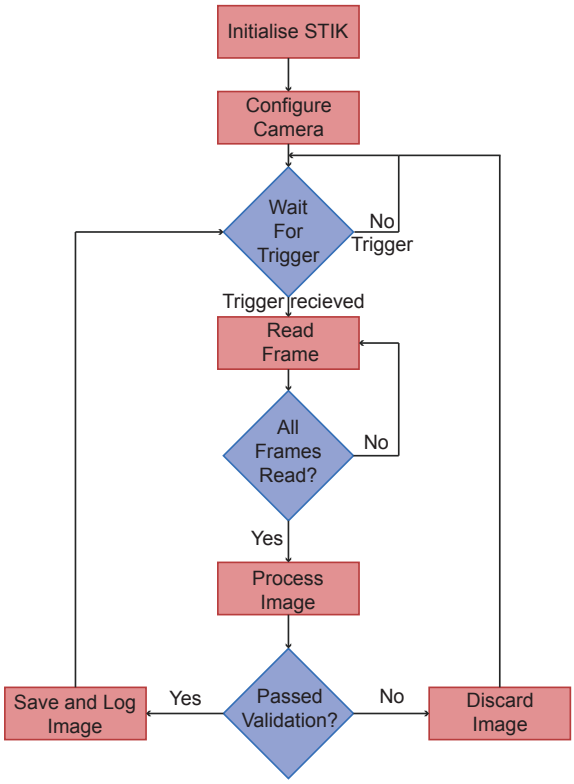

Figure 3.13: Imaging flow diagram. After initialisation of the camera the application will continuously check for new images. After images for an experimental run are obtained they are processed. If image validation has been turned on the images will be checked against the validation criteria and if found to pass will be saved and logged, otherwise the image will be discarded.

gram determines parameters such as width, center of mass and total atom number. From these parameters the experimental run can be validated according to previously defined criteria. In its current version only two validation requirements have been implemented; the first is an atom number validation which checks to see if the atomic cloud has an atom number which falls within a predefined upper and lower bound. Use of this criterion ensures greater consistency in the final data to be analysed, significantly reducing the effect of shot-to-shot variation and preventing conditions such as out of lock lasers from being unnecessarily recorded. The second criterion is based on the measurement of laser intensities but was not used for the experiments presented in this thesis but is useful for Bragg spectroscopy experiments. This second criterion demonstrates a useful feature of the new imaging control software: its ability to read information directly from an oscilloscope. The current oscilloscope[6] used in the ex-

[6]DPO 5104 LabView Library available from http://www.tektronix.com

periment has a provided LabView library which allows the read-in of measurements from any of the four available channels. These measurements can be used to monitor shot-to-shot parameters which previously had to be monitored on the oscilloscope and entered into a log file by hand. In its current incarnation this new control software links a number of previously disconnected aspects of the experiment. It currently only works with the Pixis CCD used for the top imaging setup but inclusion of the side camera is possible for future versions. A detailed outline of the operation of key elements of this new software and a quick-start guide to its usage are given in Appendix A.1.

3.4 Imaging

One of the most important part of any experiment is to be able to probe the system under examination to uncover some new knowledge. There are multiple methods with which a gas of ultracold atoms can be probed. While any method to probe the atoms is destructive, the severity of this varies between techniques. A more gentle approach to imaging can be found in phase-contrast imaging [Tur04; Mep10]. Whereas, more destructive methods such as fluorescence imaging [Ser98] can be used. Our experiment makes use of absorption imaging. While this technique is highly destructive it is technically simple to implement and provides direct knowledge of the atoms' density distribution with good signal-to-noise ratios. Pictorially, the principal idea of absorption imaging is shown in figure 3.14, in which resonant light is absorbed by the atoms and the subsequent shadow is imaged onto a CCD. Recalling that we prepare our gas in the two lowest hyperfine states as experiments are conducted at high magnetic fields to access the Feshbach resonance, these states can be described with quantum numbers $|m_I, m_J\rangle$. The imaging probe is resonant with the following transitions

$$|GND\rangle \rightarrow |EXCITED\rangle$$
$$|\uparrow\rangle = |1,-1/2\rangle \rightarrow |1,-3/2\rangle$$
$$|\downarrow\rangle = |0,-1/2\rangle \rightarrow |0,-3/2\rangle$$

Due to the presence of strong magnetic fields the optical transitions in atoms in the lowest hyperfine states are well separated by 77 MHz due to the Zeeman splitting. This splitting is large enough to be independently resolved by the probe laser field. By using a probe consisting of σ^- polarisation, the light field can only induce transitions with $\Delta m_j = -1$. As a result the transitions can be treated as an effective two-level system [Kin06].

The atoms which we image have a spatially varying density $\rho(x, y, z)$. This presence of the atoms results in a reduction of the imaging light intensity and is related to the density ρ via the Beer-Lambert law [Rei07].

$$\frac{dI}{dz} = -\rho\sigma(I)I \tag{3.23}$$

where σ is the optical absorption cross section including saturation and is given as

$$\sigma(I) = \frac{\sigma_0}{1 + (2\Delta/\Gamma)^2 + \frac{I}{I_{sat}}} \tag{3.24}$$

and $\sigma_0 = 3\lambda^2/2\pi$ is the resonant absorption cross section, $\Gamma = 5.9\,\mathrm{MHz}$ is the transition line width, $\Delta = \omega - \omega_0$ describes the laser detuning from the resonance and $I_{sat} = 2.54\,\mathrm{W\,cm^{-2}}$ is the saturation intensity for the transition. Rearranging and integrating both sides of equation (3.23) one can derive an expression for the column density $n(x, y)$ as a function of initial probe intensity in the absence of any atoms and the final intensity after propagation through the medium

$$n(x, y) = \frac{1}{\sigma_0}\left[-\left(\left(\frac{2\Delta}{\Gamma}\right)^2 + 1\right)\ln\left(\frac{I_f}{I_i}\right) + \frac{I_i - I_f}{I_{sat}}\right] \tag{3.25}$$

here, I_i is the measured intensity distribution of the probe beam in the absence of the atoms and I_f is the final measured intensity in the presence of the atoms. As shown in figure 3.12, in the experiment we have access to two imaging directions. The first is perpendicular to the radial trapping plane and is referred to as the top imaging system. The second imaging geometry is parallel to the radial trapping plane and is defined as the side imaging system. Both of these imaging geometries provide access to important features in the two-dimensional gas.

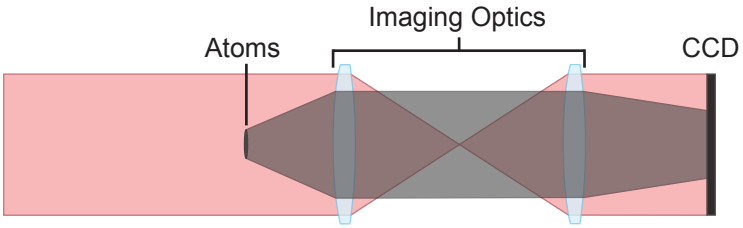

Figure 3.14: General concept of absorption imaging of an atom cloud on a CCD. Resonant laser light is absorbed by the atoms. The reduction in intensity of the probe beam due to the atoms is subsequently imaged onto a CCD camera for analysis.

Top Imaging The top imaging system consists of an optical system mounted within the supporting framework of the MOT and Feshbach coils. The exact listing of the lens elements and calibration of this system are in the following reference [Hoi14]. The imaging camera is a Pixis CCD which provides a fast kinetics mode. This allows the capture of both spin states with a minimum time delay of 820 µs, which is limited by the minimum 3.2 µs row shift time of the camera. A single image file consists of three frames. The first frame is discarded as it accumulates background light prior to imaging the atoms. The second frame contains information about the atoms and the imaging beam. To achieve this the 1024×1024 pixel CCD array is segmented into a single column made of four kinetics windows, where the window dimensions are 256×256 pixels. At any given time only one of these windows is exposed. The imaging procedure consists of three useful images and a single discarded image; this discarded image is the first window and is exposed briefly before the imaging pulses occur. The second and third windows consist of absorption images of the states $|\uparrow\rangle$ and $|\downarrow\rangle$, respectively. The final kinetics window is a reference image consisting of only the imaging beam. Referring back to equation (3.25), I_f would be taken from one of the second or third kinetics windows depending on the state to be observed and I_i is the fourth kinetics window. For the experiments described in this thesis, however, it was not necessary to image both atomic states. As such usually only combinations of windows two and four were used in the analysis.

Side Imaging The side imaging setup is simpler than that of the top imaging, both in its optical path and imaging capabilities. The imaging light exits the fibre coupler and is collimated with a $f = 75$ mm lens. The beam then passes through a $\lambda/2$

waveplate setting the correct polarisation. The beam is reflected and the atoms are imaged through the imaging system consisting of a $f = 100\,\text{mm}$ lens followed by a $f = 200\,\text{mm}$ lens onto the CCD plane of an Allied Vision Proscilica GC1290 camera. The magnification of this system is $M = 1.9$ due to slight misalignment in the placement of the lenses relative to each other. Attached to the camera is a lens tube containing an optical filter to eliminate stray light from the optical traps which enters the imaging path. Unlike the top imaging setup, the Proscilica CCD is not as feature-rich as the Pixis. During side imaging there is no access to a kinetics mode of operation. This means that only one atomic state can be imaged per experimental run. As mentioned previously, this fact does not impact on the measurements detailed in the following chapters. In order to extract the atomic density a reference beam image is still required and is taken after the camera readout of the atom image. This imaging system is heavily used in the alignment of the 2D trap and in the experiments discussed in Chapter 4, as it allows us to directly measure the dynamics of the atoms in the transverse direction.

3.4.1 2D atom number calibration

As described previously, we make use of resonant light to perform our absorption imaging and while we are operating in a regime of low optical densities $OD_{peak} \lesssim 0.1$ we use an image pulse of duration $10\,\mu\text{s}$ with an intensity $I \approx 0.25 I_{sat}$. While this increased exposure time greatly enhances the signal-to-noise ratio for a single image it also presents difficulties in obtaining a true measurement of the density distribution. These difficulties come about through a number of physical sources. A main source of measurement error is due to Doppler shift of the atoms away from the resonant frequency of the imaging beam during the imaging pulse. This reduces the number of scattering events through the cloud, resulting in the underestimation of the optical density and hence an underestimate of the total atom number. Due to the low mass of ^{6}Li compared to other atoms such as ^{87}Rb which are also commonly imaged through absorption, the overall acceleration of lithium atoms is much greater meaning lower intensities and pulse lengths should be used. In addition to the Doppler shift, in an atomic gas with finite thickness the measured absorption cross-section can be altered

by multiple scattering of a single photon in the medium [Cho12].

True representations of the density distribution are better obtained in the high intensity limit [Rei07]. By saturating the transition with imaging light with an intensity $I \gg I_{sat}$ the transition becomes power-broadened and with a short exposure time the overall Doppler shift will be smaller than the broadening of the transition resulting in a more accurate representation of the absolute atomic density. This imaging configuration suffers from lower signal-to-noise compared to long exposure imaging.

In order to make use of the higher signal-to-noise obtained in the long exposure imaging we must determine a correction for these measurements. To do this we conduct experiments in both the high-intensity and low-intensity imaging regimes. For example, experiments conducted in Chapter 5 involve 200 low-intensity images and 50 high-intensity images which are used to determine a density correction factor. We calculate the correction factor in the following way. This process begins with determining the centre of mass for each individual image and then re-centering each image such that they are overlapped, this procedure is needed to account for any drifts in camera position over the duration of the measurement which are typically ~ 1 pixel. The average of the overlapped 2D optical densities in the high and low-intensity images is taken, which are denoted OD_{High} and OD_{Low} and shown in figure 3.15. We then take the ratio of these two images to create a correction factor $C_{OD} = OD_{High}/OD_{Low}$

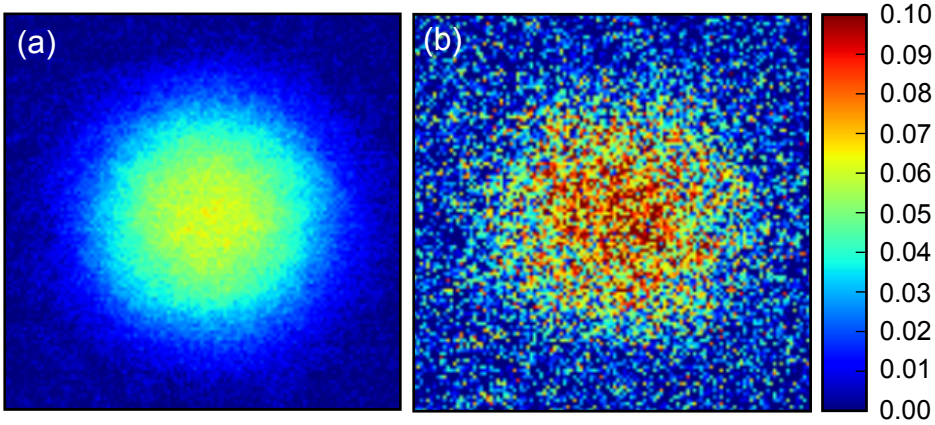

Figure 3.15: Averaged images for low intensity (a) and high intensity (b). Comparing these two images it is clear that the peak optical density is slightly higher in the high intensity case. However, the increased noise is significant compared to imaging with low intensity and longer exposure time.

for every pixel and compare the optical density at each pixel of C_{OD} to the optical density at the same pixel in OD_{Low}. These values are then binned in terms of OD_{Low}. After this binning procedure we obtain a plot of C_{OD} vs. OD_{Low} as shown in figure 3.16. We find for optical densities ≤ 0.015 there is a significant amount of noise, arising from the high level of noise in the wings of the cloud in the images taken at high intensity. For optical densities greater than this we find an approximately constant correction factor and thus we determine the overall correction C_{OD} as the mean and standard deviation of all the bins where $OD_{Low} \geq 0.015$. This correction is applied to all images measured with a long imaging pulse to more accurately determine the atomic density. In general this correction would not be constant, but is approximately constant here due to the low optical densities of the gas.

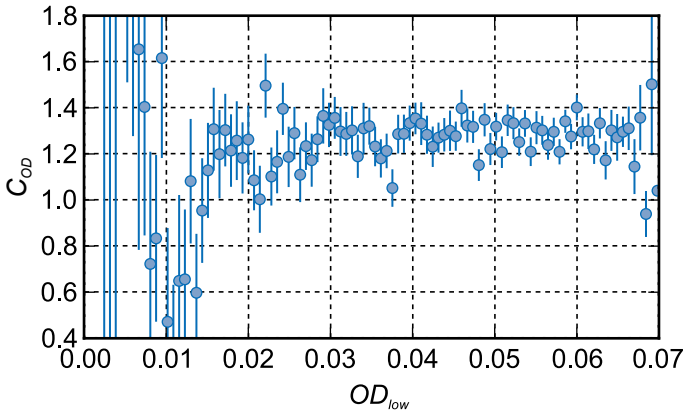

Figure 3.16: Optical density correction C_{OD} for a given experimental run. At low optical densities ($OD_{low} < 0.015$) the correction becomes unreliable.

3.5 Summary

In this chapter the basic theory of the role light fields play in providing confinement and cooling of neutral atoms was introduced. With this the steps used to optically produce a degenerate Fermi gas in three dimensions was outlined, stepping through the stages of the Zeeman slower, magneto-optical trap and finally evaporative cooling in a dipole trap. Following this, details of our TEM_{01} trap were introduced and the procedure to crossover from a three-dimensional to two-dimensional Fermi gas given. Finally, the method of imaging the atoms was presented, including overviews of the

two imaging geometries accessible to the experiment and how we are able to utilise different imaging parameters to better obtain a measurement of the density distribution of the Fermi gas. The developments presented in this chapter allow us to begin experiments on degenerate two-dimensional Fermi gases. In these experiments we aim to measure the parameter space in which two-dimensional kinematics in an interacting Fermi gas is valid and, using this, to prepare a kinematically two-dimensional Fermi gas and determine its thermodynamic properties.

Chapter 4

Criteria for two-dimensionality in an interacting Fermi gas

4.1 Introduction

In order for a Fermi gas to be truly two-dimensional, any dynamics in the transverse direction need to be removed from the system. For the case of an ideal Fermi gas, this is achieved by limiting the total number of particles and energy scales of the system such that excited transverse states are energetically unavailable as discussed in Section 2.2.2. For realistic conditions when interactions are present in the gas, calculations have indicated that interactions can lead to transverse excitations [Kes06]. For experimental realisations of a two-dimensional Fermi gas, being able to determine the regions of two-dimensionality is an important task to ensure future experiments can be directly compared to two-dimensional theories. The question to be examined in this chapter is how exactly does the introduction of interactions limit the two-dimensional or quasi-two-dimensional nature of a degenerate Fermi gas.

As discussed in Section 2.3.3, in two dimensions there always exists a bound state for any arbitrarily weak attractive interaction. On the far BCS side of the Feshbach resonance the atoms can become weakly bound, forming a gas of Cooper pairs anti-correlated in momentum-space. The separation between these bound atoms may be much greater than the average interparticle spacing and greater than the transverse harmonic oscillator length $l_z = \sqrt{\frac{\hbar}{m\omega_z}}$. In this limit the pairs are well described by

a two-dimensional picture. As one approaches the BEC limit, particles form tightly bound dimers which can have a characteristic length scale smaller than that of l_z. In this case the molecules are essentially three-dimensional [Pet01]. While a direct measurement of the excited state fraction of atoms is not easily obtained, measurement of the transverse release energy through the measurement of the width of an expanded gas is possible [Men02; Bou03; Bou04]. Measurement of this energy can provide information regarding the presence of transverse excitations in the gas.

In the following sections a method for the determination of the transverse width from absorption images of an expanded cloud will be presented followed by the observation of how the transverse width evolves through the BCS-BEC crossover. Finally, the critical atom number, which indicates the transition from three to two dimensions will be determined with varied interaction strengths. Using these results, it is possible to construct a crossover diagram which maps the densities and interaction strengths that allow the production of a kinematically two-dimensional Fermi gas. The results contained in this chapter have been published in [Dyk16a].

4.2 Evolution of the transverse excitation through the BCS-BEC crossover

The geometry of this experiment can been seen in figure 3.12. We begin by preparing a two-dimensional gas in a highly oblate harmonic trapping potential as described in Section 3.3. After loading the trap the magnetic field generated by the Feshbach coils is ramped linearly to its final value for the measurement over a period of 250 ms. Following the ramp of the Feshbach field, the gas is held for an additional 50 ms to allow equilibration. The transverse confinement is then suddenly removed allowing the atoms to freely expand in the transverse direction for 600 μs in the presence of the radial confining potential. Following the time of flight (TOF) expansion the atoms are imaged perpendicular to the transverse trapping direction. The duration of expansion τ is chosen such that $\tau \ll \omega_r^{-1}$ to avoid changes in the density distribution in the radial direction but $\tau \gg \omega_z^{-1}$ to reach the asymptotic limit of the expansion in the transverse direction. By measuring the transverse cloud width $\langle z^2 \rangle^{1/2}$ it is possible to obtain a

measure of the original transverse energy in the trapped gas.

The measurement of the transverse width is repeated across the Feshbach resonance between 700 G and 972 G for a gas with atom numbers $N = 24 \times 10^3$ and $N = 12 \times 10^3$. In terms of the ideal critical atom number N_{2D}^{Ideal} these gases are $0.6N_{2D}^{Ideal}$ and $0.3N_{2D}^{Ideal}$.

The method of processing the obtained absorption images is described in Section 3.4. At each magnetic field five images are taken. An example of these images can be seen in figure 4.1. From the obtained two-dimensional optical density profiles we determine the integrated line profile of the density distribution in the transverse direction by integration over the radial direction as

$$n_{1D}(z) = \int n(x,z)\mathrm{d}x\,. \tag{4.1}$$

The width of the expanded cloud is determined by fitting a Gaussian function to the measured line profile. At each value of the magnetic field that is imaged, the width is obtained for each of the five images and the mean and standard deviation are determined.

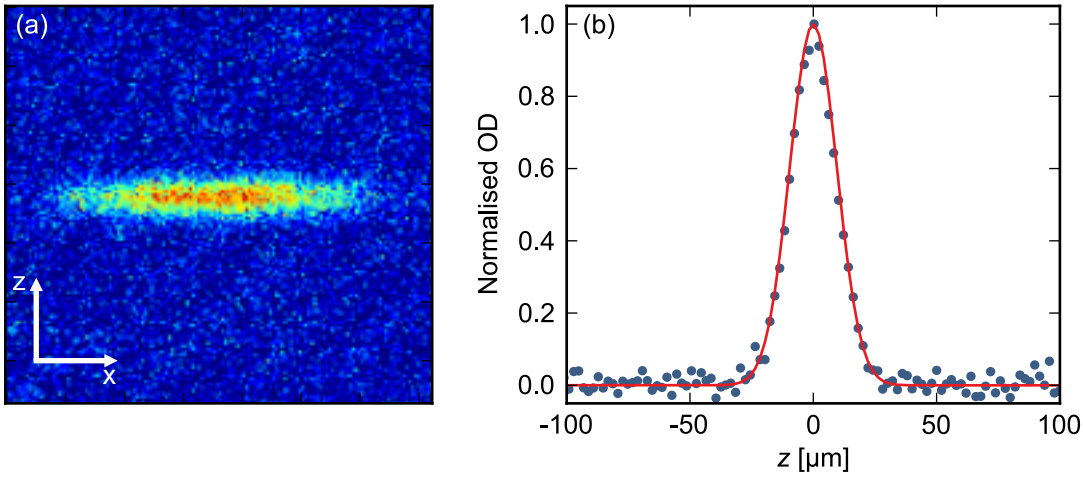

Figure 4.1: Panel (a) shows the measured two-dimensional density distribution for an expanded ($\tau = 600\,\mu$s) weakly interacting Fermi gas taken at 972 G. In panel (b) the resulting one-dimensional line profile for the transverse direction is given. The solid red curve is a Gaussian fit for this profile.

In figure 4.2 the measured widths are plotted for both the large and small atom numbers. A number of interesting features can be seen in this measurement.

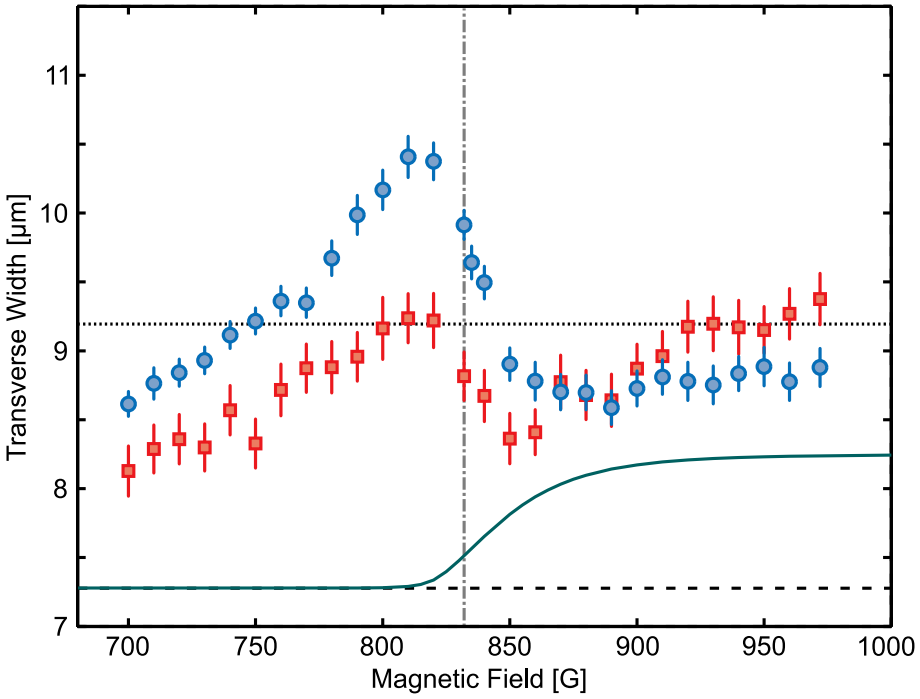

Figure 4.2: Transverse cloud width after 600 μs expansion. Blue circles correspond to $N = 0.6N_{2D}^{Ideal}$ and the red squares to $N = 0.3N_{2D}^{Ideal}$. The dotted line represents the width of an ideal Fermi gas after expansion, including finite imaging resolution and magnification. The grey dash-dot line signifies the position of the Feshbach resonance. Two-body calculations for the transverse width (green solid line) is also shown.

Beginning with the blue data points with total atom number $N = 24 \times 10^3$, on the far BCS side of the Feshbach resonance where $E_B \ll E_F$, the width remains approximately constant down to a field strength of approximately 870 G. The constant width is due to the fact that after the removal of the confining potential we image atoms which below the critical value of N_{2D} have a momentum distribution set primarily by the ground state energy of the transverse harmonic oscillator. At large magnetic fields as the gas is in the weakly attractive regime a comparison with the expanded non-interacting gas can be made. For an ideal gas the ground state wavefunction in the transverse direction is a Gaussian.[1] After removing the confining potential the root-mean-square (rms) width of the expanding Gaussian wave-packet can be calculated as

$$\sigma_z = \sqrt{\frac{\hbar}{2m}\left(\frac{1}{\omega_z} + \omega_z t^2\right)} \tag{4.2}$$

[1]The full wavefunction is $\Psi(z) = \left(\frac{m\omega_z}{\pi\hbar}\right)^{1/4} e^{(-m\omega_z z^2/2\hbar)}$

where $\frac{\omega_z}{2\pi} = 5.15\,\text{kHz}$ is the transverse trap frequency and $t = 600\,\mu\text{s}$ is the expansion time. The resulting width is $7.85\,\mu\text{m}$. Taking into account the finite rms resolution of the imaging system, which is $4.7\,\mu\text{m}$, the final result is a width of $9.2\,\mu\text{m}$. Due to the weak attractive interactions present during expansion, the measured width appears to shift slightly below the ideal gas limit. As the magnetic field is reduced a decrease in the overall width is observed as the attractive interactions in the gas become stronger. However, for fields between 850 G and the pole of the Feshbach resonance at 832.2 G a steady increase in the width is observed. This increase signifies a departure from purely two-dimensional kinematics, as one would expect a continued reduction in the transverse width due to the increased strength of the attractive interactions at these magnetic fields.

On the BEC side of the resonance, as the magnetic field remains on during expansion, weakly bound pairs formed *in situ* may remain bound after release. However, as the energy of the ground state of the trapped gas is significantly larger than the pair binding energy with $E_{B,3D}/(\hbar\omega_z) = 0.1$ at 820 G it is likely that any pairs will dissociate upon release leading to the observed increase in the transverse width between 832 G and 820 G.

The transverse width reaches a maximum on the BEC side of the Feshbach resonance at approximately 810 G. Beyond this a gradual decrease in the transverse width can be seen. This decrease is due to the fact that for fields below $\sim 800\,\text{G}$ any pairs which have formed have a binding energy $E_{B,3D} \gtrsim \hbar\omega_z$ and may not break after the removal of the transverse confining potential, leaving a gas of expanding molecules which due to their larger mass expand more slowly than a purely atomic gas.

Probing deeper into the BEC regime where $E_{B,3D} \gg \hbar\omega_z$ the transverse width decreases towards the result for a weakly interacting Bose gas. In this limit the fermionic degrees of freedom are no longer important and the two-dimensional criterion based on Pauli exclusion is no longer relevant as the gas is predominately made of tightly bound molecules. Here, the binding energy becomes the characteristic energy scale of the system and upon release the pairs may remain bound and the expansion is that of a repulsive Bose gas. As the gas enters deeper into the BEC regime the repulsive interactions between the pairs decreases and in the limit that the repulsive interaction

becomes negligible the expected transverse width should remain constant regardless of N as the gas is dominated by the bosonic degrees of freedom and all of the bound pairs may condense to the ground state where the transverse width takes the limiting value $\left\langle z^2 \right\rangle^{1/2} = 7.3\,\mu\text{m}$. Experimentally, this limit is not readily achievable as the lifetime of such a gas would be too short due to three-body losses.

The red squares in figure 4.2 show the same experiment completed for a lower atom number $N = 12 \times 10^3$. In this case an approximately constant width is again observed in the far BCS regime, with a decrease in total width as the attractive interactions become stronger. A noticeable increase in the width begins to appear at a field of 850 G peaking at 810 G as was seen for the gas with $N = 24 \times 10^3$ indicating that the position of this peak depends only on the ratio $E_B/\hbar\omega_z$. We can speculate from the fact that the position of the resonance depends only on this ratio that the peak may be due to a confinement induced resonance (CIR) [Ols98] leading to a coupling between atoms and higher excited transverse bound states. In a one-dimensional harmonically trapped Fermi gas such a resonance occurs when the s-wave scattering length a_{3D} approaches the transverse harmonic oscillator length l_z. These resonances are not present in two dimensions in a purely harmonic potential; however for positive scattering lengths anharmonicity in the confining potential permit a similar resonance [Pen11] and the position at which the resonance occurs is given by $C_{2D}a_{3D} = l_z$, where $C_{2D} = 1.19(3)$ [Hal10]. For the trapping frequencies at which these experiments were conducted the transverse harmonic oscillator length is $l_z = 571.25\,\text{nm}$. For this value we would expect a CIR at approximately 793 G which is below where we observe our maximum.

This shift in the resonance position may arise from the unclear role of pair breaking after the removal of the confining potential. This may result in an enhancement in the observed width around 810 G to 832 G. A second issue to consider is the finite Fermi energy of the gas which provides a range of collision energies which may be degenerate with the excited transverse bound state at different magnetic fields. Such an effect could explain the differences seen between the large and small density results, where the lower density cloud still displays a smaller peak. These combined effects may mask the true position of the CIR.

As previously stated, in the asymptotic limit of the expansion the width is determined by the total energy available to the system. This energy comprises both the kinetic energy and interaction energy. While the many-body solution of the expansion of an interacting Fermi gas is an open problem, there are solutions in the two-body limit which can be explored and compared to the experimental results.

The problem of the expansion of two-interacting particles initially confined to a highly oblate trap and released in the presence of a radially confining potential was completed by our collaborator Shiguo Peng [Dyk16a; Dyk16b]. While the full derivation is beyond the scope of this chapter the key results will be given. The problem is simplified due to the presence of harmonic confinement allowing the centre of mass and relative motion to be analysed independently. Beginning with the centre of mass motion the problem can be treated as a one-dimensional harmonic oscillator in which the ground state wave function is given as [Dyk16b]

$$\Psi_{cm}(Z,t) = \left(\frac{4\eta}{\pi d^2}\right)^{1/4} \frac{e^{-[2\eta Z^2/d^2](1+i\eta\omega_r t)}}{\sqrt{1+i\eta\omega_r t}}. \tag{4.3}$$

The transverse width can be determined as

$$\left\langle Z^2 \right\rangle = \int_{-\infty}^{\infty} \Psi^*_{cm}(Z,t) Z^2 \Psi_{cm}(Z,t) = \frac{d^2}{8\eta}(1+\eta^2\omega_r^2 t) \tag{4.4}$$

where $d = \sqrt{\frac{2\hbar}{m\omega_r}}$ is the harmonic oscillator length, $\eta = \frac{\omega_z}{\omega_r}$, ω_r is the radial trapping frequency and t is the expansion time.

Calculation of the relative motion of the particles is more complex, requiring first the solution of the energy and wavefunction in the initial trap. In the presence of both radial and transverse confinement the Hamiltonian describing the relative motion is

$$\hat{H}_{rel} = -\frac{\hbar^2}{m}\nabla^2 + \frac{1}{4}m\omega_r^2(r^2+\eta^2 z^2) + \hat{V}_{int}(\mathbf{r}) \tag{4.5}$$

where the calculation of the binding energy and relative wavefunction can be determined as in Idziaszek and Calarco [Idz06]. Upon release, the motion of the atoms is

described by the modified Hamiltonian

$$\hat{H} = -\frac{\hbar^2}{m}\nabla^2 + \frac{1}{4}m\omega_r^2 r^2 + \hat{V}_{int}(\mathbf{r}). \tag{4.6}$$

This Hamiltonian can be solved as in [Yur10] leading to the two-body wavefunction $\Psi_\varepsilon(\mathbf{r})$ given as [Dyk16b]

$$\Psi_\varepsilon = \frac{C_\varepsilon}{\sqrt{d}}\sum_{n=0}^{\infty}\chi_n(\rho)\frac{\cos\left[\frac{2L}{d}\sqrt{\varepsilon/2-n}\left(\frac{z}{L}-1\right)\right]}{\sqrt{\varepsilon/2-n}\sin\left(\frac{2L}{d}\sqrt{\varepsilon/2-n}\right)} \tag{4.7}$$

where L is the total length of system in the z direction and C_ε is a normalisation factor. The resulting transverse width after expansion is then

$$\left\langle z^2\right\rangle = \sum_{\varepsilon,\varepsilon'} A^*(\varepsilon')A(\varepsilon)\left\langle\Psi_{\varepsilon'}\right|z^2\left|\Psi_\varepsilon\right\rangle e^{i(\varepsilon-\varepsilon')\omega_r t} \tag{4.8}$$

where

$$\left\langle\Psi_{\varepsilon'}\right|z^2\left|\Psi_\varepsilon\right\rangle = \int \Psi^*_{\varepsilon'}(\mathbf{r})z^2\Psi_\varepsilon(\mathbf{r})d^3\mathbf{r} \tag{4.9}$$

$$A(\varepsilon) = \int \Psi^*_\varepsilon(\mathbf{r})\Psi_i(\mathbf{r})d^3\mathbf{r} \tag{4.10}$$

and Ψ_i is the initial wavefunction prior to release. Finally, the total transverse width can be determined from equations (4.4) and (4.8) as [Dyk16b]

$$\sqrt{\left\langle z^2_{com}\right\rangle + \left\langle z^2_{rel}\right\rangle} = \sqrt{2\left\langle Z^2\right\rangle + \frac{1}{2}\left\langle z^2\right\rangle}. \tag{4.11}$$

The result of this calculation is shown as the solid green line in figure 4.2. As the gas transitions from the weakly interacting BCS limit at large magnetic fields the transverse width decreases monotonically through the crossover as the attractive interactions become stronger, reaching a minimum width corresponding to an ideal gas of molecules on the BEC side of the Feshbach resonance. Returning to the weakly BCS regime, the two-body result is appreciably smaller than that of the ideal gas. This is due to the persistence of bound pairs in the zero temperature limit considered in the calculation. As the real temperature in the experiment is much larger than the binding energy of these weakly bound pairs, after the removal of the transverse confinement

the pairs are likely to dissociate leading to a width closer to the ideal gas calculation.

Comparing the experimental results to the two-body calculation, we find that the shapes agree qualitatively in the BCS limit. As the interaction strength increases, we begin to observe a significant departure from the expected two-body behaviour experimentally. We attribute the observed increase of the transverse width to the presence of transverse excitations in the gas. While the existence of these excitations is clear, we cannot easily determine if they are atomic or molecular excitations. Further experimental and theoretical studies in the strongly interacting region are required to better determine the nature of these excitations. Collisions during expansion may also lead to an increase in the transverse width. But as will be discussed in the following section, collisions alone fail to account for total enhancement observed.

We can also compare the two-dimensional result to that of a three-dimensional gas. Here, we find that in two dimensions the effect of interactions in the gas add a degree of extra complexity. Figure 4.3 from Bourdel *et al.* [Bou04] shows a clear monotonic dependence on the interactions in three dimensions, similar to the two-body limit of the two-dimensional gas.

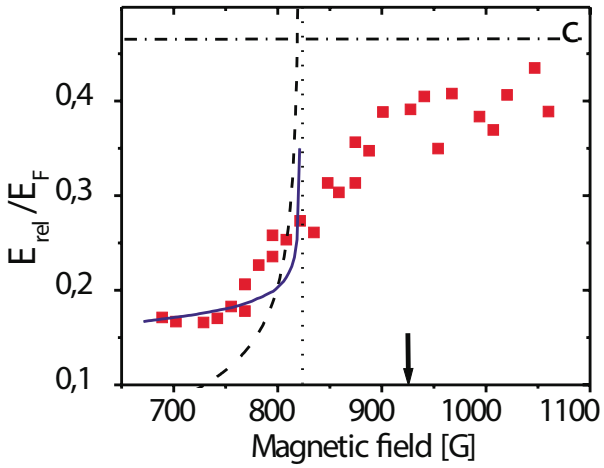

Figure 4.3: Release energy for a 3D Fermi gas measured across the Feshbach resonance. The release energy here displays a monotonic decrease from the BCS to the BEC regime. Reprinted figures with permission from T. Bourdel *et al.* "Experimental study of the BCS-BEC crossover region in lithium 6", *Physical Review Letters* **93** (5), 050401 (2004).

4.2.1 Influence of collisions during expansion

As the magnetic field remains on during expansion, a possible explanation for the observed results could be due to elastic collisions during the expansion which can transfer energy from the radial to the transverse direction. This process obfuscates the connection between the measured transverse width and the *in situ* transverse energy. As the effect of these collisions is maximised at the Feshbach resonance where the scattering cross section reaches the unitary limit $\sigma_{el} = 4\pi/k^2$, the magnitude of the possible enhancement of the transverse width due to collisions during expansion can be determined and represents the worst-case scenario which can occur due to collisional processes.

Beginning with the assumption that all particles in the gas are in the transverse ground state, the change in energy in the transverse direction will be proportional to the integrated product of the elastic scattering rate Γ_{el} and the mean energy in the radial direction $\bar{E}_r$

$$\Delta E \propto \int_0^\tau \Gamma_{el}(t)\bar{E}_r \mathrm{d}t \tag{4.12}$$

where τ is the total expansion time. After the transverse confinement has been removed the particles can scatter into a continuum of states in the transverse direction and as Pauli blocking is no longer significant the classical scattering rate $\Gamma_{el} = \langle n(t)\rangle \sigma_{el}\bar{\mathrm{v}}$ can be used. Here $\bar{\mathrm{v}} \propto \sqrt{E_F}$ is the mean velocity of the atoms, and $\langle n(t)\rangle$ is the mean density of the gas which can be experimentally determined by integrating the measured density distribution

$$\langle n(t)\rangle = \frac{1}{N}\int_{-\infty}^{\infty} n(\mathbf{r},t)^2 d^3\mathbf{r}\,. \tag{4.13}$$

As the expansion time τ is significantly smaller than ω_r^{-1} the density profile of the atoms in the radial direction does not change over the expansion time, which allow two assumptions to be made. Firstly, $\bar{E}_r$ should remain approximately constant as it is set by the Fermi energy and depends on the radial density. Secondly, any time-dependence in $\langle n(t)\rangle$ originates from dynamics of the gas in the transverse direction. The latter

assumption implies that $\langle n(t)\rangle$ can be described by an initial density distribution $\langle n(0)\rangle$ scaled by a time dependent function $f_z(t)$ which describes the transverse expansion and is independent of the total atom number N.

By isolating the density dependencies for Γ_{el}, σ_{el} and E_r it is possible to establish for the worst-case scenario experienced at the Feshbach resonance the maximum energy which can be transfered to transverse expansion to be

$$\Delta E \propto \langle n(0)\rangle^{3/2} . \tag{4.14}$$

Experimentally, $\langle n(0)\rangle$ can be measured at the Feshbach resonance by integrating the acquired absorption images according to equation (4.13). We find that the density scales as $\langle n(0)\rangle \propto N^{0.59(8)}$, slightly larger than the zero-temperature ideal gas result $\langle n(0)\rangle \propto N^{1/2}$ due to the presence of interactions. The maximum energy exchange which may arise in the measurement is then $\Delta E \propto N^{0.9}$. Using this result it is possible to estimate the atom number dependence on the transverse width which scales as $\sqrt{E}$, resulting in a maximum value of $\left\langle z^2\right\rangle^{1/2} \propto N^{0.45(6)}$. By measuring the transverse width at the Feshbach resonance and varying the atom number the scaling of the transverse width with N can be measured directly and is shown in figure 4.4. Apply-

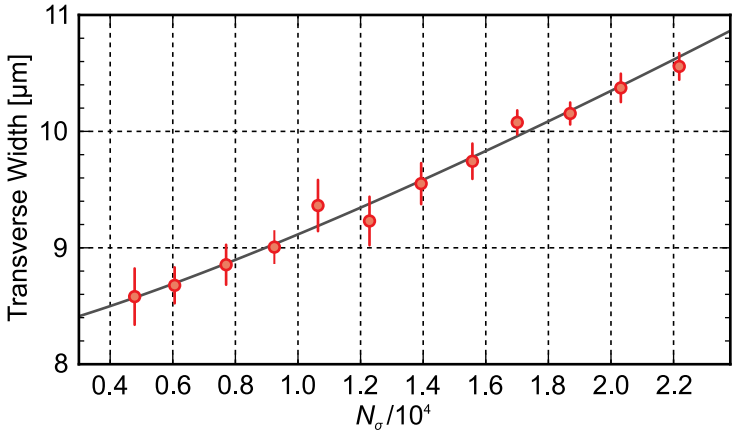

Figure 4.4: Measured transverse width at the Feshbach resonance for total atom numbers below N_{2D}^{Ideal}.

ing a power-law fit with a free exponent to the measured data, the transverse width is found to scale as $N^{1.24(15)}$. This result is significantly larger than what would be possible due to collisions during the expansion time, indicating that the additional energy

which results in the observed enhancement of the transverse width must be a result of transverse excitations that were present in the gas prior to release.

4.3 Determining the 2D kinematics of an attractive Fermi gas

The measured enhancement of the transverse width for a Fermi gas with an atom number below the critical atom number N_{2D}^{Ideal} for an ideal gas demonstrates that when working with two-dimensional Fermi gases, ensuring two-dimensionality requires not only consideration of how the thermal energy and Fermi energy compare to $\hbar\omega_z$ but also that control of the density and strength of interactions is critical. For future experiments a more careful measurement of the critical atom number beyond the weakly interacting gas should be established.

Previously, it was shown that it is possible to experimentally determine the value of N_{2D} through a measurement of the transverse width of the gas as a function of total atom number [Dyk11]. At low atom numbers ($N < N_{2D}$) a constant transverse width is observed independent of N. This constant width is due to the fact that only the transverse ground state is occupied, resulting in a fixed energy available for the transverse expansion of the gas. As N is increased above N_{2D} excited transverse states become occupied, providing additional energy for the transverse expansion resulting in the observation of an increased transverse width as N increases. For an interacting gas N_{2D} is the atom number which corresponds to the transition from a constant transverse width to a transverse width which increases with total atom number.

In order to measure N_{2D} throughout the crossover we begin by preparing the gas as previously described in Section 3.3.4 until the magnetic gradient evaporation stage. By altering the strength of the magnetic gradient we can control the number of atoms removed from the TEM_{01} mode trap at lower power. This method provides precise control over the final atom number of the gas. We begin with a weak gradient resulting in an atom number $N > 5 \times 10^4$. After the gradient field is removed the Feshbach field is ramped to its final value over 250 ms, followed by an equilibration time of 250 ms after which the gas is released for an expansion time of 600 µs and then imaged.

This process is repeated, where the magnetic field gradient is increased during the evaporation stage to reduce the atom number further for the next set of images. At the largest magnetic evaporation we image a Fermi gas with $N \approx 500$.

From the images obtained at each value of the evaporation set-point the transverse width is extracted through Gaussian fits as described in Section 4.2. This measurement is repeated through the BCS side at 972 G to 820 G just below the pole of the Feshbach resonance.

4.3.1 Atom number calibration

Due to the larger optical densities and the large spatial extent of the gas when imaging from the side, it was determined that accurate measurement of N from side imaging alone may not be possible. To remedy this we make use of the fact that the application of the gradient field results in highly repeatable atom numbers and we can also image the cloud from the top, parallel to the tight confinement direction. To determine the correction we obtain a series of measurements using the top imaging with a determined correction factor for the absolute density as described in Section 3.4.1. The same measurement is repeated using side imaging. For each value of the applied magnetic gradient we determine the atom number by integrating over both spatial directions and by taking the ratio of these we obtain a correction factor which we can apply to future side images. We observe a roughly constant correction factor at mod-

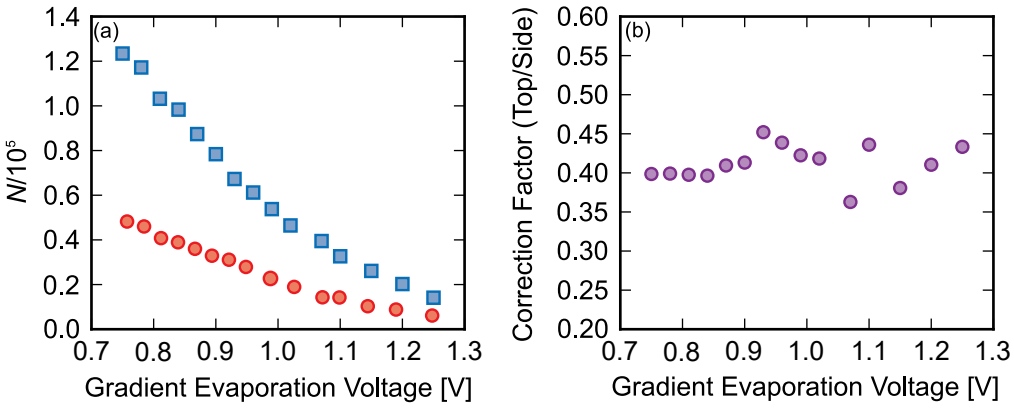

Figure 4.5: Panel (a) shows the calculated atom numbers for top imaging (red circles) and side imaging (blue squares). Panel (b) shows the correction factor as a function of evaporation strength. The correction is approximately constant.

erate atom numbers. At lower atom numbers where background noise can begin to make measurement of atom numbers difficult we find some additional fluctuation in the observed correction. The final determined correction factor is taken as the mean value of the values shown in panel (b) of figure 4.5 and is 0.41(2).

4.3.2 Determination of N_{2D} in the presence of interactions

The results of the experiment described previously in Section 4.3 are shown in figure 4.6 for each magnetic field, ranging from the BEC side of the Feshbach resonance at 820 G into the weakly interacting BCS regime at 972 G. In order to determine these points we measure the width from Gaussian fits to the one-dimensional line profiles as described in Section 4.2. Despite taking multiple images at fixed strengths of the magnetic gradient, shot-to-shot fluctuations in the atom number lead to a spread in our observed N. This effect is particularly important in the low atom number images. In addition to this, the low atom number images suffer from poor signal-to-noise, particularly when imaging $N < 2 \times 10^3$. This leads to greater fluctuation in the measured widths. To compensate for this a larger number of shots are taken at low atom numbers. The raw widths are binned according to the measured total atom number which gives the points in figure 4.6, where the red circles are the mean value for the bin and the error bars are the standard deviation of the widths in the bin. We can explore the effect interactions have on N_{2D} by looking at how the observed value varies across the BCS-BEC crossover. Beginning on the far BCS side with a weakly attractive gas at 972 G the gas has a binding energy $E_B = 0.0008\hbar\omega_z$ calculated from equation (2.46); here the measured transverse width displays an elbow at $N \approx 40 \times 10^3$ in agreement with the estimated value of N_{2D}^{Ideal} given in Section 3.3.3.2. Decreasing the magnetic field to 950 G we again find a critical atom number in agreement with ideal gas result. At 920 G the critical atom number is observed to have shifted to slightly lower values of N. Increasing the strength of the attractive interactions further, at 865 G the gas has a binding energy $E_B = 0.043\hbar\omega_z$ and the position of the elbow is shifted significantly lower to $N \approx 20 \times 10^3$. If interactions were unable to induce transverse excitations we would expect a value of $N_{2D}^{Ideal} \approx 43 \times 10^3$. The increase in N_{2D}^{Ideal} compared to the value given in Section 2.2.2 is due to the reduced radial confinement frequency at lower

magnetic fields. At the Feshbach resonance the binding energy is $E_B = 0.244\hbar\omega_z$ and

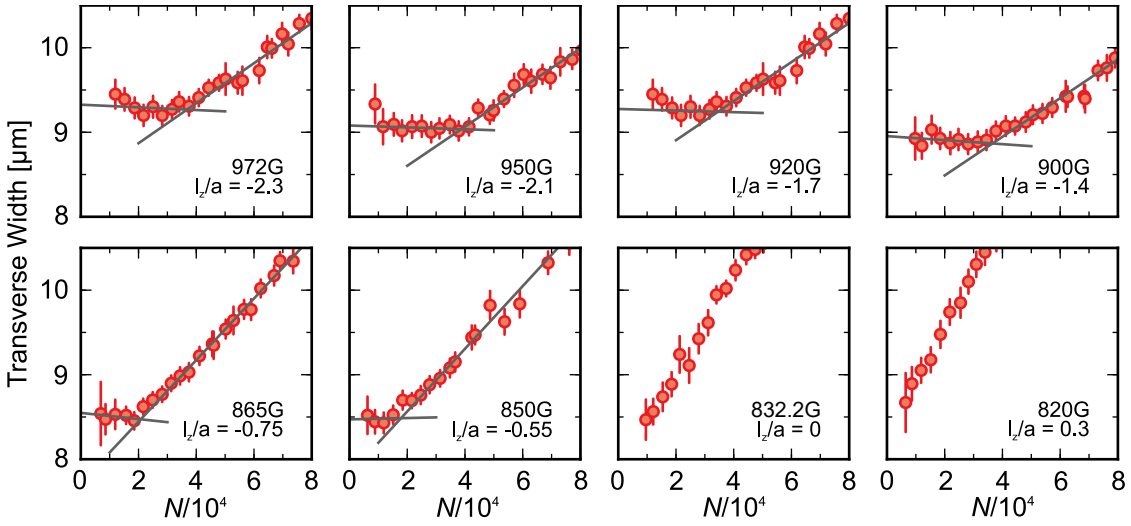

Figure 4.6: Measured transverse width as a function of atom number through the BCS-BEC crossover. Grey lines are linear fits to the measurements of plateau and increasing regions of the width where N_{2D} is determined as the intersection of these fits.

for the atom numbers experimentally accessible it is no longer possible to resolve any indication of a plateau leading to a elbow in the transverse width at this field. Moving into the BEC side of the resonance, at 820 G the plateau remains unobservable.

Using these measurements of N_{2D} an empirical crossover diagram can be constructed. The crossover diagram shown in figure 4.7 clearly shows how N_{2D}, in the figure represented as a function of the dimensionless energy $E_F/\hbar\omega_z$, with $E_F = \sqrt{N}\hbar\omega_r$, depends on the strength of interactions, given by the dimensionless variable l_z/a_{3D}, where l_z is the harmonic oscillator length in the transverse direction and a_{3D} is the 3D s-wave scattering length. The geometric limit for two-dimensionality is given by the dotted horizontal line at $E_F/(\hbar\omega_z) = 1$. This limit corresponds to the value N_{2D}^{Ideal} which is determined by equation (2.25). At interaction strengths $-l_z/a_{3D} < 1.5$, initial signs of a departure from the geometric limit due to the influence of interactions begin to manifest and the departure from the ideal limit increases with stronger interactions.

From this crossover diagram two regions can be designated. The region below the dashed white line represents the limit of densities and interactions where we can be confident that the atoms behave two-dimensionally. Within this region transverse excitations are not detected and the two-dimensional criteria is satisfied. For strongly

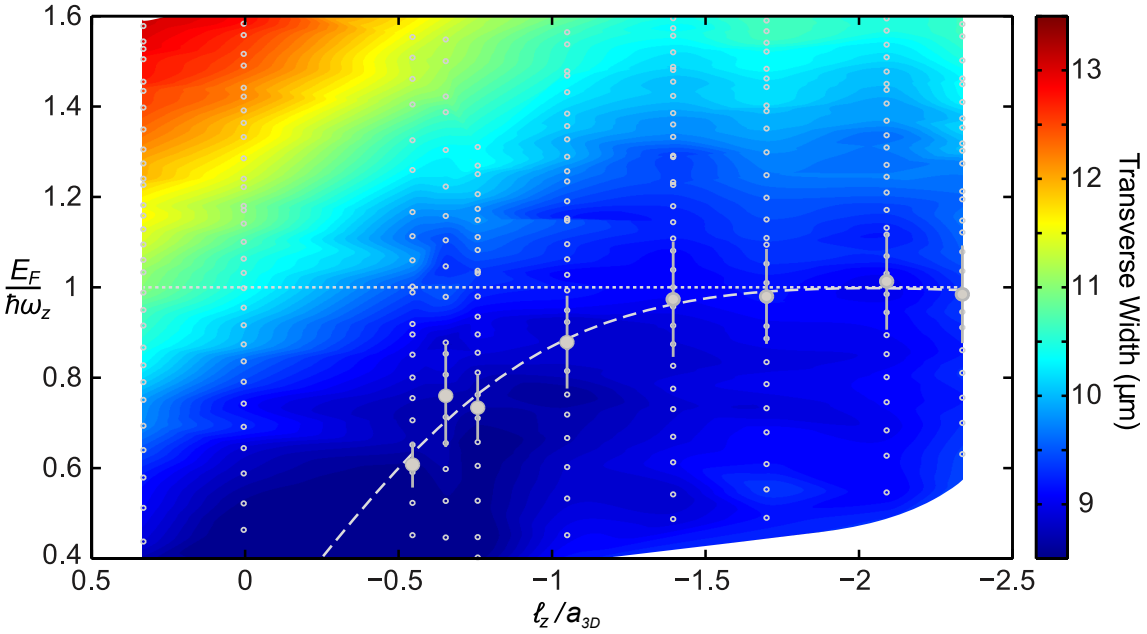

Figure 4.7: Crossover diagram for an interacting Fermi gas in two dimensions. The transverse width is shown as the false colour surface. Empty circles are the individual measurements for each magnetic field and the filled grey circles give the value of N_{2D}. The grey dashed curve is a guide to the eye and the horizontal white dotted line is the geometric limit for N_{2D}.

confined Fermi gases with densities and interactions above the dashed white line care must be taken when considering how the presence of transverse excitations may affect the gas. In this scenario direct comparison of experimental results with strictly two-dimensional theories may not be valid.

4.4 Conclusion

In this chapter the transverse width of an expanded Fermi gas originally confined to a highly anisotropic trapping potential was studied throughout the BCS-BEC crossover. This measurement revealed that, as interactions in the gas increase, finding transverse excitations in the gas appears to be unavoidable. This result was also compared to an exact two-body calculation for the expanded width throughout the crossover, where it was found that the two-body result behaves monotonically with the magnetic field, decreasing as the gas crosses from the far BCS to the far BEC regime. This is a markedly different result compared to the measurements which featured a peak in the transverse width slightly beyond the Feshbach resonance into the BEC side at

approximately 810 G. This result may provide a benchmark for future theoretical studies of two-dimensional Fermi gases as current theories cannot adequately describe the features observed in the strongly interacting region near the pole of the Feshbach resonance. This result also has implications for future experiments on two-dimensional Fermi gases, as even moderate interaction strengths on the BCS side result in detectable transverse excitations. While the exact nature of these excitations is unclear, we speculate that they may arise due to anharmonicity in the trapping potential resulting in a confinement induced resonance [Hal10; Pen11].

In Section 4.3 we set out to empirically determine the values of N_{2D} in the presence of interactions. This was achieved by fixing the magnetic field and therefore fixing the interactions and measuring the transverse width after time of flight expansion as a function of total atom number N. By observing an elbow in the measured width at the point where the width stops decreasing as N is reduced and becomes approximately constant, which indicates that only the transverse ground state is occupied. The atom number corresponding to this elbow marks the required atom number N_{2D}. Performing this measurement from the far BCS to just after the Feshbach resonance, N_{2D} decreases as the Feshbach resonance is approached from the BCS side and for the observable atom numbers the elbow is not present from the pole of the Feshbach resonance and below. This result establishes an appropriate parameter range in which the thermodynamics of an attractive two-dimensional Fermi gas can be studied.

Chapter 5

Thermodynamics of an attractive two-dimensional Fermi gas in the normal state

5.1 Introduction

Equations of state relate different thermodynamic state variables and are fundamental to understanding the behaviour of systems made up of a large number of particles. In the framework of statistical mechanics the understanding of ideal classical gases is obtainable through the determination of the equation of state of the system. As systems consisting of fermions confined to two-dimensional geometries become more prevalent, including superconductors [Dag94], atomically thin materials such as graphene [Has10] and other condensed matter systems such as liquid helium mono-layers [Bon98], understanding their fundamental thermodynamic properties is an important task. Due to the complex nature of these materials developing theoretical models that accurately describe their properties and behaviour is a challenge. Degenerate Fermi gases confined to two dimensions provide a simpler model which may be used to better understand the behaviour of more complex matter through the exploration of its thermodynamic properties and provide reliable benchmarks for comparisons with theory.

Experimental and theoretical explorations of these properties have been previously

performed on Fermi gases in three dimensions [Nav10; Nas10; Hor10] with more recent experiments able to precisely determine the critical temperature for superfluidity in the unitary regime [Ku12]. A number of studies of the thermodynamics of two-dimensional Bose gases have also been conducted [Rat10; Yef11; Des14]. For the case of fermionic systems in two dimensions, theoretical studies have been put forward [Ber11; Bau14; And15] with some preliminary experiments exploring the ground state pressure made by Makhalov *et al.* [Mak14]. This chapter presents the first experimental measurement of the equation of state of an attractive two-dimensional Fermi gas in the normal state. Shortly after our determination of the equation of state, a measurement of the density equation of state over the crossover was made by Boettcher *et al.* [Boe16] focusing on the Bose side of the crossover. This work complements the results presented in this chapter. With these combined results a fuller picture of the equation of state throughout the BKT-BCS crossover is available. The results contained in this chapter have appeared in the following publication [Fen16b].

5.2 Thermodynamics of Fermi gases in two dimensions

5.2.1 Local density approximation

The gases produced in the lab are inhomogeneous due to the harmonic confinement. If the confining potential varies slowly compared to the length scale of the interparticle spacing the change in quantum pressure is small and can be ignored [Hun14]. Hence we can treat the gas as being locally homogeneous. The chemical potential μ of these local regions is shifted due to the trapping potential giving a local chemical potential $\mu(\mathbf{r}) = \mu_0 - V(\mathbf{r})$, where $V(\mathbf{r})$ is the trapping potential at position $\mathbf{r}$ experienced by the atoms and μ_0 is the chemical potential at the centre of the trap where $V(\mathbf{r}) = 0$. In our experiment the coordinate $\mathbf{r}$ is the radial position away from the centre of the trap as we have a circularly symmetric trapping potential in the xy-plane.

We consider a single local region of the gas which is in thermal equilibrium and remains in contact with a reservoir of atoms contained in the rest of the trapped gas [Dal99a]. This region can be considered as an open system with constant tem-

perature T but variable atom number N. Systems satisfying these two conditions can be described by the grand canonical ensemble representation. In the grand canonical ensemble the macroscopic thermodynamics are described by the thermodynamic potential

$$\Omega(T,\mu,V) = U - TS - \mu N \tag{5.1}$$

where U is the internal energy, T is the absolute temperature, S is the entropy, μ is the chemical potential and N is the number of particles. With a system in thermal equilibrium the grand potential is minimised such that $\mathrm{d}\Omega = 0$. Taking the derivative of equation (5.1) and using Euler's equation the change in the grand potential is

$$\mathrm{d}\Omega = \mathrm{d}U - S\mathrm{d}T - T\mathrm{d}S - \mu\mathrm{d}N - N\mathrm{d}\mu \tag{5.2}$$

$$= -p\mathrm{d}V - V\mathrm{d}p \tag{5.3}$$

here we have used the fact that $\mathrm{d}U$ which can be determined by applying Euler's relation to the function $U(S,V,N)$ is given as

$$\mathrm{d}U = T\mathrm{d}S + S\mathrm{d}T - p\mathrm{d}V - V\mathrm{d}p + \mu\mathrm{d}N + N\mathrm{d}\mu\,. \tag{5.4}$$

From this the grand potential for a homogeneous gas is simply $\Omega = -PV$, where P is the system pressure and V is the system volume. By relating the Gibbs free energy G to the internal energy U using the same procedure as above the well known Gibbs-Duhem equation is found

$$V\mathrm{d}P - S\mathrm{d}T - N\mathrm{d}\mu = 0\,. \tag{5.5}$$

The Gibbs-Duhem equation allows us to determine the i^{th} thermodynamic variable provided we can measure $i-1$ variables.

5.2.2 The ideal gas

Before discussing the thermodynamic properties of interacting Fermi gases in two dimensions it is useful to first describe the case of the ideal gas. Unlike the three-dimensional case in which many properties can only be determined numerically, for the two-dimensional Fermi gas many of the ideal gas properties are analytically solvable. In Section 2.2.1 the density of states was derived in equation (2.9) and some of the zero temperature properties were derived. Here we are now interested in the non-zero temperature properties of the gas. From the density of states $g_{2D}(\varepsilon) = \frac{Am}{2\pi\hbar^2}$ one can begin to derive these properties. Starting with the chemical potential μ, which can be determined through the integration of the Fermi-Dirac distribution, we find for a homogeneous gas

$$\mu = \frac{1}{\beta} \ln\left[-1 + e^{\lambda^2 n}\right] \tag{5.6}$$

where $\beta = 1/k_B T$, $\lambda = \sqrt{2\pi\hbar^2/mk_B T}$ is the thermal de Broglie wavelength and n is the density. The energy can be determined by the integral $\int_0^\infty \varepsilon g_{2D}(\varepsilon) n_{FD}(\varepsilon, \mu, T) \mathrm{d}\varepsilon$, where $n_{FD}(\varepsilon, \mu, T)$ is the Fermi-Dirac distribution. Completing the integral the total energy is then

$$U(\mu, T) = -\frac{g_{2D}}{\beta^2} Li_2\left(e^{\beta\mu}\right) \tag{5.7}$$

where Li_2 is the polylogarithm function of order two. In general, polylogarithm functions can be computed by the series

$$Li_n(z) = \sum_{i=1}^{\infty} \frac{z^i}{i^n}. \tag{5.8}$$

For a gas in thermal equilibrium the pressure and isothermal-compressibility can be determined from the standard thermodynamic relations $P = \frac{\partial U}{\partial V}$ and $\kappa = -\frac{1}{V}\frac{\partial V}{\partial P}$,

for an ideal Fermi gas in two dimensions these are

$$P = -\frac{1}{\lambda^2 \beta} Li_2(-\beta\mu) \tag{5.9}$$

$$\kappa = \frac{\beta}{(n\lambda)^2}(e^{\beta\mu}). \tag{5.10}$$

For the analysis of the equation of state we want to work with dimensionless variables, so we can normalise P and κ by their respective zero temperature results

$$P_0 = -\frac{\partial U}{\partial V} = \frac{\partial}{\partial A}(\frac{\pi\hbar^2}{m}\frac{N^2}{A}) = \frac{\pi\hbar^2}{m}n^2 \tag{5.11}$$

$$= \frac{nE_F}{2} \tag{5.12}$$

$$\kappa_0 = -\frac{1}{V}\frac{\mathrm{d}V}{\mathrm{d}P} = -\frac{1}{A}\frac{\mathrm{d}A}{\mathrm{d}P} = -\frac{\pi\hbar^2 N^2}{2mA^3} \tag{5.13}$$

$$= \frac{1}{nE_F} \tag{5.14}$$

where n is the density and $E_F = \frac{\pi\hbar^2}{m}n$ is the Fermi energy. Normalising equations (5.9) and (5.10) with equations (5.12) and (5.14) will allow the determination of the dimensionless parameters which are required to determine the thermodynamics [Ku12; Des14] as will be discussed in Section 5.3. Additional thermodynamic properties such as the entropy and specific heat can be determined through appropriate combinations of equations (5.7) – (5.10). In the following sections the extension of these thermodynamics to the high temperature limit for an interacting gas will be made.

5.2.3 High temperature equation of state through the virial expansion

The virial expansion can accurately describe the thermodynamic properties of an interacting gas at high temperature. As the virial expansion is a perturbative method it relies on the existence of a small parameter in the system on which the perturbation is applied. In the high temperature regime this parameter is the fugacity $z = \exp(\beta\mu)$ which tends to zero as the temperature increases and μ becomes negative. As we are describing the thermodynamics in the grand canonical ensemble, the grand potential

can be expanded in powers of z in order to determine the corresponding virial coefficients Δb_n. These coefficients depend on the interaction strength βE_b. The second order virial coefficient can be determined using the Beth-Uhlenbeck formalism [Liu13] and is given as [Liu10; Fen16a]

$$\Delta b_2 = e^{\beta E_b} - \int_{\infty}^{\infty} \exp\left[\frac{e^{2t}}{2\pi}\frac{2}{\pi^2 + 4(t-x)^2}\right] \tag{5.15}$$

where $x = \frac{1}{2}\ln(2\pi\beta E_B)$ [Fen16a]. As the calculation of the nth order coefficient Δb_n requires the solution of an n-body system, coefficients of order $n > 2$ become increasingly difficult to determine. The value for Δb_3 has been calculated for the case of a harmonically trapped three-body system in [Liu10] and for the homogeneous gas via the solution of Feynman diagrams in [Ley11; Nga13]. Within the range of interaction strengths $0.003 < \beta E_b < 1.0$ which our experiments fall within, Δb_3 can be described by a polynomial fit to the full result

$$\Delta b_3 = -\sum_{n=0}^{7} a_n x^n \tag{5.16}$$

here the coefficients a_n are $a_0 = 0.45938$, $a_1 = 0.40400$, $a_2 = 0.31103$, $a_3 = 0.16998$, $a_4 = 0.17801$, $a_5 = 0.23461$, $a_6 = 0.13623$ and $a_7 = 0.02685$. In figure 5.1, the dependence of Δb_2 and Δb_3 with interaction strength is shown. With knowledge of

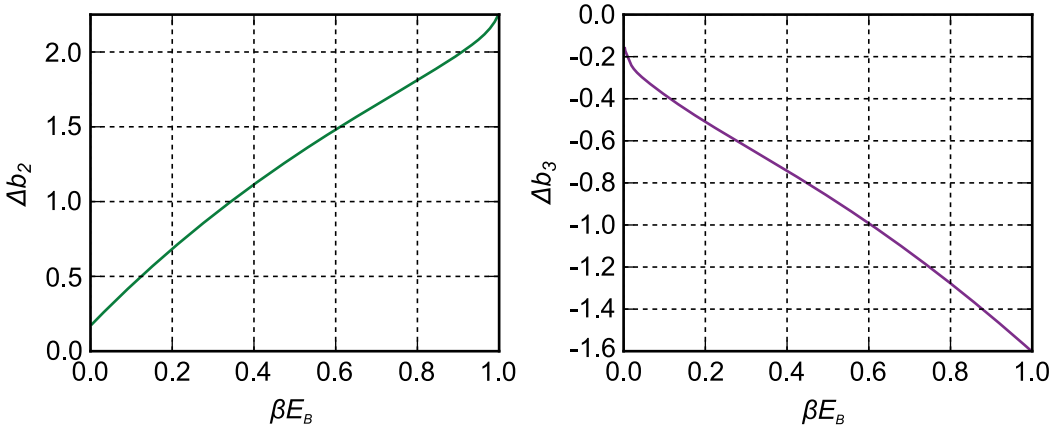

Figure 5.1: Second and third order virial coefficients for a two-dimensional Fermi gas. For interaction strengths $0 \leq \beta E_B \leq 1$.

the virial coefficients we can determine the high temperature thermodynamics of the

system.

As we measure the density distribution in our experiments it is useful to begin with the virial expansion representation of the density, given in equation (5.17), which can be used to describe the high temperature wings of the atom cloud

$$n(\mathbf{r}) = \frac{2}{\lambda^2}\left[\ln(1+z(\mathbf{r})) + 2\Delta b_2 z(\mathbf{r}) + 3\Delta b_3 z(\mathbf{r})^3 + \dots\right] \tag{5.17}$$

where $z(\mathbf{r}) = e^{\beta[\mu_0 - V(\mathbf{r})]}$ is the local fugacity.

In our experiments we will show in Section 5.3 that the important experimentally accessible thermodynamic properties are the isothermal compressibility κ and the pressure P. Using the same thermodynamic relation as for the ideal gas and using the virial coefficients we can determine the isothermal compressibility as

$$\kappa = \frac{2\beta}{(n\lambda^2)}\left[\frac{z}{1+z} + 4\Delta b_2 z^2 + 9\Delta b_3^3 + \dots\right]. \tag{5.18}$$

Likewise the pressure can be determined from the following

$$P = \frac{2}{\beta\lambda^2}\left[\int_0^\infty \ln\left(1+ze^{-t}\right)\mathrm{d}t + \Delta b_2 z^2 + \Delta b_3 z^3 + \dots\right]. \tag{5.19}$$

Finally from the density given in equation (5.17) we can define the dimensionless temperature $\tilde{T} \equiv T/T_F$ as

$$\tilde{T} = \left[\ln(1+z) + 2\Delta b_2 z^2 + 3\Delta b_3 z^3 + \dots\right]^{-1}. \tag{5.20}$$

The above results are valid in the high temperature limit and provide a robust benchmark with which the measured thermodynamic properties can be compared.

5.3 Measurement of the equation of state

The thermodynamic properties of an interacting two-component Fermi gas can be described by a set of dimensionless universal functions [Ho04]. As the thermodynamic quantities in the gas are functions of temperature T, chemical potential μ and inter-

action a_{2D} which is quantified through the two-body binding energy E_B, we can define these functions f through dimensionless combinations of these three energy scales and define the universal functions $f(\beta\mu, \beta E_B)$.

Due to the fact that the gases studied in experiments are prepared at thermal equilibrium at a fixed temperature and magnetic field, the value of βE_B across the gas will be constant for any given experimental run. The pressure P, density n and isothermal compressibility κ are related to the function $f(\beta\mu, \beta E_B)$ in the following way, beginning with the dimensionless pressure

$$\beta\lambda^2 P = f_p(\beta\mu, \beta E_b)\,. \tag{5.21}$$

From the Gibbs-Duhem equation at fixed T and a_{2D} we have $n = \frac{\partial P}{\partial \mu}|_{T,a_{2D}}$, from which phase space density can be determined

$$n\lambda^2 = f_n(\beta\mu, \beta E_B) = f_p'(\beta\mu, \beta E_B)\,. \tag{5.22}$$

Finally, the dimensionless compressibility is found from the relation $\kappa = \frac{1}{n^2}\frac{\partial n}{\partial \mu}|_{T,a_{2D}}$

$$\frac{n^2\lambda^2}{\beta}\kappa = f_\kappa(\beta\mu, \beta E_b) = f_p''(\beta\mu, \beta E_b) \tag{5.23}$$

where $\beta = 1/(k_B T)$, $\lambda = \sqrt{2\pi\hbar^2/mk_B T}$ is the thermal de Broglie wavelength, $E_b = \hbar^2/(ma_{2D}^2)$ is the two-body binding energy, which is valid in the kinematically 2D limit [Pet01; Blo08; Lev15] and f_p' represents differentiation with respect to $\beta\mu$. The goal in our experiment is to determine these universal functions.

While the density $n(V)$ is known from our measurement as a function of the trapping potential, μ remains unknown. To overcome this the local density approximation can be used. To recall briefly, within the LDA the chemical potential μ is related to the trapping potential by $\mu(\mathbf{r}) = \mu_0 - V(\mathbf{r})$. Using this we can write for a gas in thermal equilibrium and constant interactions the change in the chemical potential $\mathrm{d}\mu = -\mathrm{d}V$.

Finally, we can express the pressure in terms of observable quantities n and V

$$P = \int -n(V)dV\,. \tag{5.24}$$

Likewise, we can derive the isothermal compressibility κ of the system. In terms of the chemical potential the isothermal compressibility is defined as $\kappa = \frac{1}{n^2}\frac{dn}{d\mu}$. Following the transformation of $d\mu$ as before we can write κ under the LDA as

$$\kappa = -\frac{1}{n^2}\frac{dn(V)}{dV}\,. \tag{5.25}$$

In order to construct a dimensionless equation of state we normalise P and κ by their non-interacting zero-temperature equivalents P_0 and κ_0 given by equations (5.12) and (5.14). Experimentally, we initially prepare the gas as described in Chapter 3. Once the gas is confined to the TEM_{01} mode trap we reduce the atom number through the application of the magnetic gradient described in Section 3.3.4 to be within the kinematically two-dimensional region determined in the previous chapter. The Feshbach magnetic field is then swept to the desired position in the BCS-BEC crossover over 200 ms and the gas is held between 250 ms and 750 ms depending on the interaction strength to allow for equilibration. Immediately after the equilibration the gas is imaged *in situ*.

As the analysis requires numerical derivatives which can enhance noise, a number of steps are undertaken in order to improve the measurement of κ. Due to the low optical thickness of our samples we perform absorption imaging at low intensity with longer exposure times to enhance signal-to-noise as described in Section 3.4. We obtain 200 shots at each interaction strength and in doing so the overall statistical error of the measurement of κ is reduced.

From the 200 *in situ* profiles principal component analysis (PCA) is performed to reduce the noise further. Principal component analysis is a dimensionality reduction technique commonly used to reduce background noise [Jol02] by reducing the information held in the images to a series of eigenvectors which describe different elements of variation within the data set. Due to the nature of repeated measurement of nearly identical clouds, most variation in the images is due to noise and as such this method

lends itself nicely to reducing the overall level of noise in the images [Des13; Dub14].

In order to compute the principal components the average of all 200 images is computed and subtracted from each individual image. The individual images are reshaped from a 256×256 matrix to a single column vector of dimensions 1×65536. These new image column vectors are combined to form a new matrix $\mathbf{A}$ with dimensions $N \times N_{pixel}$ where N is the total number of images and $N_{pixel} = 65536$ is the total number of pixels in a single image. The covariance matrix of $\mathbf{A}$ is calculated and diagonalised. The resulting eigenvalues describe the amount of variance for a given principal component and the eigenvectors $\mathbf{E}$ are the components.

In the experiment the first 20 principal components are retained which contain $\sim 95\%$ of the observed variance in the images. The new images can be reconstructed using only these components by forming a projection of the original data in the new basis given by the selected components.

In a final step we make use of the radially symmetric nature of the trap and perform an azimuthal averaging of each individual profile. Examples of our measured 2D density and corresponding azimuthally averaged line profile are shown in figure 5.2.

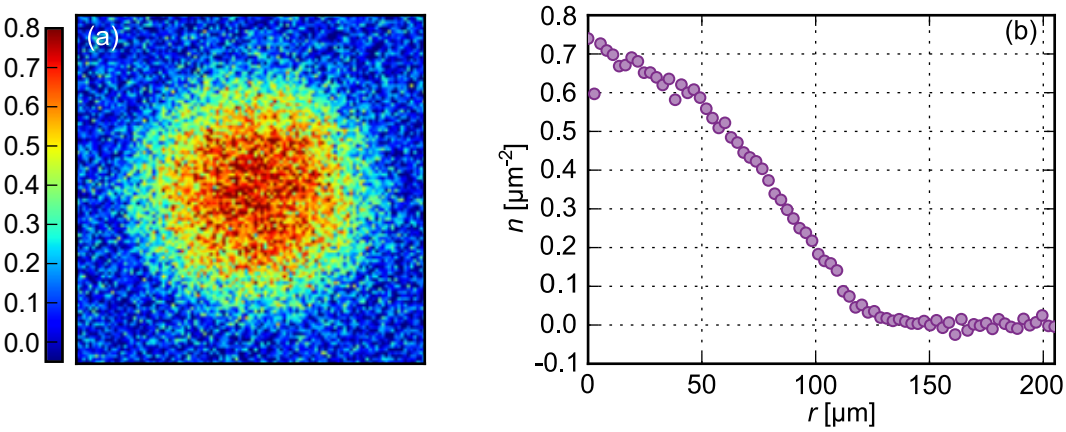

Figure 5.2: In (a) the 2D optical density of an average of 10 shots is shown and in (b) the resulting radially averaged density profile.

Using these line profiles we can compute P and κ as given in equations (5.24) and (5.25). After normalisation of P and κ by their zero temperature results P_0 and κ_0 the dimensionless compressibility equation of state $\tilde{\kappa}(\tilde{p})$ can be determined. Before performing the full thermodynamic analysis it is necessary to establish an initial temperature estimate and density correction using the virial expansion.

5.3.1 Temperature estimation and density correction

Due to a lack of scale invariance in two dimensions, the virial expansion coefficients Δb_2 and Δb_3 depend on βE_B and therefore when we want to fit the virial expansion to the measured density we must already know the temperature of the gas. The density $n(V)$ can be determined using equation (5.17). Due to the fact that the virial expansion is only valid at high temperatures, or more precisely when $\beta\mu \ll 0$, we are limited to only using the high tempeature wings of the cloud where the relative temperature T/T_F is largest. To circumvent the need to know *a priori* the temperature, the fitting procedure we use is iterated and a bisection algorithm applied for different starting values of $(\beta E_B)_{guess}$ until the resulting value $(\beta E_B)_{fit}$ converges. We take this final value of βE_B to determine T, as we have precise knowledge of the binding energy E_B through our measurement of the transverse trap frequency ω_z and the three-dimensional s-wave scattering length a_{3D}. The temperature obtained from the fitting procedure is used to determine the initial known equation of state for the full thermodynamic analysis. Figure 5.3 shows an example of the in-trap density fit to the wings of a cloud imaged at a magnetic field of 972 G after applying the iterative fitting procedure.

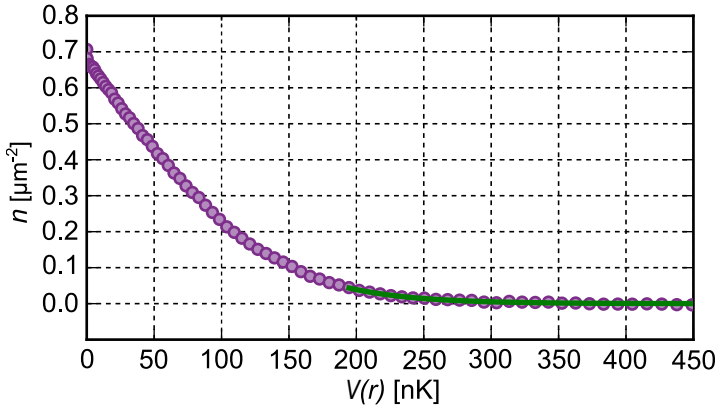

Figure 5.3: Virial expansion fit to the measured in-trap density distribution for a magnetic field of 972 G. After convergence of the fitting routine, the final value of βE_B was determined to be 0.005(1).

We also use the virial fitting procedure to improve upon the density correction factor to be applied to the measured density. Beginning with the correction factor found in Section 3.4.1 which is determined using both high and low intensity images,

we iteratively fit the virial expansion to the wings of the cloud while varying this correction factor. When using the incorrect scaling we observe systematic errors in the resulting fit. Using this process we can improve on the accuracy of our density scaling factor compared to the method described in Section 3.4.1. For the data used in our analysis the correction factors found using both methods are listed in table 5.1. With

Magnetic Field [G]	C_{OD} (High/Low)	C_{OD} (Virial)	βE_B
972	1.27(8)	1.21(3)	0.005(1)
920	1.24(17)	1.20(4)	0.06(1)
880	1.20(12)	1.21(3)	0.29(5)
865	1.24(13)	1.22(2)	0.49(5)

Table 5.1: Final values of C_{OD} found for each magnetic field. The second column gives the value found by the method of taking the ratio of optical density of high intensity and low intensity imaging. The value listed is the mean value of the correction with error given by the standard error. The third column gives the value found after fitting with the third-order virial and the final column lists the values of βE_B found using this iterative fitting method. For all values the errors listed are the 95% confidence interval from the fitting procedure.

these improved correction factors and knowledge of βE_B from the virial fits, the virial expansion compressibility equation of state shown as the dashed lines in figure 5.4 are constructed. We can now use these these measured high temperature equation of states as starting parameters for the full thermodynamic analysis.

5.3.2 Density and pressure equation of state

From the dimensionless equation of state $\tilde{\kappa}(\tilde{p})$, presented in figure 5.4, we can extract the dimensionless temperature $\tilde{T} = \frac{T}{T_F}$ and dimensionless chemical potential $\beta\mu$. To achieve this we relate the reduced pressure and compressibility to the universal functions in the following way. Beginning with the universal functions given in equations (5.21) – (5.23). The reduced pressure $\tilde{p}$ can be written as

$$\tilde{p} = \frac{P}{P_0} = \frac{1}{\beta\lambda^2} f_p \frac{2}{nE_F} \tag{5.26}$$

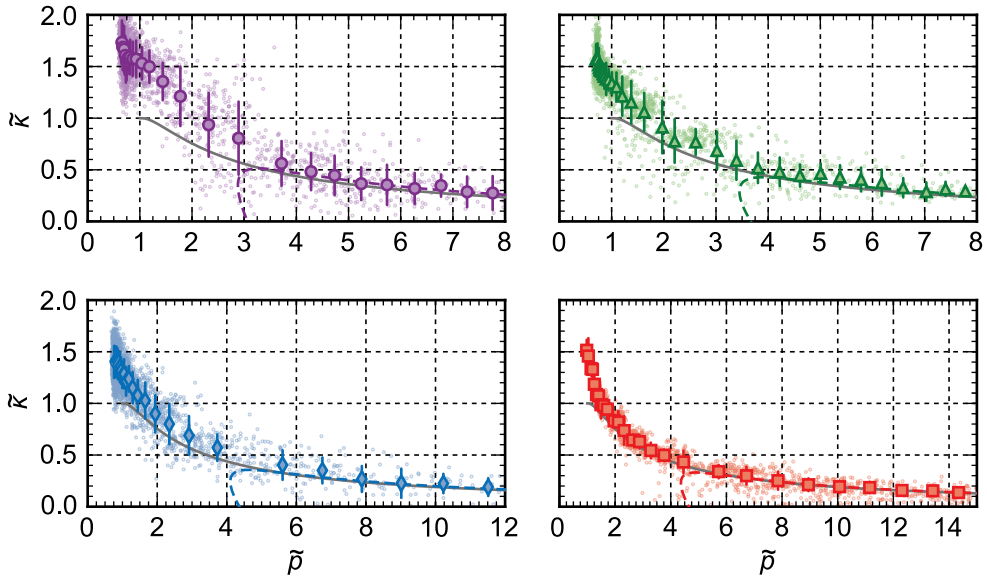

Figure 5.4: Compressibility equation of state $\kappa(\tilde{p})$ for 4 different interaction strengths (clockwise $\beta E_B = 0.47$, 0.26, 0.06 and 0.005). The small points are the individual pressure and compressibility from each image. Larger points (circle, triangle, diamond and square) are the binned result which is used to extract the thermodynamics. In each plot the virial (dashed line) is given for each value of βE_B and the solid grey line is the ideal gas result.

we can further relate this to our additional universal functions through the density n given by equation (5.22) leaving us with the following definition of $\tilde{p}$

$$\tilde{p} = 2\frac{T}{T_F}\frac{f_p}{f_p'}. \tag{5.27}$$

Similarly, we can find the reduced compressibility $\tilde{\kappa}$

$$\tilde{\kappa} = \frac{\kappa}{\kappa_0} = \frac{\beta}{n^2\lambda^2} f_p'' n E_F. \tag{5.28}$$

In order to determine $\frac{T}{T_F}$ and $\beta\mu$, an expression for how our measured quantities change in terms of these variables is required. Performing the required differentiation

of equation (5.27) the following expressions are obtained

$$\frac{\mathrm{d}\tilde{p}}{\mathrm{d}\tilde{T}} = 2\tilde{T}^{-1}\left[\tilde{p} - \frac{1}{\tilde{\kappa}}\right] \tag{5.29}$$

$$\frac{\mathrm{d}\tilde{p}}{\mathrm{d}(\beta\mu)} = 2\tilde{T}(1-\tilde{p}\tilde{\kappa})\,. \tag{5.30}$$

Equivalent equations can also be obtained through the differentiation of equation (5.28). Integrating the above equations we can extract $\frac{T}{T_F}$ and $\beta\mu$. For the reduced temperature we obtain

$$\tilde{T} = \tilde{T}_i \exp\left[\frac{1}{2}\int_{\tilde{p}_i}^{\tilde{p}} \frac{1}{\tilde{p} - \frac{1}{\tilde{\kappa}}}\mathrm{d}\tilde{p}\right] \tag{5.31}$$

where $\tilde{T}_i$ and $\tilde{p}_i$ are the reduced temperature corresponding to a value of the dimensionless pressure taken from a known region of the equation of state. The known region is taken from the wings of the density distribution as within this region the relative temperature $\tilde{T}$ is large and the virial expansion can be used to exactly determine the values of $\tilde{p}$, $\tilde{\kappa}$, as described in Section 5.3.1. For even higher temperatures it would be possible to determine the initial parameters by fitting a Boltzmann distribution to the wings of the density distribution.

In order to determine the dimensionless chemical potential $\beta\mu$ requires the integration of equation (5.30) resulting in the following equation

$$\beta\mu = (\beta\mu)_i + \frac{1}{2}\int_{\tilde{p}_i}^{\tilde{p}} \frac{1}{\tilde{T}}\frac{1}{1-\tilde{\kappa}\tilde{p}}\mathrm{d}\tilde{p}\,. \tag{5.32}$$

Like the temperature integral in equation (5.31) $(\beta\mu)_i$ is a value corresponding to the point $\tilde{p}_i$ in a known region of the equation of state previously determined from the virial expansion. While these integrals provide the same information as can be obtained from the virial expansion fit, their determination can provide a check on any numerical noise in the measured values of $\tilde{\kappa}$ and $\tilde{p}$ and allow a more accurate determination of T and μ_0 as the virial expansion can only be performed over a small portion of the trapped gas.

Having determined the temperature and chemical potential for each realisation of

the gas we can examine the density equation of state for an attractive Fermi gas in two dimensions. The homogeneous density is determined from equation (5.22). While f_n is unknown, it can be related to our measured quantities. Starting with the Fermi energy $E_F = \frac{\pi\hbar^2}{m}n$ and inserting equation (5.22) we obtain

$$E_F = \frac{\pi\hbar^2}{m}\frac{1}{\lambda^2}f_n \tag{5.33}$$

where m is the atomic mass, $\hbar$ is the reduced Plank constant, $\lambda = \sqrt{\pi\hbar^2/mk_BT}$ is the de Broglie wavelength and f_n is the universal thermodynamic function. With some algebraic manipulation we can show f_n is given by

$$f_n = 2\frac{T_F}{T}\,. \tag{5.34}$$

Therefore, by the determination of equation (5.31), we can obtain the homogeneous density as a function of $\beta\mu$. To elucidate the role of interactions we can examine the departure of the interacting gas from that of the ideal gas by normalisation of the density with the density of an ideal gas for the same values of temperature and chemical potential. This normalisation is given by

$$n_0 = \frac{2}{\lambda^2}\ln\left(1+e^{\beta\mu}\right). \tag{5.35}$$

Figure 5.5 shows the resulting normalised density equation of state for a range of interaction strengths.

A qualitatively different dependence on $\beta\mu$ between the three-dimensional equation of state shown in figure 5.6 for a Fermi gas at unitarity and the two-dimensional Fermi gas can be seen immediately as in two dimensions the dependence of the equation of state with $\beta\mu$ is non-monotonic and exhibits a peak in the region $\beta\mu \sim 1$. This non-monotonic behaviour has been seen in simulations using both the self-consistent GG t-matrix (Luttinger-Ward) approach [Bau14] and also in the lattice quantum Monte Carlo (LQMC) approach [And15]. The approximate locations and heights of the peaks differ slightly between the two calculations. For the experimental data at interaction strengths comparable to available theory there is good agreement with the predicted

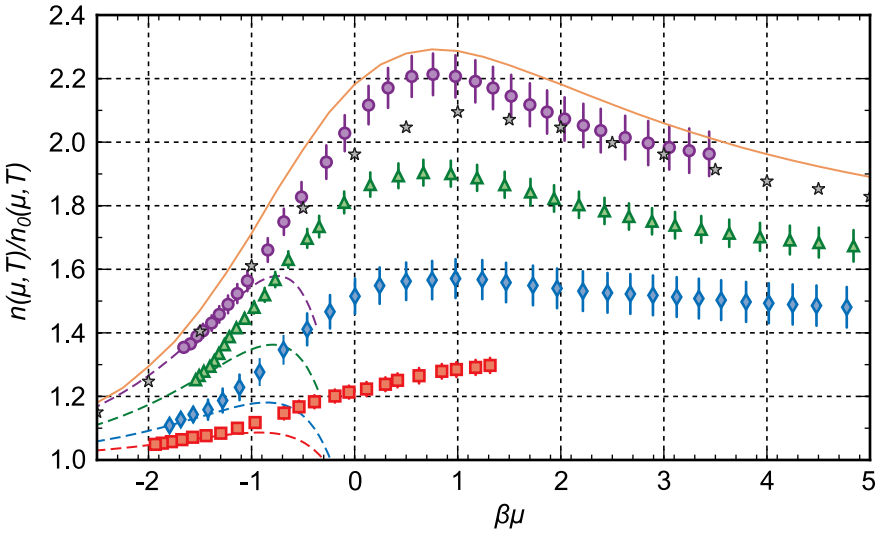

Figure 5.5: Density equation of state of a two-dimensional Fermi gas, corresponding to values of $\beta E_B = 0.005(1), 0.06(1), 0.26(2), 0.47(3)$ (bottom to top). Dashed lines of the same colour are the results of the density equation of state determined by the virial expansion. Included are theoretical calculations for $\beta E_B = 0.5$ where the orange solid line is the Luttinger-Ward model [Bau14] and grey stars is a Lattice-Quantum Monte Carlo calculation [And15].

behaviour of n/n_0. More recent comparisons between a number of strong coupling theories suggest that the GG model describes the measured experimental results most accurately [Mul15]. The peak in the density equation of state arises in two dimensions as a consequence of the presence of the two-body bound state. With a_{2D} fixing E_B, for all gases examined we have $\beta E_B < 1$, meaning that for a gas in thermal equilibrium the thermal energy of the system $k_B T > E_B$. In the low density regions of the gas where $E_F \ll k_B T$ the average kinetic energy E_k of the colliding particles within the gas is set by the thermal energy $k_B T$. As $\beta\mu$ increases so does the density of the gas increasing the effect of interactions between particles. For $\beta\mu > 1$, $E_F > k_B T$ and the Fermi energy becomes the dominant energy scale which increases the average energy of colliding particles above $k_B T$. As the density increases the Fermi energy continues to increase over the binding energy resulting in a decrease in the effect of the interactions and hence in n/n_0 above $\beta\mu \approx 1$.

The effect of the ratio E_k/E_B can be understood by looking at the two-body scat-

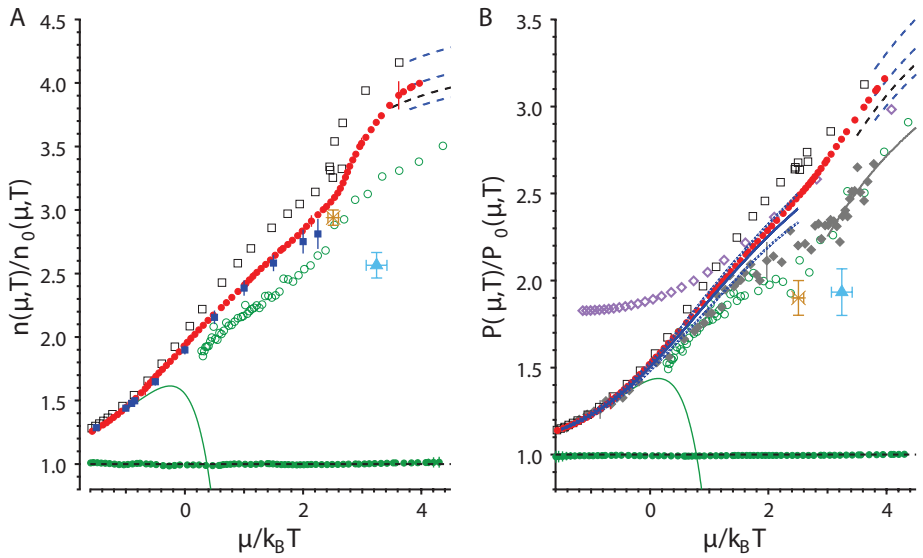

Figure 5.6: Normalised density (A) and pressure (B) equations of state for 3D Fermi gas at unitarity. We compare our result to the solid red circles which represent the latest experimental measurement from Ku *et al.*, the green solid line is the thrid order virial expansion. Additional data shown are from a range of experimental and theoretical results. Details and references for these points are in the referenced text. From M. J. H Ku, A. T. Sommer, L. W. Cheuk and M. W. Zwierlein, "Revealing the Superfluid Lambda Transition in the Universal Thermodynamics of a Unitary Fermi Gas" *Science* **335**, 563 (2012). Reprinted with permission from AAAS.

tering amplitude in two dimensions

$$f = -\frac{4\pi}{2\ln(ka_{2D}) - i\pi} = -\frac{4\pi}{\ln(E_k/E_B) - i\pi} \tag{5.36}$$

where the parametrising value (ka_{2D}) has been rewritten in terms of the ratio of the Fermi energy to the two-body binding energy $(ka_{2D})^2 = E_k/E_B$. The scattering amplitude f which describes the probability of two particles scattering is maximised when $E_k/E_B = 1$ and the logarithmic term in the denominator goes to zero. For increasing E_k/E_B, as we have in the region where the Fermi energy is the dominant energy scale the scattering amplitude decreases asymptotically as this ratio increases and the gas becomes more weakly interacting.

In terms of T/T_F and $\ln(k_F a_{2D})$, the gas experiences the competing pull of these two parameters. As the density increases, T/T_F decreases and the gas becomes increasingly degenerate and the effect of interactions increases. At the same time, however, $\ln(k_F a_{2D})$ becomes larger and positive with increasing density, resulting in a de-

crease in interactions as the gas enters deeper into the weakly interacting BCS regime. This interplay of interactions and relative temperature indicate that it is at intermediate temperatures where the interactions play the most significant role in the gas, unlike the three-dimensional Fermi gas where the strongest interactions are found in the region in which the density is highest. For the interaction strengths examined this dependence between T/T_F and $\ln(k_F a_{2D})$ is shown in figure 5.7.

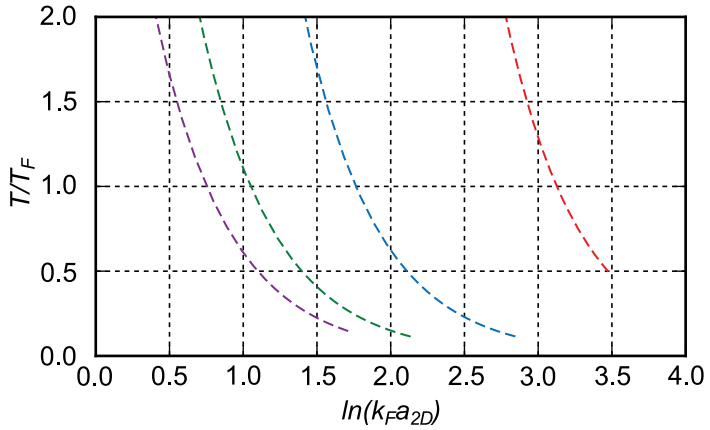

Figure 5.7: Dependence of the relative temperature T/T_F on interactions. Increasing $\ln(k_f a_{2D})$ results in progressively weaker interaction strength. At lower values of the reduced temperature, the density increases and the overall interaction strength is decreased.

We find that even for the case of a weakly interacting Fermi gas $\beta E_B = 0.005(1)$ (red squares) in figure 5.5 a significant departure from the density of an ideal gas is observed.

In addition to the density equation of state we can also extract the pressure equation of state, shown in figure 5.8. As we related f_n to the measurable thermodynamics we can repeat this for f_p, giving

$$f_p = \tilde{p}\left(\frac{T_F}{T}\right)^2 \tag{5.37}$$

using this we can then determine the pressure equation of state normalised by the pressure of an ideal gas at the same temperature and chemical potential as was done

for the density. This normalisation is determined by

$$P_0(\mu, T) = -\frac{2}{\beta\lambda^2} Li_2(\beta\mu). \tag{5.38}$$

Similar to the density, we observe a non-monotonic dependence on $\beta\mu$, however now with a less prominent peak.

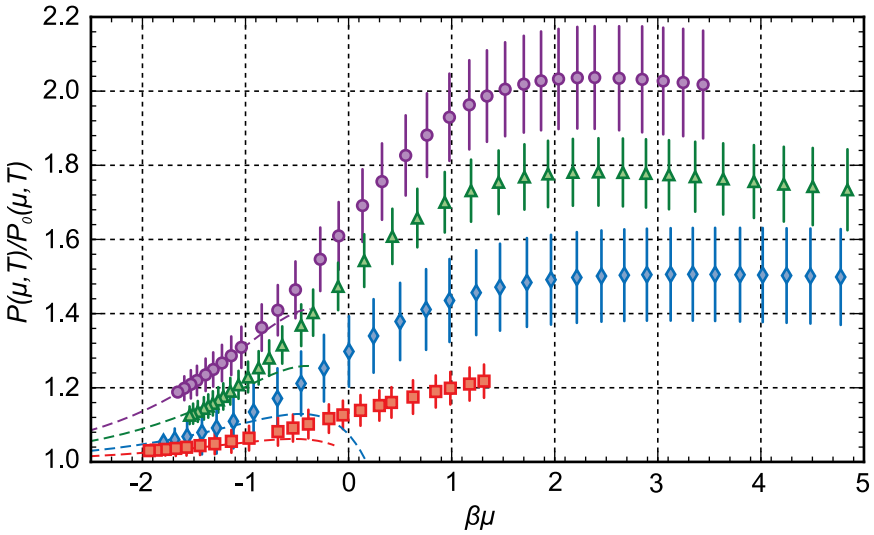

Figure 5.8: Pressure equation of state of a two-dimensional Fermi gas, corresponding to values of $\beta E_B = 0.005(1), 0.06(1), 0.26(2), 0.47(3)$ (bottom to top). Dashed lines of the same colour are the results of the density equation of state determined by the virial expansion.

5.3.3 Chemical potential, internal energy and entropy

In addition to being able to extract the density and pressure equations of state we can also access other thermodynamic properties of the gas such as the chemical potential, internal energy, etc.

It has been shown that the chemical potential can be extracted at any given point via an integral starting in a region of known chemical potential. It is also possible to straight forwardly extract the Helmholtz free energy F defined as

$$F = U - TS \tag{5.39}$$

using the Gibbs-Duhem equation the energy can be written as

$$U = TS + \mu N - PV \tag{5.40}$$

$$U - TS = \mu N - PV \tag{5.41}$$

by converting equation (5.41) to dimensionless form and substituting the result into equation (5.39) we obtain the dimensionless Helmholtz free energy $\tilde{F} = F/(NE_F)$

$$\tilde{F} = \frac{\mu}{E_F} - \frac{1}{2}\tilde{p}\,. \tag{5.42}$$

Both the internal energy $\tilde{U}$ and Helmholtz free energy $\tilde{F}$ are shown in figure 5.9. Un-

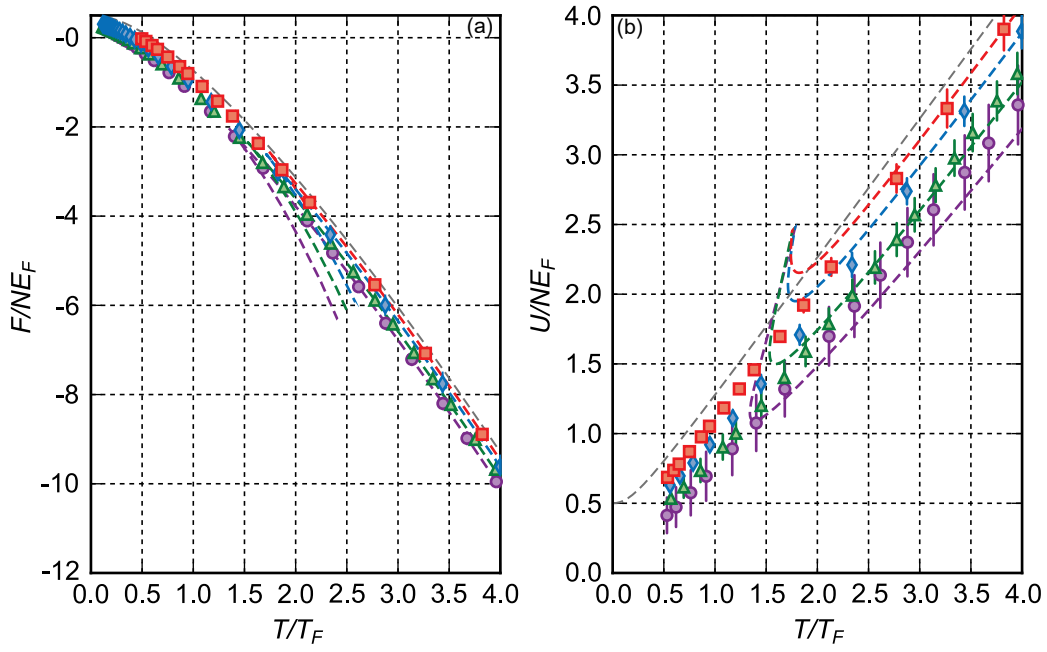

Figure 5.9: Panel (a) shows the free energy of the system, with the corresponding virial expansion result shown as the dashed line, where colour and symbol are the same as in figure 5.5. The free energy of the ideal gas shown as the dashed grey line. Panel (b) shows the internal energy for each interaction strength. For the largest interaction strength a shift away from the high-temperature result is due to the fact the derivative can only be performed using the single point backwards derivative and not a two-point forward/backwards difference.

like the unitary Fermi gas, where the internal energy is given by the universal result $U = 3PV/2$ [Ho04], it is not as straight forward to extract the internal energy or entropy from simple combinations of the already obtained thermodynamics at a single

interaction strength. To solve this problem using a single experimental run would require the measurement of the Contact parameter C for a gas of equivalent βE_B. This could be achieved via Bragg spectroscopy as previously examined in three dimensions [Kuh11; Hoi13; Lin14] and in two dimensions [Frö12]. However, this requires the completion of an entirely new experiment.

In keeping with the idea that all thermodynamics can be measured using *in situ* absorption images we can make use of the fact that the contact itself is a thermodynamic variable and use Tan's adiabatic relation in two dimensions $\frac{\mathrm{d}\tilde{F}}{\mathrm{d}\ln(a_{2D})} = \frac{2C}{k_F^4}$ [Val11; Wer12; Hof12]. As we have extracted the Helmholtz free energy $\tilde{F}$ at four unique values of a_{2D} we can compute the homogeneous contact by taking the derivative of $\tilde{F}$ at fixed values of T/T_F and use this to determine the internal energy and entropy. For each value of T/T_F the resulting numeric differentiation will be performed over only four data points, which leads to a significant uncertainty in the properties which are extracted using this method when compared to directly measured quantities such as μ/E_F, $\tilde{F}$ etc. In order to improve the quality of the differentiation we conduct a two-point derivative where possible using both forward and backward differentiation for the inner sets of data ($\beta E_B = 0.06, 0.26$). Points at either end can only be forward or backward differentiated resulting in increased uncertainty. As each set of data contains unique measured values of T/T_F dependent on the range and binning of $\tilde{p}$, the Helmholtz free energies are interpolated with a third-order spline to allow for differentiation across each data set at a fixed T/T_F. The range of temperatures are also limited to regions in which there is experimental data for each data set effectively bounding the range with the lowest temperature of the hottest cloud and the upper limit set by the highest temperature of the coldest cloud. This temperature range is approximately $0.5 < \frac{T}{T_F} < 4.0$ leaving us well within the normal phase. With this we can determine the internal energy U/NE_F from the Tan pressure relation $\tilde{p} = \frac{2U}{NE_F} + \frac{2C}{k_F^4}$ [Tan08; Val11; Hof12] as

$$\tilde{U} = \frac{U}{NE_F} = \frac{1}{2}\left[\tilde{p} - \frac{\mathrm{d}\tilde{F}}{\mathrm{d}(\ln(a_{2D}))}\right] \tag{5.43}$$

after performing the differentiation using the interpolated temperature scale for each

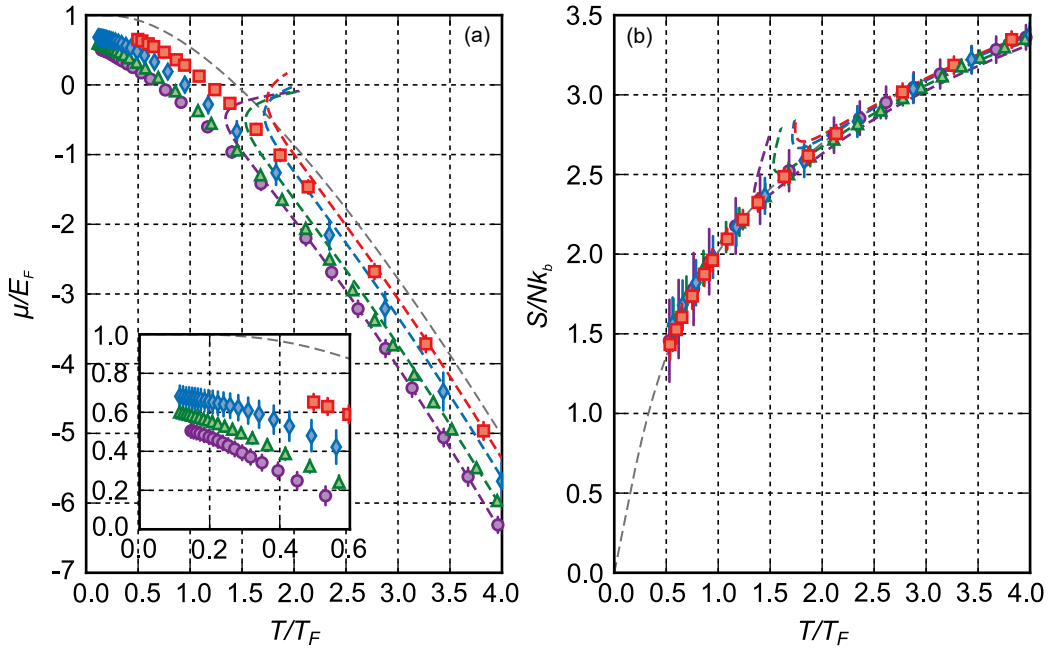

Figure 5.10: Panel (a) plots the dimensionless chemical potential and panel (b) the entropy per particle, corresponding to values of $\beta E_B = 0.005(1)$, $0.06(1)$, $0.26(2)$, $0.47(3)$ (top to bottom). Dashed lines of the same colour are the results determined by the virial expansion. The dashed grey line gives the result for an ideal two-dimensional Fermi gas. Inset of panel (a) is a zoomed in section of the low temperature chemical potential.

data set we extract from the interpolated data only the values at T/T_F which correspond to the experimental data and using the experimental values of $\tilde{p}$ the internal energy is determined with equation (5.43).

The results for $\tilde{F}$ and $\tilde{U}$ are presented in figure 5.9. One can see in the internal energy that the temperature dependence appears to be well captured and in general agrees with the virial expansion at high temperature, while there is greater uncertainty due to the differentiation process the overall contribution from the Contact remains relatively small at these interaction strengths. With these results it is straight forward to determine the entropy per particle S/Nk_B using equation (5.41) to be

$$\tilde{S} = \frac{S}{Nk_B} = (\tilde{U} - \tilde{F})\frac{T_F}{T}. \tag{5.44}$$

The result for both the entropy per particle and chemical potential are shown in figure 5.10. Interestingly, we note that the entropy curves for each interaction strength lie almost on top of eachother. Finally, we can plot the dependence of $\tilde{p}$ on interactions

$\ln(k_F a_{2D})$ and temperature T/T_F in figure 5.11. The construction of the surface would

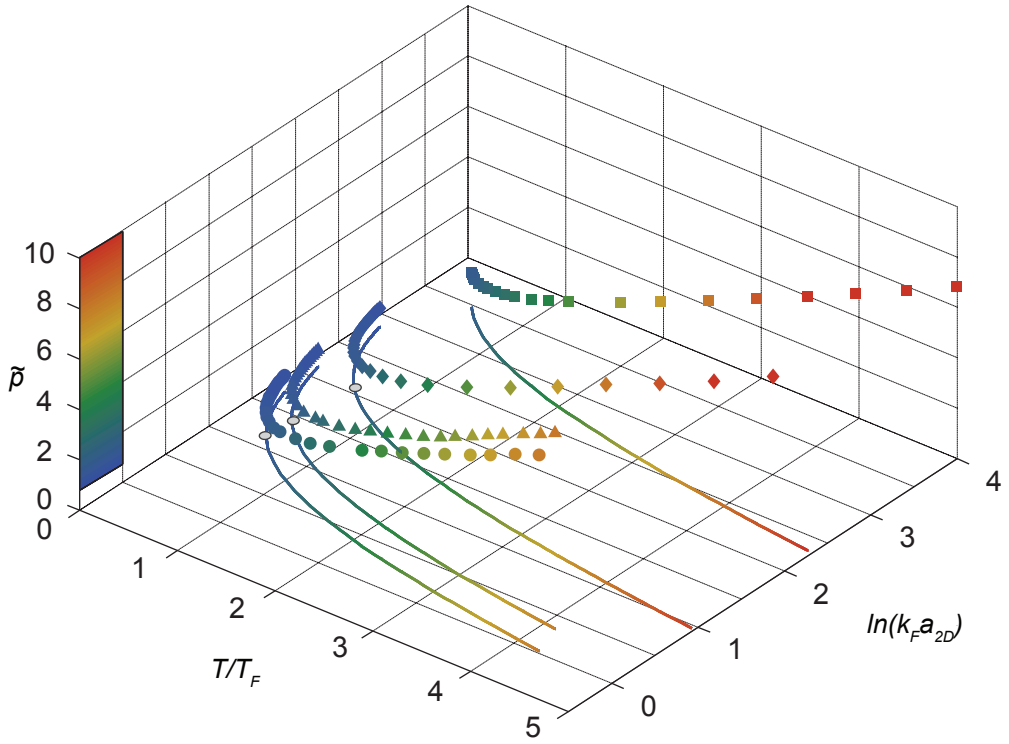

Figure 5.11: Reduced pressure as a function of both interactions and temperature for the four fixed values of βE_B. Contours in the x-y plane are equivalent to figure 5.7

constitute full knowledge of all thermodynamic properties of the two-dimensional Fermi gas. The contours plotted in the plane $\tilde{p} = 0$ are the same as those given in figure 5.7 with the addition of the three grey circles which identify the approximate locations of the peaks found in the density equation of state.

5.4 Validation of thermodynamics

As the temperature and chemical potential are computed through the solutions of the integral equations (5.31) and (5.32) a method of validating the resulting thermodynamics is of significant importance. This is achieved by making use of the fact that the atomic cloud is in thermal equilibrium and should have a constant temperature across the cloud. Secondly the LDA, states $\mu(\mathbf{r}) = \mu_0 - V(\mathbf{r})$ so one should obtain the same central chemical potential μ_0 if the integral in equation 5.32 is stopped at any location in the cloud. We can first determine the validity of our measurement of the temperature. Having determined the reduced temperature as a function of the

dimensionless pressure $\tilde{p}$ we want to check the absolute temperature as a function of position. This requires knowledge of the local Fermi temperature $T_F = E_F/k_B$, which ultimately equates to having knowledge of the function $\tilde{p}(n)$, where n is the local density. The result of this validation is shown in figure 5.12. In each of these the main cause of fluctuation is in the determination of T_F, in part due to discretisation in the binning process used to determine $\tilde{p}$. We can now check the validity of the $\beta\mu$ inte-

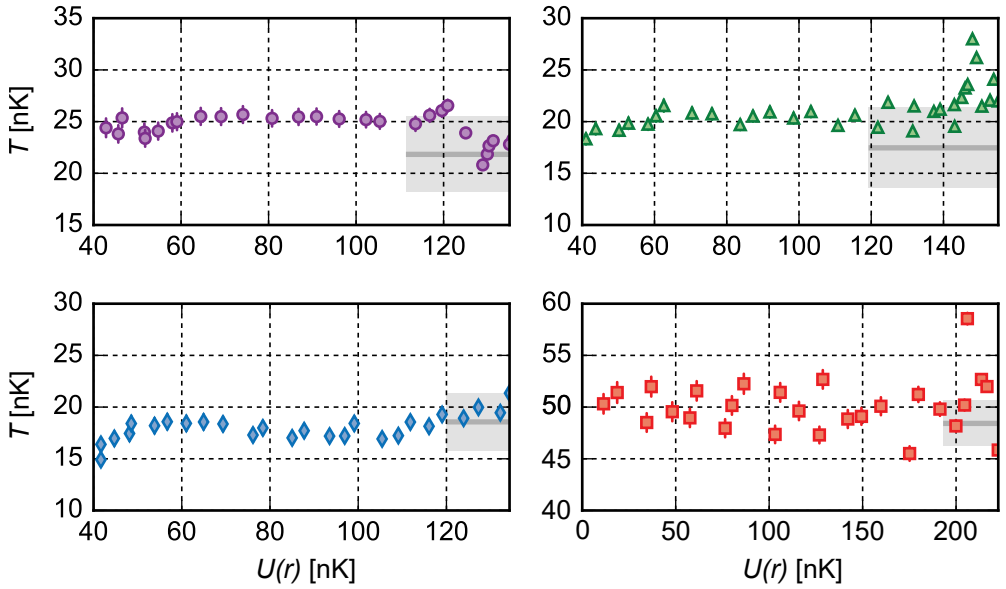

Figure 5.12: Plots of the spatial dependence of the bulk temperature T for each interaction strength. The horizontal grey solid line is the fitted temperature from the virial expansion. Which was determined in the high temperature wings of the atomic cloud. Light grey filled area represents the 95% confidence interval for the fitted temperature.

gral. Having determined and validated $\beta = \frac{1}{k_B T}$ previously, we now have knowledge of μ. Experimentally, all that is needed for this is the determination of the confining potential $V(\mathbf{r})$. This, however, is straightforward to calculate as the trapping potential is provided via magnetic confinement which provides a very pure harmonic trapping potential that we have characterised in Section 3.3.3.2.

In this case the chemical potential $\mu(\mathbf{r})$ is known as a function of $\tilde{p}$. By performing the integral in equation (5.32) and cutting off the integral at different values of $\tilde{p}$ we obtain μ at any position in the cloud. To determine the central chemical potential μ_0 we make use of the LDA in which $\mu_0 = \mu + V(\mathbf{r})$. The extracted central chemical potential as a function of trapping potential can be seen in figure 5.13. Here we find that the value we obtain for the chemical potential is essentially constant with some

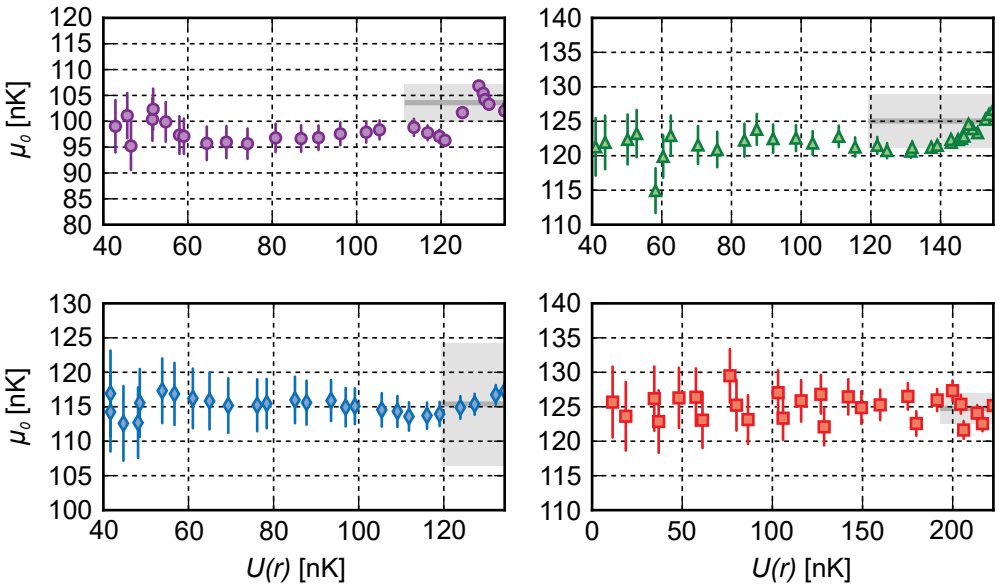

Figure 5.13: Plots of the spatial dependence of the central chemical potential μ_0 for each interaction strength. The horizontal grey solid line is the fitted chemical potential μ_0 from the virial expansion. Which was determined in the high temperature wings of the atomic cloud. Light grey filled area represents the 95% confidence interval for the fitted temperature.

fluctuation, again resulting from discretisation of the binned positions.

As described in Section 5.3.1, virial expansion fits to the high temperature wings of the measured densities are made. From these fits initial values for T and μ_0 are obtained. In our determination of the accuracy of our thermodynamic integrals we assert that the values obtained should reflect the results of the fits. If all three of these criteria are satisfied we are confident that the resulting thermodynamic variables we determined are also accurate. The final self-consistency check which is applied is the

Magnetic Field [G]	βE_B (Virial)	βE_B (Full Analysis)
972	0.005(1)	0.005(1)
920	0.06(1)	0.06(1)
880	0.29(5)	0.26(2)
865	0.49(5)	0.47(3)

Table 5.2: Final values of βE_B found at each magnetic field. The second column gives the final value found by fitting to the density with the third-order virial. The third column is the value found after completing the thermodynamic analysis using the dimensionless variables $\tilde{\kappa}$ and $\tilde{p}$.

same as the one applied to the virial fitting, namely, that the value of βE_B determined by the analysis must agree with the value used to generate the known equation of state. We find this method of thermometry to be particularly robust against errors in the initial conditions supplied ($\tilde{T}_i$ and $(\beta\mu)_i$), with small variations in these parameters not heavily affecting the final results. This insensitivity may arise from two factors: the first is found in the fact that these particular parameters do not change significantly within small regions around a particular value of βE_B. Secondly, as these are integrated quantities the overall contribution from the virial expansion is only over a small range of the integrated data. Provided the initial conditions are not very far away from the correct value.

From the above checks, we find that both T and μ_0 are relatively constant which is expected for a gas in thermal equilibrium. We also observe the measured values of T, μ_0 and βE_B all fall within the error of the virial fit to the high temperature region of the cloud. These results confirm the validity of the analysis.

5.5 Conclusion

In this experiment the method previously used to determine the thermodynamics of three-dimensional Fermi gases and two-dimensional Bose gases has successfully been applied to the case of the two-dimensional Fermi gas. In doing so it has been shown that in two dimensions the thermodynamic behaviour is qualitatively different to that of a Fermi gas in three dimensions, clearly evident in the non-monotonic density equation of state. The presence of a two-body bound state for an arbitrarily weak attractive interaction results in the alteration of the scattering properties in two dimensions. This leads to the interactions having the most significant effect away from the centre of the trapped gas in regions where the Fermi energy approaches the two-body binding energy.

In addition to the equation of state, a number of other thermodynamic properties of a two-dimensional Fermi gas were determined, including the chemical potential, Helmholtz free energy, entropy, pressure, compressibility and internal energy. Each of these showed good agreement with the high temperature virial expansion and pro-

vides benchmarks for strong coupling theories which aim to explore the low temperature thermodynamics beyond the virial expansion.

For the interaction strengths used we were, at best, approximately a factor of two away from the predicted value of T_C [Lev15]. Future measurements of the equation of state below the critical temperature will hopefully be able to resolve the superfluid phase transition and may provide a measurement of T_C as a function of interaction strength for a two-dimensional Fermi gas.

Chapter 6

Conclusion and outlook

The physics of interacting fermions in reduced dimensions is an important field of study and the results contained in this thesis begin to scratch the surface of possibilities in furthering our understanding of this topic. In chapter 3 the theoretical background and technical implementation of the new TEM_{01} mode optical trap were detailed. Here, the results of the beam characterisation and trap frequency measurements were presented. These results indicated the new optical trap could produce a two-dimensional degenerate Fermi gas with significantly larger critical atom number N_{2D} than previous traps at Swinburne, as the new trap achieves an aspect ratio $\Lambda \approx 200$ compared to $\Lambda \approx 60$ for the previous trap [Dyk10].

In chapter 4 the results of the first experiment with the new TEM_{01} mode trap were presented. The aim of this experiment was to better understand the role interactions play in setting the dimensionality of a trapped Fermi gas. To achieve this the transverse width $\left\langle z^2 \right\rangle^{1/2}$ of a tightly confined Fermi gas with total atom numbers of $0.6N_{2D}^{Ideal}$ and $0.3N_{2D}^{Ideal}$ were measured after 600 µs time of flight. This measurement gives an indication of the transverse energy and showed that the total energy in the transverse direction increases for even moderate attractive interactions, indicating the presence of transverse excitations even for the case of $N \ll N_{2D}^{Ideal}$. The fact that the dimensionality is strongly dependent on both the strength of interactions and the density of the gas is important for future studies of two-dimensional Fermi gases, as our results show that measurements performed away from the BCS side of the Feshbach resonance will need to account for transverse excitations.

In order to determine the parameter space in which a kinematically two-dimensional Fermi gas can be produced, a measurement of the transverse width after expansion was made for a range of magnetic fields through the BCS-BEC crossover. At a given magnetic field the total atom number N was varied in a controlled fashion. Measurement of the transverse width from small to large N provides a signature of the transition to the two-dimensional regime through the observation of an elbow in the measured width, which occurs as the transverse width becomes constant independent of N. Here, the constant transverse width indicates that only the transverse ground-state is occupied, satisfying the two-dimensional criteria given in chapter 2. The atom number at the location of this elbow then provides the value of N_{2D} for a given interaction strength. It was found that as the Feshbach resonance was approached from the BCS side a decrease in the observed N_{2D} begins at values $\frac{l_z}{a_{3D}} \gtrsim -1.5$, where l_z is the characteristic length of the harmonic oscillator in the transverse direction and a_{3D} is the three-dimensional s-wave scattering length. At the Feshbach resonance and beyond no strictly two-dimensional behaviour can be seen for the atom numbers accessible in the experiment. Using these measurements a crossover diagram was constructed; this diagram can be used to inform future experiments as to what atom numbers and level of interactions would allow the study of a kinematically two-dimensional Fermi gas.

In chapter 5 the first measurement of the full thermodynamics of a two-dimensional Fermi gas was presented. Implementing the methods used on both the three-dimensional Fermi gas [Ku12] and two-dimensional Bose gas [Des14] the measurement of the thermodynamics was extended to the case of the two-dimensional Fermi gas. These experiments are limited to the BCS regime with atom numbers low enough to remain within the kinematically two-dimensional region as found in chapter 4. To access the thermodynamics the *in situ* density was measured at four magnetic fields (972 G, 920 G, 880 G and 865 G). Through these measured density distributions the local thermodynamic properties of the system were extracted as well as the density and pressure equations of state, which display unique non-monotonic behaviour due to the presence of a two-body bound state for arbitrarily weak attractive interactions in two dimensions. This non-monotonic behaviour shows that the greatest effect of interactions in two dimensions does not occur where the density is largest. Due to technical limitations it was

not possible to cool the gas below the two-dimensional superfluid transition temperature.

Future efforts to further reduce the temperature is a near term goal as the measurement of the thermodynamics of a two-dimensional Fermi superfluid is of great interest and the method used in chapter 5 may help determine the transition temperature T_C and for benchmarking new theoretical models. Comparing the thermodynamic behaviour across the superfluid transition to the three-dimensional case may provide insight into the nature of the phase transition in quasi-two-dimensional condensed matter systems.

Beyond this, the significant experience using Bragg spectroscopy in our lab provides a wide range of experiments which have previously been performed on three-dimensional gases such as studies of the Tan relations and universal short range phenomena. The nature of collective oscillations in two dimensions remain an open question, with previous experiments by Vogt *et al.* [Vog12] deviating from theoretical predictions. Measurement of these oscillations are readily accessible in our current setup and is an avenue which is being explored.

Continuing the theme of extending established three-dimensional techniques to two dimensions is the examination of the physics of p-wave pairing in a two-dimensional Fermi gas. Accessible via the p-wave Feshbach resonance in ^{6}Li, a number of theoretical studies [Chu94; Bot05; Isk06; Lev08; Ino12; Yu15] and experiments [Zha04; Gün05; Sch05; Ina08; Luc16] have explored these resonances in three-dimensions. This pairing behaviour may be important in relating the results of cold-atom experiments to those of condensed matter, as higher order pairing is often found in exotic superfluids and superconductors [Tsu00; Tai10; Zha11]. Accessing p-wave pairing in two dimensions under the controlled environment of ultracold atoms is an exciting possibility as the system may be more stable [Lev08].

Appendices

Appendix A

Software enhancements

A.1 Imaging control

The major software enhancement made to the system is the development of a new integrated imaging controller built in LabView. This controller when combined with additional hardware control programs can significantly increase the level of automation in the experiment. A simplified flowchart of how this controller works is given in figure 3.13. This appendix will outline some additional technical details regarding the design and use of the program. The following sections are written in the style of a user guide for future researchers using this experiment.

A.1.1 Quickstart guide

For those interested in simply running the imaging control software this section is all you will need to read.

- Before running the main VI, double check the camera settings and set up the logging information for the experiment in the input boxes at the top of the front panel.
- At the beginning of the experiment a new folder based on the current date and given experiment name with the naming format 'yymmdd_experiment_name'. To avoid filling the hard drive with unnecessary images the save image option should be turned off until needed.

- The main VI can now be started.
- If any external interfaces or external acquisition trigger is desired these can be turned on and off with the change taking place prior to the next acquisition trigger.
- Reading of oscilloscope signals is available in the oscilloscope tab. From this tab read in can be turned on and off and the type of measurement to read in can be set for each channel.

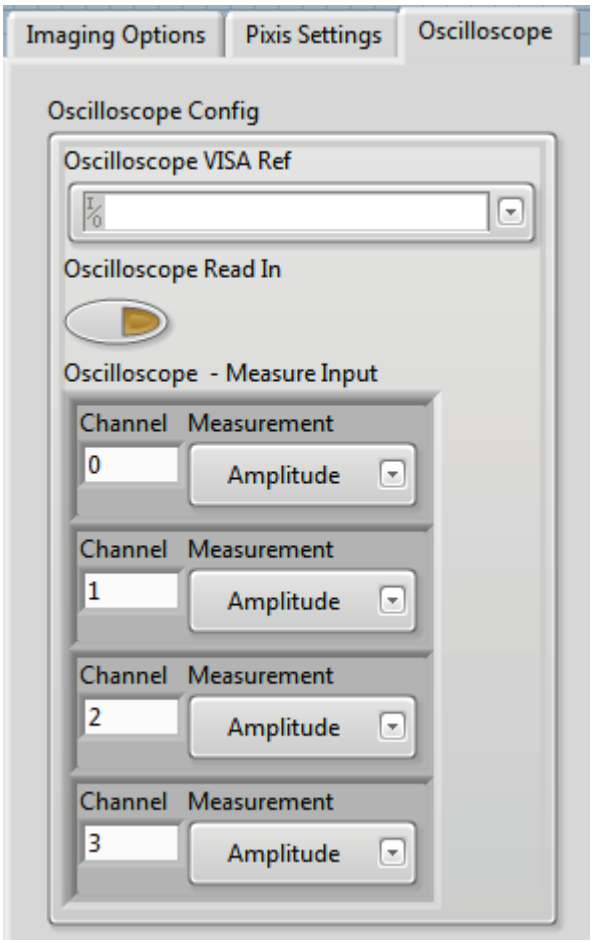

Figure A.1: Oscilloscope setup tab. For each of the four available channels a range of signal properties can be read.

- If the active value is not automatically updated it needs to be updated prior to the acquisition trigger being received for the change to propagate. Failure to do this could compromise the accuracy of the log file.
- Take data.

A.1.2 Camera trigger

Prior to imaging, the camera requires a trigger to begin the acquisition process. This trigger can be provided manually through the imaging controller front panel, or via an external source. For large experiments which require minimal alteration between runs, using the external trigger is of significant usefulness. The trigger source comes from the main experiment computer which has four PCI-6673 National Instruments I/O boards, each with eight analog and eight digital channels. In order to connect the separate experiment control and imaging computers we use the serial port of the imaging computer to read in the TTL signal which originates from one of the digital outputs of the national instruments card. A simple way to do this is by using one of the control bits present in the serial connector. In our experiment we currently make use of the data carrier detect (DCD) control bit corresponding to pin 1 shown in figure A.2. If the option for the external trigger is selected at the beginning of each experimental

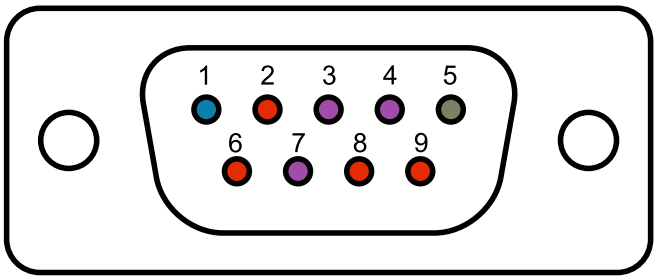

Figure A.2: Pin-out for a standard serial port with DE9 connector. Pins marked in purple are output lines; pin 5 marked in grey is signal ground; all remaining pins are accessible input lines which correspond to control bits which may be read by LabView. Pin 1 marked in blue is the current input line used for the experiment.

run the program will poll the serial port continuously waiting for the trigger as shown in figure A.3. The particular pin which is being polled is selected by changing the DCD state in the VISA instrument properties in the loop shown in figure A.3. As there are a total of five input control bits available to the serial port it is possible to independently trigger the same number of LabView applications if necessary.

External triggering can be activated from the front panel in the experiment setup tab.

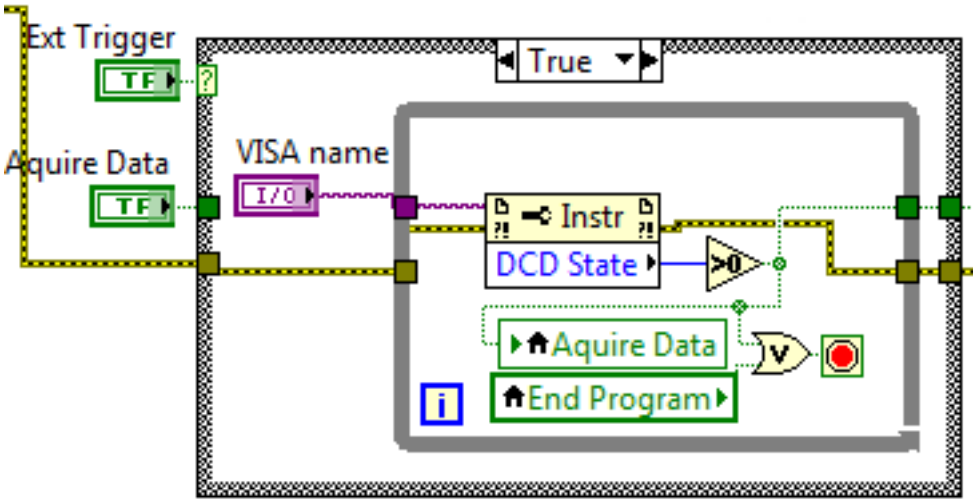

Figure A.3: Polling loop for external acquisition trigger. At every iteration of the loop the selected control bit state is checked. If this bit is set high (> 0) the loop will end and the camera acquisition begun.

A.1.3 Camera settings

All accessible features of the Pixis camera are available in the camera setup tab shown in figure A.4. As these parameters are set once only at the VI start-up phase before the main loop begins, if any of these settings require changing the main VI needs to be stopped and restarted.

Standard settings such as exposure time and ADC readout speed are accessible, along with triggering parameters, CCD cleaning options and region of interest (ROI) selection. For current experiments we make use of the kinetics mode which allows multiple images to be taken within short succession. This can be turned on and off from this setting window. Settings regarding total number of images and accumulations are given in relation to a single acquisition trigger. Currently the experiment consists of a single acquisition trigger which results in a single accumulation of an image consisting of four frames.

In some cases it may be desirable to have the camera free running for diagnostic purposes. To enable this the external trigger option needs to be disabled and free running can be turned on and off via the toggle in the camera settings tab.

As the setting of these functions is achieved through the SITK interface, I refer

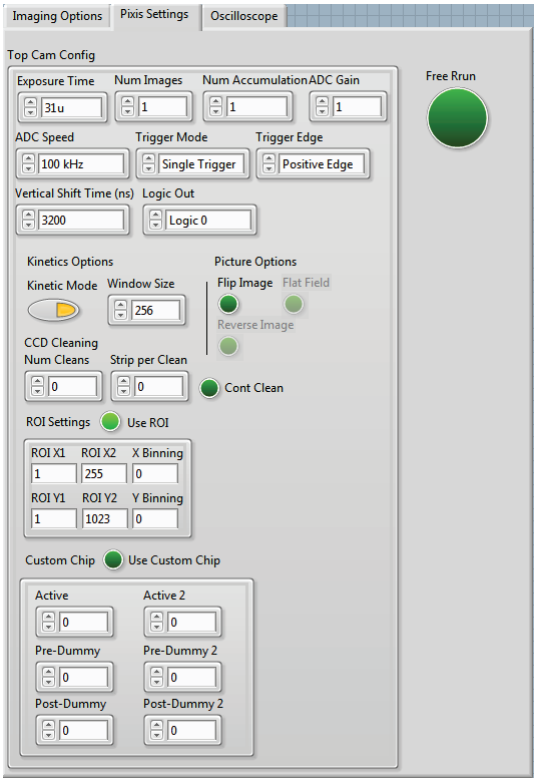

Figure A.4: Settings panel for the Pixis CCD camera.

interested readers to the SITK documentation for details.

A.1.4 Experiment validation

The ability to post-select data allows the overall quality of the results to be improved as the post-selected shot-to-shot variation can be minimised and results which could potentially skew the overall result can be avoided. As all the relevant information which is extracted in our experiments is contained in the resulting absorption image inclusion of this validation in the imaging program is natural. Typically, the experiment is optimised against the total atom number, where a maximised atom number reflects an optimisation in the loading efficiency and imaging frequency. As the density can alter fundamental properties of the gas it is experimentally desirable to keep this parameter constant. While this is difficult due to numerous sources of technical instabilities it is possible to enforce this requirement through post-selection in which we discard any image outside the acceptable level of fluctuations. In figure A.5 the implementation of this feature is shown. In essence any measurable quantity which

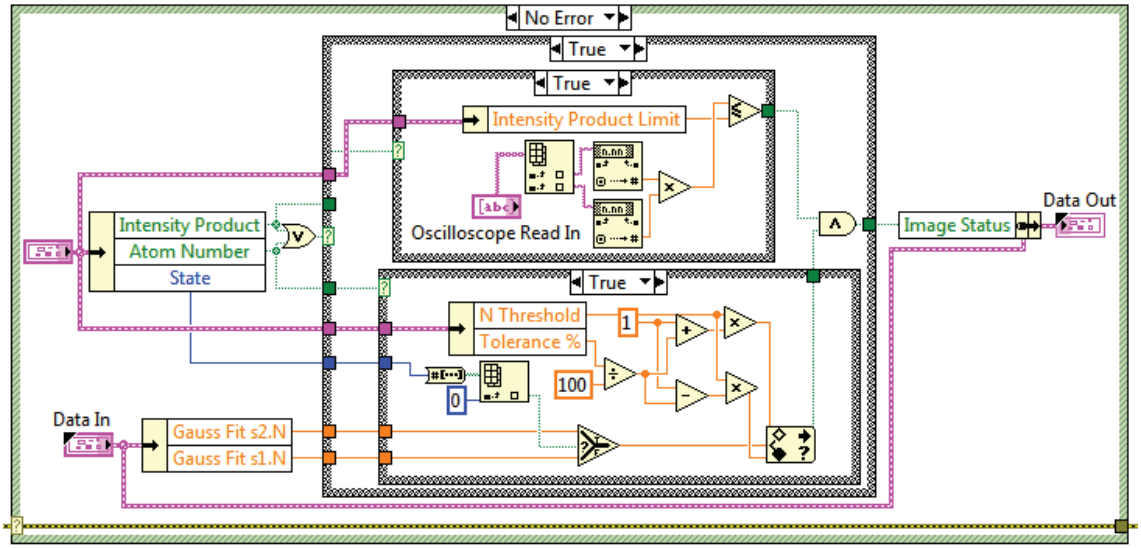

Figure A.5: Image validation VI for the new imaging program. The upper conditional checks if a signal read in from the oscilloscope is below a specified threshold. The lower conditional checks if the total atom number is within a certain range set by the user.

can be obtained from the absorption image can be included in the validation. Some possible quantities could include aspect ratio, temperature, centre of mass, etc.

It is also possible to include external signals as validation criteria. For example, an optical probe of the system which should be constant between cycles can be monitored on a photo-diode. Such a signal can be delivered to an oscilloscope which can be subsequently read in by the imaging program and used as a validation criterion. Additional validation criteria can be be added to *image_validation.vi* and an accessible switch and parameters added to the front panel.

A.1.5 Interfacing with external programs

A significant advantage of the new imaging software is the ability to link independent applications to enhance the level of automation in the experiment. By making use of the LabView message/queue system which allows message passing across running VIs, new programs can be made to work as plug-ins for the imaging controller. To give a general example of how such a system can be used, we can examine a LabView VI which directly controls a direct digital synthesiser (DDS). Within this program there is implemented some control logic which scans through a range of frequencies to be out-

put by introducing a communication channel between this program and the imaging controller. The imaging controller which performs logging duties can receive up-to-date information regarding the type of waveform and any pertinent parameters which should be logged and the DDS controller can receive notifications of the status either pass or fail from the imaging controller allowing it to then either proceed to the next frequency if the last experimental run was a success or simply repeat the experiment with the same parameters until the validation is passed.

Detail regarding the LabView message/queue system is readily available in the LabView documentation, but briefly, a key component for inter-VI communication is maintaining a consistent queue naming scheme. It is good practice to allow the linkage between programs to be user-selectable and all selected queues initialised at start-up. Directly following start-up the imaging controller checks for any messages on the selected queues in order to set the initial parameters for logging. Finally, after the experimental run has concluded and an image taken, the result of the validation process can be sent to the desired queue. The connected program can then extract this information and proceed based on the control logic implemented. A small example of such an action is given in Figure A.6. This can then continue for the duration of the experiment.

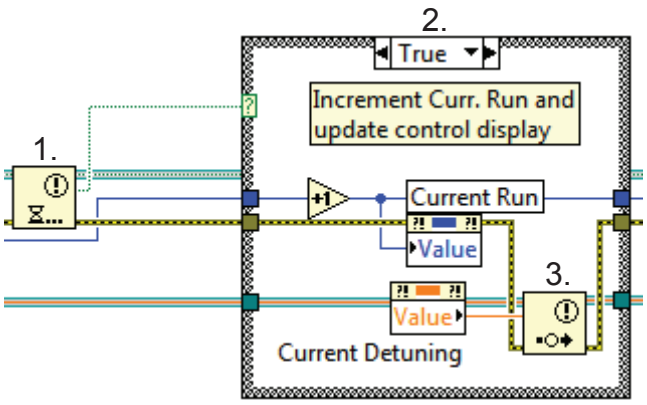

Figure A.6: Basic framework for responding to inter-VI messages. At position (1) the VI will wait until a notification has arrived. At (2) some internal function will be evaluated. Finally at (3) the new active value which has been set is sent to the imaging program to maintain accurate logging.

Appendix B

Copyright statements

I warrant that I have obtained, where neccessary, permission from the copyright owners to use any third party copyright material reproduced in the thesis (such as artwork, images, unpublished documents), or to use any of my own published work (such as journal articles) in which the copyright is held by another party (such as publisher, co-author).

Figure 4.3 Reprinted figures with permission from T. Bourdel *et al.* "Eperimental study of the BEC-BCS crossover region in lithium 6", *Physical Review Letters* **93** (5), 050401 (2004).

Figure 5.6 Reprinted with permission from AAAS. From M. J. H Ku, A. T. Sommer, L. W. Cheuk and M. W. Zwierlein, "Revealing the superfluid lambda transition in the universal thermodynamics of a unitary Fermi gas," *Science* **335**, 563 (2012).

Bibliography

[Adh86] S. K. Adhikari. "Quantum scattering in two dimensions." *American Journal of Physics* **54** (4), 362–367 (1986) (cit. on p. 23).

[Aik14] K. Aikawa, A. Frisch, M. Mark, S. Baier, R. Grimm, and F. Ferlaino. "Reaching Fermi degeneracy via universal dipolar scattering." *Physical Review Letters* **112** (1), 010404 (2014) (cit. on p. 11).

[And15] E. Anderson and J. Drut. "Pressure, compressibility, and contact of the two-dimensional attractive Fermi gas." *Physical Review Letters* **115** (11), 115301 (2015) (cit. on pp. 6, 84, 97, 98).

[And95] M. H. Anderson, J. R. Ensher, M. R. Matthews, C. E. Wieman, and E. A. Cornell. "Observation of Bose-Einstein condensation in a dilute atomic vapor." *Science* **269** (5221), 198–201 (1995) (cit. on p. 1).

[Ash70] A. Ashkin. "Acceleration and trapping of particles by radiation pressure." *Physical Review Letters* **24** (4), 156–159 (1970) (cit. on p. 37).

[Ash97] A. Ashkin. "Optical trapping and manipulation of neutral particles using lasers." *Proceedings of the National Academy of Sciences of the United States of America* **94** (10), 4853–60 (1997) (cit. on p. 38).

[Bag91] V. Bagnato and D. Kleppner. "Bose-Einstein condensation in low-dimensional traps." *Physical Review A* **44** (11), 7439–7441 (1991) (cit. on p. 4).

[Bar57] J. Bardeen, L. N. Cooper, and J. R. Schrieffer. "Theory of superconductivity." *Physical Review* **108** (5), 1175–1204 (1957) (cit. on pp. 2, 28, 31).

[Bau09] D. M. Bauer, M. Lettner, C. Vo, G. Rempe, and S. Dürr. “Control of a magnetic Feshbach resonance with laser light.” *Nature Physics* **5** (5), 339–342 (2009) (cit. on p. 27).

[Bau14] M. Bauer, M. M. Parish, and T. Enss. “Universal equation of state and pseudogap in the two-dimensional Fermi gas.” *Physical Review Letters* **112** (13), 135302 (2014) (cit. on pp. 6, 84, 97, 98).

[Bay98] M. Bayindir and B. Tanatar. “Bose-Einstein condensation in a two-dimensional, trapped, interacting gas.” *Physical Review A* **58** (4), 3134–3137 (1998) (cit. on p. 4).

[Bed86] J. G. Bednorz and K. A. Müller. “Possible high T_c superconductivity in the Ba-La-Cu-O system.” *Zeitschrift für Physik B Condensed Matter* **64** (2), 189 (1986) (cit. on p. 3).

[Bei94] M. Beijersbergen, R. Coerwinkel, M. Kristensen, and J. Woerdman. “Helical-wavefront laser beams produced with a spiral phaseplate.” *Optics Communications* **112** (5-6), 321–327 (1994) (cit. on p. 47).

[Ber11] G. Bertaina and S. Giorgini. “BCS-BEC crossover in a two-dimensional Fermi gas.” *Physical Review Letters* **106** (11), 110403 (2011) (cit. on pp. 4, 84).

[Ber71] V. L. Berezinskii. “Destruction of long-range order in one-dimensional and two-dimensional systems having a continuous symmetry group I. classical systems.” *Soviet Journal of Experimental and Theoretical Physics* **32** (3), 2–9 (1971) (cit. on p. 3).

[Ber72] V. L. Berezinskii. “Destruction of long-range order in one-dimensional and two-dimensional systems possessing a continuous symmetry group. II. quantum systems.” *Soviet Journal of Experimental and Theoretical Physics* **34**, 610 (1972) (cit. on p. 33).

[Bet49] H. A. Bethe. “Theory of the effective range in nuclear scattering.” *Physical Review* **76** (1), 38–50 (1949) (cit. on p. 22).

[Blo05] I. Bloch. “Ultracold quantum gases in optical lattices.” *Nature Physics* **1** (1), 23–30 (2005) (cit. on p. 1).

[Blo08] I. Bloch, J. Dalibard, and W. Zwerger. “Many-body physics with ultracold gases.” *Reviews of Modern Physics* **80** (3), 885–964 (2008) (cit. on pp. 29, 90).

[Boe16] I. Boettcher, L. Bayha, D. Kedar, P. A. Murthy, M. Neidig, M. G. Ries, A. N. Wenz, G. Zürn, S. Jochim, and T. Enss. “Equation of state of ultracold fermions in the 2D BEC-BCS crossover region.” *Physical Review Letters* **116**, 045303 (4 2016) (cit. on p. 84).

[Bon98] M. Boninsegni and M. W. Cole. “Superfluidity of monolayer helium films.” *Journal of Low Temperature Physics* **113** (3), 393–398 (1998) (cit. on p. 83).

[Bot05] S. S. Botelho and C. A. R. Sá de Melo. “Quantum phase transition in the BCS-to-BEC evolution of p-wave Fermi gases.” *Journal of Low Temperature Physics* **140** (5-6), 409–428 (2005) (cit. on p. 113).

[Bot06] S. S. Botelho and C. A. R. Sá De Melo. “Vortex-antivortex lattice in ultracold fermionic gases.” *Physical Review Letters* **96** (4), 040404 (2006) (cit. on p. 3).

[Bou03] T. Bourdel, J. Cubizolles, L. Khaykovich, K. M. F. Magalhães, S. J. J. M. F. Kokkelmans, G. V. Shlyapnikov, and C. Salomon. “Measurement of the interaction energy near a Feshbach resonance in a ^{6}Li Fermi gas.” *Physical Review Letters* **91** (2), 020402 (2003) (cit. on p. 66).

[Bou04] T. Bourdel, L. Khaykovich, J. Cubizolles, J. Zhang, F. Chevy, M. Teichmann, L. Tarruell, S. J. J. M. F. Kokkelmans, and C. Salomon. “Experimental study of the BEC-BCS crossover region in lithium 6.” *Physical Review Letters* **93** (5), 050401 (2004) (cit. on pp. 66, 73).

[Bra13] W. H. Bragg and W. L. Bragg. “The reflection of X-rays by crystals.” *Proceedings of the Royal Society A: Mathematical, Physical and Engineering Sciences* **88** (605), 428–438 (1913) (cit. on p. 20).

[Bra95] C. C. Bradley, C. A. Sackett, J. J. Tollett, and R. G. Hulet. "Evidence of Bose-Einstein condensation in an atomic gas with attractive interactions." *Physical Review Letters* **75** (9), 1687–1690 (1995) (cit. on p. 1).

[Bul09] I. Buluta and F. Nori. "Quantum simulators." *Science* **326** (5949), 108–111 (2009) (cit. on p. 1).

[Bur01] S. Burger, F. S. Cataliotti, C. Fort, P. Maddaloni, F. Minardi, and M. Inguscio. "Quasi 2D Bose-Einstein condensation in an optical lattice." *Europhysics Letters* **57** (1), 7 (2001) (cit. on p. 44).

[Bur14] A. Burchianti, G. Valtolina, J. A. Seman, E. Pace, M. De Pas, M. Inguscio, M. Zaccanti, and G. Roati. "Efficient all-optical production of large ^{6}Li quantum gases using D_1 gray-molasses cooling." *Physical Review A* **90** (4), 043408 (2014) (cit. on p. 41).

[Chi10] C. Chin, R. Grimm, P. Julienne, and E. Tiesinga. "Feshbach resonances in ultracold gases." *Reviews of Modern Physics* **82** (2), 1225–1286 (2010) (cit. on p. 25).

[Cho12] L. Chomaz, L. Corman, T. Yefsah, R. Desbuquois, and J. Dalibard. "Absorption imaging of a quasi-two-dimensional gas: A multiple scattering analysis." *New Journal of Physics* **14** (5), 055001 (2012) (cit. on p. 62).

[Chu94] A. V. Chubukov and A. Sokol. "Theory of p-wave pairing in a two-dimensional Fermi gas." *Physical Review B* **49** (1), 678–681 (1994) (cit. on p. 113).

[Coo56] L. N. Cooper. "Bound electron pairs in a degenerate Fermi gas." *Physical Review* **104** (4), 1189–1190 (1956) (cit. on pp. 2, 28, 31).

[Cub03] J. Cubizolles, T. Bourdel, S. J. J. M. F. Kokkelmans, G. V. Shlyapnikov, and C. Salomon. "Production of long-lived ultracold Li_2 molecules from a Fermi gas." *Physical Review Letters* **91** (24), 240401 (2003) (cit. on p. 2).

[Dag94] E. Dagotto. "Correlated electrons in high-temperature superconductors." *Reviews of Modern Physics* **66** (3), 763–840 (1994) (cit. on p. 83).

[Dal89] J. Dalibard and C. Cohen-Tannoudji. “Laser cooling below the Doppler limit by polarization gradients: simple theoretical models.” *Journal of the Optical Society of America B* **6** (11), 2023–2045 (1989) (cit. on p. 37).

[Dal99a] F. Dalfovo, S. Giorgini, L. P. Pitaevskii, and S. Stringari. “Theory of Bose-Einstein condensation in trapped gases.” *Reviews of Modern Physics* **71** (3), 463–512 (1999) (cit. on p. 84).

[Dal99b] J. Dalibard. “Collisional dynamics of ultra-cold atomic gases.” *Bose-Einstein Condensation in Atomic Gases: Proceedings of the international school of physics (Enrico Fermi)*. Ed. by M. Inguscio, S. Stringari, and C. Wieman. IOS Press, 1999, 321–349 (cit. on p. 30).

[Dav95] K. B. Davis, M. O. Mewes, M. R. Andrews, N. J. Van Druten, D. S. Durfee, D. M. Kurn, and W. Ketterle. “Bose-Einstein condensation in a gas of sodium atoms.” *Physical Review Letters* **75** (22), 3969–3973 (1995) (cit. on p. 1).

[DeM99] B. DeMarco and D. S. Jin. “Onset of Fermi degeneracy in a trapped atomic gas.” *Science* **285** (5434), 1703–1706 (1999) (cit. on pp. 1, 11).

[Des13] R. Desbuquois. “Thermal and superfluid properties of the two-dimensional Bose gas.” PhD thesis. École Normale Supérieure, 2013 (cit. on p. 92).

[Des14] R. Desbuquois, T. Yefsah, L. Chomaz, C. Weitenberg, L. Corman, S. Nascimbène, and J. Dalibard. “Determination of scale-invariant equations of state without fitting parameters: Application to the two-dimensional Bose gas across the Berezinskii-Kosterlitz-Thouless transition.” *Physical Review Letters* **113** (2), 020404 (2014) (cit. on pp. 84, 87, 112).

[Dub14] R. Dubessy, C. De Rossi, T. Badr, L. Longchambon, and H. Perrin. “Imaging the collective excitations of an ultracold gas using statistical correlations.” *New Journal of Physics* **16** (12), 122001 (2014) (cit. on p. 92).

[Dyk10] P. Dyke. “Quasi two-dimensional Li Fermi gas.” PhD thesis. Swinburne University, 2010 (cit. on pp. 7, 35, 41, 111).

[Dyk11] P. Dyke, E. D. Kuhnle, S. Whitlock, H. Hu, M. Mark, S. Hoinka, M. Lingham, P. Hannaford, and C. J. Vale. "Crossover from 2D to 3D in a weakly interacting Fermi gas." *Physical Review Letters* **106** (10), 105304 (2011) (cit. on pp. 6, 19, 76).

[Dyk16a] P. Dyke, K. Fenech, T. Peppler, M. G. Lingham, S. Hoinka, W. Zhang, B. Mulkerin, H. Hu, X.-J. Liu, and C. J. Vale. "Criteria for two-dimensional kinematics in an interacting Fermi gas." *Physical Review A* **93** (1), 011603 (2016) (cit. on pp. i, 66, 71).

[Dyk16b] P. Dyke, K. Fenech, T. Peppler, M. G. Lingham, S. Hoinka, W. Zhang, B. Mulkerin, H. Hu, X.-J. Liu, and C. J. Vale. "Supplemental material: Criteria for two-dimensional kinematics in an interacting Fermi gas." *Physical Review A* **93** (1), 011603 (2016) (cit. on pp. 71, 72).

[Fan61] U. Fano. "Effects of configuration interaction on intensities and phase shifts." *Physical Review* **124** (6), 1866–1878 (1961) (cit. on p. 25).

[Fel11] M. Feld, B. Fröhlich, E. Vogt, M. Koschorreck, and M. Köhl. "Observation of a pairing pseudogap in a two-dimensional Fermi gas." *Nature* **480** (7375), 75–78 (2011) (cit. on p. 7).

[Fen16a] K. Fenech, P. Dyke, T. Peppler, M. G. Lingham, S. Hoinka, H. Hu, and C. J. Vale. "Supplmental material: Thermodynamics of an attractive 2D Fermi gas." *Physical Review Letters* **116** (4), 045302 (2016) (cit. on p. 88).

[Fen16b] K. Fenech, P. Dyke, T. Peppler, M. G. Lingham, S. Hoinka, H. Hu, and C. J. Vale. "Thermodynamics of an attractive 2D Fermi gas." *Physical Review Letters* **116** (4), 045302 (2016) (cit. on pp. ii, 84).

[Fes58] H. Feshbach. "Unified theory of nuclear reactions." *Annals of Physics* **5** (4), 357–390 (1958) (cit. on pp. 2, 11, 25).

[Fey82] R. P. Feynman. "Simulating physics with computers." *International Journal of Theoretical Physics* **21** (6-7), 467–488 (1982) (cit. on p. 1).

[Fis13] A. M. Fischer and M. M. Parish. "BCS-BEC crossover in a quasi-two-dimensional Fermi gas." *Physical Review A* **88** (2), 023612 (2013) (cit. on p. 4).

[Fis14] A. M. Fischer and M. M. Parish. “Quasi-two-dimensional Fermi gases at finite temperature.” *Physical Review B* **90** (21), 214503 (2014) (cit. on p. 32).

[Foo04] C. Foot. *Atomic Physics*. Oxford University Press, 2004 (cit. on p. 37).

[Frö12] B. Fröhlich, M. Feld, E. Vogt, M. Koschorreck, M. Köhl, C. Berthod, and T. Giamarchi. “Two-dimensional Fermi liquid with attractive interactions.” *Physical Review Letters* **109** (13), 130403 (2012) (cit. on pp. 4, 103).

[Fuc09] J. Fuchs. “Molecular Bose-Einstein Condensates and p-wave Feshbach Molecules of $^6Li_2$.” PhD thesis. Swinburne University of Technology, 2009 (cit. on p. 35).

[Gau13] A. L. Gaunt, T. F. Schmidutz, I. Gotlibovych, R. P. Smith, and Z. Hadzibabic. “Bose-Einstein condensation of atoms in a uniform potential.” *Physical Review Letters* **110** (20) (2013) (cit. on p. 15).

[Gio08] S. Giorgini, L. P. Pitaevskii, and S. Stringari. “Theory of ultracold atomic Fermi gases.” *Reviews of Modern Physics* **80** (4), 1215–1274 (2008) (cit. on p. 21).

[Gre02] M. Greiner, O. Mandel, T. Esslinger, T. W. Hänsch, and I. Bloch. “Quantum phase transition from a superfluid to a Mott insulator in a gas of ultracold atoms.” *Nature* **415** (6867), 39–44 (2002) (cit. on p. 1).

[Gre03] M. Greiner, C. A. Regal, and D. S. Jin. “Emergence of a molecular Bose-Einstein condensate from a Fermi gas.” *Nature* **426** (6966), 537–540 (2003) (cit. on pp. 2, 31).

[Gri00] R. Grimm, M. Weidemüller, and Y. B. Ovchinnikov. “Optical dipole traps for neutral atoms.” *Advances in Atomic, Molecular and Optical Physics* **42**, 95–170 (2000) (cit. on pp. 37, 38, 43).

[Gri13] A. T. Grier, I. Ferrier-Barbut, B. S. Rem, M. Delehaye, L. Khaykovich, F. Chevy, and C. Salomon. “Λ-enhanced sub-Doppler cooling of lithium atoms in D_1 gray molasses.” *Physical Review A* **87** (6), 063411 (2013) (cit. on p. 41).

[Gün05] K. Günter, T. Stöferle, H. Moritz, M. Köhl, and T. Esslinger. "p-wave interactions in low-dimensional Fermionic gases." *Physical Review Letters* **95** (23), 230401 (2005) (cit. on p. 113).

[Had06] Z. Hadzibabic, P. Krüger, M. Cheneau, B. Battelier, and J. Dalibard. "Berezinskii-Kosterlitz-Thouless crossover in a trapped atomic gas." *Nature* **441** (7097), 1118–1121 (2006) (cit. on pp. 7, 33).

[Had13] Z. Hadzibabic and J. Dalibard. "BKT physics with two-dimensional atomic gases." *40 Years of Berezinskii-Kosterlitz-Thouless Theory*. World Scientific, 2013. Chap. 9, 297–323 (cit. on p. 33).

[Hal10] E. Haller, M. J. Mark, R. Hart, J. G. Danzl, V. Melezhik, and P. Schmelcher. "Confinement-induced resonances in low-dimensional quantum systems." *Physical Review Letters* **104** (15), 1–5 (2010) (cit. on pp. 70, 81).

[Has10] M. Z. Hasan and C. L. Kane. "*Colloquium*: Topological insulators." *Reviews of Modern Physics* **82** (4), 3045–3067 (2010) (cit. on p. 83).

[Hau99] R. Haussmann. *Self-consistent quantum field theory and bosonization for strongly correlated electron systems*. Vol. 56. Springer, 1999, viii+175 (cit. on p. 6).

[Hec92] N. R. Heckenberg, R. McDuff, C. P. Smith, and A. G. White. "Generation of optical phase singularities by computer-generated holograms." *Optics Letters* **17** (3), 221–223 (1992) (cit. on p. 47).

[Ho04] T. L. Ho. "Universal thermodynamics of degenerate quantum gases in the unitarity limit." *Physical Review Letters* **92** (9), 090402 (2004) (cit. on pp. ii, 89, 102).

[Hof12] J. Hofmann. "Quantum anomaly, universal relations, and breathing mode of a two-dimensional Fermi gas." *Physical Review Letters* **108** (18), 185303 (2012) (cit. on p. 103).

[Hoh67] P. C. Hohenberg. "Existence of long-range order in one and two dimensions." *Physical Review* **158** (2), 383–386 (1967) (cit. on pp. 3, 4, 33).

[Hoi13] S. Hoinka, M. Lingham, K. Fenech, H. Hu, C. J. Vale, J. E. Drut, and S. Gandolfi. “Precise determination of the structure factor and contact in a unitary Fermi gas.” *Physical Review Letters* **110** (5), 055305 (2013) (cit. on pp. 4, 103).

[Hoi14] S. Hoinka. “Precision Bragg spectroscopy of the density and spin response of a strongly interacting Fermi gas.” PhD thesis. Swinburne University of Technology, 2014 (cit. on pp. 35, 36, 60).

[Hor10] M. Horikoshi, S. Nakajima, M. Ueda, and T. Mukaiyama. “Measurement of universal thermodynamic functions for a unitary Fermi gas.” *Science* **327** (5964), 442–445 (2010) (cit. on p. 84).

[Hou98] M. Houbiers, H. T. C. Stoof, W. I. McAlexander, and R. G. Hulet. “Elastic and inelastic collisions of ^{6}Li atoms in magnetic and optical traps.” *Physical Review A* **57** (3), 1497 (1998) (cit. on p. 25).

[Hun14] C.-L. Hung and C. Chin. “In situ imaging of atomic quantum gases.” *Quantum Gas Experiments*. Imperial College Press, 2014. Chap. 6, 101–120 (cit. on p. 84).

[Idz06] Z. Idziaszek and T. Calarco. “Analytical solutions for the dynamics of two trapped interacting ultracold atoms.” *Physical Review A* **74** (2), 022712 (2006) (cit. on p. 71).

[Ina08] Y. Inada, M. Horikoshi, S. Nakajima, M. Kuwata-Gonokami, M. Ueda, and T. Mukaiyama. “Collisional properties of p-wave Feshbach molecules.” *Physical Review Letters* **101** (10), 100401 (2008) (cit. on p. 113).

[Ino12] D. Inotani, R. Watanabe, M. Sigrist, and Y. Ohashi. “Pseudogap phenomena of an ultracold Fermi gas with a p-wave Feshbach resonance.” *Journal of Physics: Conference Series* **400** (1), 012021 (2012) (cit. on p. 113).

[Ino98] S. Inouye, M. R. Andrews, J. Stenger, H.-J. Miesner, D. M. Stamper-Kurn, and W. Ketterle. “Observation of Feshbach resonances in a Bose-Einstein condensate.” *Nature* **392** (6672), 151–154 (1998) (cit. on p. 25).

[Isk06] M. Iskin and C. A. R. Sá de Melo. “Evolution from BCS to BEC superfluidity in p-wave Fermi gases.” *Physical Review Letters* **96** (4), 040402 (2006) (cit. on p. 113).

[Joc03a] S. Jochim, M. Bartenstein, A. Altmeyer, G. Hendl, C. Chin, J. H. Denschlag, and R. Grimm. “Pure gas of optically trapped molecules created from fermionic atoms.” *Physical Review Letters* **91** (24), 240402 (2003) (cit. on p. 2).

[Joc03b] S. Jochim, M. Bartenstein, A. Altmeyer, G. Hendl, S. Riedl, C. Chin, J. H. Denschlag, and R. Grimm. “Bose-Einstein condensation of molecules.” *Science* **302** (5653), 2101–2103 (2003) (cit. on pp. 2, 31).

[Jol02] I. T. Jolliffe. *Principal Component Analysis, Second Edition*. Second. Springer, 2002 (cit. on p. 91).

[Kam11a] H. Kamerlingh Onnes. “Further experiments with liquid helium. C. On the change of electric resistance of pure metals at very low temperatures, etc. IV. The resistance of pure mercury at helium temperatures.” *Comm. Phys. Lab. Univ. Leiden* **120b** (1911) (cit. on p. 3).

[Kam11b] H. Kamerlingh Onnes. “Further experiments with liquid helium. D. On the change of electric resistance of pure metals at very low temperatures, etc. V. The disappearance of the resistance of mercury.” *Comm. Phys. Lab. Univ. Leiden* **122b** (1911) (cit. on p. 3).

[Kam11c] H. Kamerlingh Onnes. “Further experiments with liquid helium. G. On the electrical resistance of pure metals, etc. VI. On the sudden change in the rate at which the resistance of mercury disappears.” *Comm. Phys. Lab. Univ. Leiden* **124c** (1911) (cit. on p. 3).

[Kap38] P. Kapitza. “Viscosity of liquid helium below the λ-point.” *Nature* **141** (3558), 74–74 (1938) (cit. on p. 1).

[Kes06] J. P. Kestner and L. M. Duan. “Conditions of low dimensionality for strongly interacting atoms under a transverse trap.” *Physical Review A* **74** (5), 053606 (2006) (cit. on pp. 5, 65).

[Ket07] W. Ketterle and M. W. Zwierlein. “Making, probing and understanding ultracold Fermi gases.” *Ultracold Fermi gases: Proceedings of the international school of physics (Enrico Fermi)*. Ed. by M. Inguscio, S. Stringari, and C. Salomon. Vol. 164. IOS Press, 2007, 95–287 (cit. on pp. 16, 21, 28, 30).

[Kin06] J. Kinast. “Thermodynamics and superfluidity of a strongly interacting Fermi gas.” PhD thesis. Duke University, 2006 (cit. on p. 59).

[Köh06] T. Köhler, K. Góral, and P. S. Julienne. “Production of cold molecules via magnetically tunable Feshbach resonances.” *Reviews of Modern Physics* **78** (4), 1311–1361 (2006) (cit. on pp. 25, 28).

[Kos72] J. M. Kosterlitz and D. J. Thouless. “Long range order and metastability in two dimensional solids and superfluids. (Application of dislocation theory).” *Journal of Physics C: Solid State Physics* **5** (11), L124–L126 (1972) (cit. on p. 3).

[Kos73] J. M. Kosterlitz and D. J. Thouless. “Ordering, metastability and phase transitions in two-dimensional systems.” *Journal of Physics C: Solid State Physics* **6** (7), 1181–1203 (1973) (cit. on p. 33).

[Ku12] M. J. H. Ku, A. T. Sommer, L. W. Cheuk, and M. W. Zwierlein. “Revealing the superfluid lambda transition in the universal thermodynamics of a unitary Fermi gas.” *Science* **335** (6068), 563–567 (2012) (cit. on pp. 84, 87, 112).

[Kuh11] E. D. Kuhnle, S. Hoinka, H. Hu, P. Dyke, P. Hannaford, and C. J. Vale. “Studies of the universal contact in a strongly interacting Fermi gas using Bragg spectroscopy.” *New Journal of Physics* **13** (5), 055010 (2011) (cit. on pp. 4, 103).

[Lan70] L. D. Landau and E. M. Lifshitz. *Statistical Physics*. Vol. 5. Pergamon Press, 1970 (cit. on p. 12).

[Leg75] A. J. Leggett. “A theoretical description of the new phases of liquid ^{3}He.” *Reviews of Modern Physics* **47** (2), 331–414 (1975) (cit. on p. 28).

[Let79] V. S. Letokhov and V. G. Minogin. “Cooling, trapping, and storage of atoms by resonant laser fields.” *Journal of the Optical Society of America* **69** (3), 413–419 (1979) (cit. on p. 37).

[Lev08] J. Levinsen, N. R. Cooper, and V. Gurarie. “Stability of the fermionic gases close to a p-wave Feshbach resonance.” *Physical Review A* **78** (6), 1–14 (2008) (cit. on p. 113).

[Lev15] J. Levinsen and M. M. Parish. “Strongly interacting two-dimensional Fermi gases.” *Annual Review of Cold Atoms and Molecules*. World Scientific, 2015. Chap. 1, 1–75 (cit. on pp. 24, 32, 34, 90, 109).

[Ley11] X. Leyronas. “Virial expansion with Feynman diagrams.” *Physical Review A* **84** (5), 053633 (2011) (cit. on p. 88).

[Lin14] M. G. Lingham, K. Fenech, S. Hoinka, and C. J. Vale. “Local observation of pair condensation in a Fermi gas at unitarity.” *Physical Review Letters* **112** (10), 100404 (2014) (cit. on p. 103).

[Liu10] X.-J. Liu, H. Hu, and P. D. Drummond. “Exact few-body results for strongly correlated quantum gases in two dimensions.” *Physical Review B* **82** (5), 054524 (2010) (cit. on pp. 5, 88).

[Liu13] X. J. Liu. “Virial expansion for a strongly correlated Fermi system and its application to ultracold atomic Fermi gases.” *Physics Reports* **524** (2), 37–83 (2013) (cit. on p. 88).

[Lon38] F. London. “The λ-phenomenon of liquid helium and the Bose-Einstein degeneracy.” *Nature* **141** (3571), 643–644 (1938) (cit. on p. 1).

[Lu12] M. Lu, N. Q. Burdick, and B. L. Lev. “Quantum degenerate dipolar Fermi gas.” *Physical Review Letters* **108** (21), 215301 (2012) (cit. on p. 11).

[Luc16] C. Luciuk, S. Trotzky, S. Smale, Z. Yu, S. Zhang, and J. H. Thywissen. “Evidence for universal relations describing a gas with *p*-wave interactions.” *Nature Physics* (2016) (cit. on p. 113).

[Mak14] V. Makhalov, K. Martiyanov, and A. Turlapov. “Ground-state pressure of quasi-2D Fermi and Bose gases.” *Physical Review Letters* **112** (4), 045301 (2014) (cit. on pp. 8, 84).

[Mar10] K. Martiyanov, V. Makhalov, and A. Turlapov. “Observation of a two-dimensional Fermi gas of atoms.” *Physical Review Letters* **105** (3), 030404 (2010) (cit. on pp. 6, 7, 44).

[Men02] C. Menotti, P. Pedri, and S. Stringari. “Expansion of an interacting Fermi gas.” *Physical Review Letters* **89** (25), 250402 (2002) (cit. on p. 66).

[Mep10] R. Meppelink, R. A. Rozendaal, S. B. Koller, J. M. Vogels, and P. Van Der Straten. “Thermodynamics of Bose-Einstein-condensed clouds using phase-contrast imaging.” *Physical Review A* **81** (5), 053632 (2010) (cit. on p. 58).

[Mer66] N. D. Mermin and H. Wagner. “Absence of ferromagnetism or antiferromagnetism in one- or two-dimensional isotropic Heisenberg models.” *Physical Review Letters* **17** (22), 1133–1136 (1966) (cit. on pp. 3, 4, 33).

[Met02] H. J. Metcalf and P. van der Straten. *Laser Cooling and Trapping*. Springer, 2002 (cit. on p. 37).

[Mey05] T. Meyrath, F. Schreck, J. Hanssen, C. Chuu, and M. Raizen. “A high frequency optical trap for atoms using Hermite-Gaussian beams.” *Optics Express* **13** (8), 2843–51 (2005) (cit. on pp. 6, 44, 46, 47).

[Miy83] K. Miyake. “Fermi liquid theory of dilute submonolayer ^{3}He on thin ^{4}He II film: Dimer bound state and Cooper pairs.” *Progress of Theoretical Physics* **69** (6), 1794–1797 (1983) (cit. on p. 32).

[Mod03] G. Modugno, F. Ferlaino, R. Heidemann, G. Roati, and M. Inguscio. “Production of a Fermi gas of atoms in an optical lattice.” *Physical Review A* **68** (1), 011601 (2003) (cit. on p. 6).

[Moe95] A. J. Moerdijk, B. J. Verhaar, and A. Axelsson. “Resonances in ultracold collisions of ^{6}Li, ^{7}Li, and ^{23}Na.” *Physical Review A* **51** (6), 4852–4861 (1995) (cit. on pp. 25, 27).

[Mor14] K. H. Morgener. “Microscopy of 2D Fermi gases exploring excitations and thermodynamics.” PhD thesis. Universitat Hamburg, 2014 (cit. on p. 44).

[Mul15] B. C. Mulkerin, K. Fenech, P. Dyke, C. J. Vale, X.-J. Liu, and H. Hu. “Comparison of strong-coupling theories for a two-dimensional Fermi gas.” *Physical Review A* **92** (6), 063636 (2015) (cit. on p. 98).

[Mur14] P. A. Murthy, D. Kedar, T. Lompe, M. Neidig, M. G. Ries, A. N. Wenz, G. Zürn, and S. Jochim. “Matter-wave Fourier optics with a strongly interacting two-dimensional Fermi gas.” *Physical Review A* **90** (4), 043611 (2014) (cit. on p. 8).

[Mur15] P. A. Murthy, I. Boettcher, L. Bayha, M. Holzmann, D. Kedar, M. Neidig, M. G. Ries, A. N. Wenz, G. Zürn, and S. Jochim. “Observation of the Berezinskii-Kosterlitz-Thouless phase transition in an ultracold Fermi gas.” *Physical Review Letters* **115** (1), 010401 (2015) (cit. on pp. 8, 33).

[Nas10] S. Nascimbène, N. Navon, K. J. Jiang, F. Chevy, and C. Salomon. “Exploring the thermodynamics of a universal Fermi gas.” *Nature* **463** (7284), 1057–1060 (2010) (cit. on p. 84).

[Nav10] N. Navon, S. Nascimbene, F. Chevy, and C. Salomon. “The equation of state of a low-temperature Fermi gas with tunable interactions.” *Science* **328** (5979), 729–732 (2010) (cit. on p. 84).

[Nga13] V. Ngampruetikorn, J. Levinsen, and M. M. Parish. “Pair correlations in the two-dimensional Fermi gas.” *Physical Review Letters* **111** (26), 265301 (2013) (cit. on pp. 5, 88).

[Ols98] M. Olshanii. “Atomic scattering in presence of an external confinement and a gas of impenetrable bosons.” *Physical Review Letters* **81** (5), 5 (1998) (cit. on p. 70).

[Pat11] R. K. Pathria and P. D. Beale. *Statistical Mechanics*. Third. Elsevier, 2011 (cit. on p. 13).

[Pei35] R. Peierls. “Quelques propriétés typiques des corps solides.” *Annales de l’institut Henri Poincaré* **5** (3), 177–222 (1935) (cit. on p. 3).

[Pen11] S.-G. Peng, H. Hu, X.-J. Liu, and P. D. Drummond. “Confinement induced resonances in anharmonic waveguides.” *Physical Review A* **84**, 043619 (2011) (cit. on pp. 70, 81).

[Pet01] D. S. Petrov and G. V. Shlyapnikov. “Interatomic collisions in a tightly confined Bose gas.” *Physical Review A* **64** (1), 012700 (2001) (cit. on pp. 5, 24, 25, 29, 66, 90).

[Pet02] C. J. Pethick and H. Smith. *Bose-Einstein condensation in dilute gases*. Cambridge University Press, 2002 (cit. on pp. 13, 15).

[Pet03] D. S. Petrov, M. A. Baranov, and G. V. Shlyapnikov. “Superfluid transition in quasi-two-dimensional Fermi gases.” *Physical Review A* **67** (3), 031601 (2003) (cit. on pp. 5, 32, 33).

[Pet04] D. S. Petrov, C. Salomon, and G. V. Shlyapnikov. “Weakly bound molecules of fermionic atoms.” *Physical Review Letters* **93** (9), 090404 (2004) (cit. on p. 28).

[Phi82] W. D. Phillips and H. Metcalf. “Laser deceleration of an atomic beam.” *Physical Review Letters* **48** (9), 596–599 (1982) (cit. on p. 39).

[Phi85] W. D. Phillips, J. V. Prodan, and H. J. Metcalf. “Laser cooling and electromagnetic trapping of neutral atoms.” *Journal of the Optical Society of America B* **2** (11), 1751–1767 (1985) (cit. on p. 37).

[Raa87] E. L. Raab, M. Prentiss, A. Cable, S. Chu, and D. E. Pritchard. “Trapping of Neutral Sodium Atoms with Radiation Pressure.” *Physical Review Letters* **59** (23), 2631–2634 (1987) (cit. on p. 40).

[Ran90] M. Randeria, J.-M. Duan, and L.-Y. Shieh. “Superconductivty in a two-dimensional Fermi gas: Evolution from Cooper pairing to Bose condensation.” *Physical Review B* **41** (327) (1990) (cit. on p. 4).

[Rat10] S. P. Rath, T. Yefsah, K. J. Günter, M. Cheneau, R. Desbuquois, M. Holzmann, W. Krauth, and J. Dalibard. “Equilibrium state of a trapped two-dimensional Bose gas.” *Physical Review A* **82** (1), 013609 (2010) (cit. on p. 84).

[Reg03] C. A. Regal, C. Ticknor, J. L. Bohn, and D. S. Jin. “Creation of ultracold molecules from a Fermi gas of atoms.” *Nature* **424** (6944), 47–50 (2003) (cit. on p. 2).

[Rei07] G. Reinaudi, T. Lahaye, Z. Wang, and D. Guéry-Odelin. “Strong saturation absorption imaging of dense clouds of ultracold atoms.” *Optics Letters* **32** (21), 3143–3145 (2007) (cit. on pp. 59, 62).

[Rie15a] M. G. Ries, A. N. Wenz, G. Zürn, L. Bayha, I. Boettcher, D. Kedar, P. A. Murthy, M. Neidig, T. Lompe, and S. Jochim. “Observation of pair condensation in the quasi-2D BEC-BCS crossover.” *Physical Review Letters* **114** (23), 230401 (2015) (cit. on pp. 6, 8, 33).

[Rie15b] M. G. Ries. “A two-dimensional Fermi gas in the BEC-BCS crossover.” PhD thesis. Ruperto-Carola-University of Heidelberg, 2015 (cit. on p. 44).

[Rio12] D. Rio Fernandes, F. Sievers, N. Kretzschmar, S. Wu, C. Salomon, and F. Chevy. “Sub-Doppler laser cooling of fermionic ^{40}K atoms in three-dimensional gray optical molasses.” *Europhysics Letters* **100** (6), 63001 (2012) (cit. on p. 41).

[Rut11] E. Rutherford. “The scattering of α and β particles by matter and the structure of the atom.” *Philosophical Magazine* **21** (6), 669–688 (1911) (cit. on p. 20).

[Sá 93] C. A. R. Sá De Melo, M. Randeria, and J. R. Engelbrecht. “Crossover from BCS to Bose superconductivity: Transition temperature and time-dependent Ginzburg-Landau theory.” *Physical Review Letters* **71** (19), 3202–3205 (1993) (cit. on p. 2).

[Sag12] Y. Sagi, T. E. Drake, R. Paudel, and D. S. Jin. “Measurement of the homogeneous contact of a unitary Fermi gas.” *Physical Review Letters* **109** (22), 220402 (2012) (cit. on p. 4).

[Sal00] L. Salasnich. “Ideal quantum gases in D-dimensional space and power-law potentials.” *Journal of Mathematical Physics* **41** (12), 8016 (2000) (cit. on p. 17).

[Sal07] B. E. A. Saleh and M. C. Teich. *Fundamentals of Photonics*. 2nd. Wiley, 2007 (cit. on p. 45).

[San10] C. Sanner, E. J. Su, A. Keshet, R. Gommers, Y.-i. Shin, W. Huang, and W. Ketterle. "Suppression of density fluctuations in a quantum degenerate Fermi gas." *Physical Review Letters* **105** (4), 040402 (2010) (cit. on p. 33).

[Sch05] C. H. Schunck, M. W. Zwierlein, C. A. Stan, S. M. F. Raupach, W. Ketterle, A. Simoni, E. Tiesinga, C. J. Williams, and P. S. Julienne. "Feshbach resonances in fermionic ^{6}Li." *Physical Review A* **71** (4), 045601 (2005) (cit. on p. 113).

[Sch07] V. Schweikhard, S. Tung, and E. A. Cornell. "Vortex proliferation in the Berezinskii-Kosterlitz-Thouless regime on a two-dimensional lattice of Bose-Einstein condensates." *Physical Review Letters* **99** (3), 030401 (2007) (cit. on p. 33).

[Sch93] A. Schilling, M. Cantoni, J. D. Guo, and H. R. Ott. "Superconductivity above 130 K in the Hg-Pb-Ba-Ca-Cu-O system." *Nature* **363** (64224), 56–58 (1993) (cit. on p. 3).

[Ser98] I. Serre, L. Pruvost, and H. T. Duong. "Fluorescence imaging efficiency of cold atoms in free fall." *Applied Optics* **37** (6), 1016–1021 (1998) (cit. on p. 58).

[Som12] A. T. Sommer, L. W. Cheuk, M. J. H. Ku, W. S. Bakr, and M. W. Zwierlein. "Evolution of fermion pairing from three to two dimensions." *Physical Review Letters* **108** (4), 045302 (2012) (cit. on p. 7).

[Ste99] J. Stenger, S. Inouye, M. R. Andrews, H.-J. Miesner, D. M. Stamper-Kurn, and W. Ketterle. "Strongly enhanced inelastic collisions in a Bose-Einstein condensate near Feshbach resonances." *Physical Review Letters* **82** (12), 2422 (1999) (cit. on p. 28).

[Str03] K. E. Strecker, G. B. Partridge, and R. G. Hulet. "Conversion of an atomic Fermi gas to a long-lived molecular Bose gas." *Physical Review Letters* **91** (8), 080406 (2003) (cit. on p. 2).

[Tai10] L. Taillefer. “Scattering and pairing in cuprate superconductors.” *Annual Review of Condensed Matter Physics* **1** (1), 51–70 (2010) (cit. on p. 113).

[Tan08] S. Tan. “Generalized virial theorem and pressure relation for a strongly correlated Fermi gas.” *Annals of Physics* **323** (12), 2987–2990 (2008) (cit. on p. 103).

[Tay72] J. R. Taylor. *Scattering theory: the quantum theory on nonrelativistic collisions*. New York: Wiley, 1972 (cit. on p. 21).

[Tem09] J. Tempere, S. N. Klimin, and J. T. Devreese. “Effect of population imbalance on the Berezinskii-Kosterlitz-Thouless phase transition in a superfluid Fermi gas.” *Physical Review A* **79** (5), 053637 (2009) (cit. on p. 4).

[The04] M. Theis, G. Thalhammer, K. Winkler, M. Hellwig, G. Ruff, R. Grimm, and J. H. Denschlag. “Tuning the scattering length with an optically induced Feshbach resonance.” *Physical Review Letters* **93** (12), 123001 (2004) (cit. on p. 27).

[Tho05] J. E. Thomas, J. Kinast, and A. Turlapov. “Virial theorem and universality in a unitary Fermi gas.” *Physical Review Letters* **95** (12), 120402 (2005) (cit. on p. 5).

[Tie93] E. Tiesinga, B. J. Verhaar, and H. T. C. Stoof. “Threshold and resonance phenomena in ultracold ground-state collisions.” *Physical Review A* **47** (5), 4114–4122 (1993) (cit. on p. 25).

[Tör14] P. Törmä. “Spectroscopies - Theory.” *Quantum Gas Experiments*. Imperial College Press, 2014. Chap. 10, 199–250 (cit. on p. 4).

[Tra94] S. V. Traven. “Superfluidity of a two-dimensional dilute attractive Fermi gas.” *Physical Review Letters* **73** (25), 3451 (1994) (cit. on p. 5).

[Tru01] A. G. Truscott, K. E. Strecker, W. I. McAlexander, G. B. Partridge, and R. G. Hulet. “Observation of Fermi pressure in a gas of trapped atoms.” *Science* **291** (5512), 2570–2572 (2001) (cit. on pp. 1, 11).

[Tsu00] C. C. Tsuei and J. R. Kirtley. “Pairing symmetry in cuprate superconductors.” *Reviews of Modern Physics* **72** (4), 969–1016 (2000) (cit. on p. 113).

[Tur04] L. D. Turner, K. P. Weber, D. Paganin, and R. E. Scholten. “Off-resonant defocus-contrast imaging of cold atoms.” *Optics Letters* **29** (3), 232–234 (2004) (cit. on p. 58).

[Val11] M. Valiente, N. T. Zinner, and K. Mølmer. “Universal relations for the two-dimensional spin-1/2 Fermi gas with contact interactions.” *Physical Review A* **84** (6), 063525 (2011) (cit. on p. 103).

[Van12] K. Van Houcke, F. Werner, E. Kozik, N. Prokof’ev, B. Svistunov, M. J. H. Ku, A. T. Sommer, L. W. Cheuk, A. Schirotzek, and M. W. Zwierlein. “Feynman diagrams versus Fermi-gas Feynman emulator.” *Nature Physics* **8** (5), 366–370 (2012) (cit. on p. 1).

[Vee08] G. Veeravalli, E. Kuhnle, P. Dyke, and C. J. Vale. “Bragg spectroscopy of a strongly interacting Fermi gas.” *Physical Review Letters* **101** (25), 250403 (2008) (cit. on p. 4).

[Vee09] G. Veeravalli. “Bragg spectroscopy of a strongly interacting Fermi gas.” PhD thesis. Swinburne University of Technology, 2009 (cit. on p. 35).

[Vog12] E. Vogt, M. Feld, B. Fröhlich, D. Pertot, M. Koschorreck, and M. Köhl. “Scale invariance and viscosity of a two-dimensional Fermi gas.” *Physical Review Letters* **108** (7), 070404 (2012) (cit. on p. 113).

[Wer12] F. Werner and Y. Castin. “General relations for quantum gases in two and three dimensions. II. Bosons and mixtures.” *Physical Review A* **86** (5), 053633 (2012) (cit. on p. 103).

[Yef11] T. Yefsah, R. Desbuquois, L. Chomaz, K. J. Günter, and J. Dalibard. “Exploring the thermodynamics of a two-dimensional Bose gas.” *Physical Review Letters* **107** (13), 130401 (2011) (cit. on pp. 8, 44, 84).

[Yu15] Z. Yu, J. H. Thywissen, and S. Zhang. “Universal relations for a Fermi gas close to a p-wave interaction resonance.” *Physical Review Letters* **115** (13), 135304 (2015) (cit. on p. 113).

[Yur10] V. A. Yurovsky and M. Olshanii. “Restricted thermalization for two interacting atoms in a multimode harmonic waveguide.” *Physical Review A* **81** (4), 043641 (2010) (cit. on p. 72).

[Zha04] J. Zhang, E. G. M. van Kempen, T. Bourdel, L. Khaykovich, J. Cubizolles, F. Chevy, M. Teichmann, L. Tarruell, S. J. J. M. F. Kokkelmans, and C. Salomon. “*P*-wave Feshbach resonances of ultracold ^{6}Li.” *Physical Review A* **70** (3), 030702 (2004) (cit. on p. 113).

[Zha08] W. Zhang, G.-D. Lin, and L.-M. Duan. “Berezinskii-Kosterlitz-Thouless transition in a trapped quasi-two-dimensional Fermi gas near a Feshbach resonance.” *Physical Review A* **78** (4), 1–6 (2008) (cit. on p. 3).

[Zha11] Y. H. Zhang and B. Jin. “Quasi-2D non-chiral p-wave superconductors in parallel magnetic field: The multiple phase transitions.” *Physica C: Superconductivity* **471** (19-20), 586–590 (2011) (cit. on p. 113).

[Zür13] G. Zürn, T. Lompe, A. N. Wenz, S. Jochim, P. S. Julienne, and J. M. Hutson. “Precise characterization of ^{6}Li Feshbach resonances using trap-sideband-resolved RF spectroscopy of weakly bound molecules.” *Physical Review Letters* **110** (March), 135301 (2013) (cit. on pp. 27, 28).

[Zwe12] W. Zwerger, ed. *The BCS-BEC crossover and the unitary Fermi gas*. Vol. 836. Lecture Notes in Physics. Berlin, Heidelberg: Springer Berlin Heidelberg, 2012 (cit. on p. 31).

[Zwi03] M. W. Zwierlein, C. A. Stan, C. H. Schunck, S. M. F. Raupach, S. Gupta, Z. Hadzibabic, and W. Ketterle. “Observation of Bose-Einstein condensation of molecules.” *Physical Review Letters* **91** (25), 250401 (2003) (cit. on pp. 2, 31).

[Zwi04] M. W. Zwierlein, C. A. Stan, C. H. Schunck, S. M. F. Raupach, A. J. Kerman, and W. Ketterle. “Condensation of pairs of fermionic atoms near a Feshbach resonance.” *Physical Review Letters* **92** (12), 120403 (2004) (cit. on p. 25).

[Zwi05] M. W. Zwierlein, C. H. Schunck, C. A. Stan, S. M. F. Raupach, and W. Ketterle. “Formation dynamics of a fermion pair condensate.” *Physical Review Letters* **94** (18), 180401 (2005) (cit. on p. 31).

[Zwi06] M. W. Zwierlein, C. H. Schunck, A. Schirotzek, and W. Ketterle. “Direct observation of the superfluid phase transition in ultracold Fermi gases.” *Nature* **442** (7098), 54–58 (2006) (cit. on p. 31).

Publications

K. Fenech, P. Dyke, T. Peppler, M. Lingham, S. Hoinka and C. J. Vale, "Thermodynamics of an attractive 2D Fermi gas", *Physical Review Letters* **116**(4), 045302 (2016).

P. Dyke, K. Fenech, T. Peppler, M. G. Lingham, S. Hoinka, W. Zhang, S.-G. Peng, B. Mulkerin, H. Hu, X.-J. Liu and C. J. Vale, "Criteria for 2D kinematics in an interacting Fermi gas", *Physical Review A* **93**, 011603 (2016).

B. Mulkerin, K. Fenech, P. Dyke, C. J. Vale, X.-J. Liu and H. Hu, "Comparison of strong-coupling theories for a two-dimensional Fermi gas", *Physical Review A* **92**, 063636 (2015).

M. G. Lingham, K. Fenech, S. Hoinka and C. J. Vale, "Local observation of pair condensation in a Fermi gas at unitarity", *Physical Review Letters* **112**, 100404 (2014).

S. Hoinka, M. Lingham, K. Fenech, H. Hu, C. J. Vale, J. E. Drut and S. Gandolfi, "Precise determination of the structure factor and contact in a unitary Fermi gas", *Physical Review Letters* **110**, 055305 (2013).